Novel Over-the-Air Methods and Practical Approaches for Reconfigurable Intelligent Surfaces System Designs and Analyses

by

Emre Arslan

A Dissertation Submitted to the
Graduate School of Sciences and Engineering
in Partial Fulfillment of the Requirements for
the Degree of

Doctor of Philosophy

in

Electrical and Electronics Engineering

KOÇ ÜNİVERSİTESİ

March 5, 2025

Novel Over-the-Air Methods and Practical Approaches for Reconfigurable Intelligent Surfaces System Designs and Analyses

Koç University
Graduate School of Sciences and Engineering

This is to certify that I have examined this copy of a doctoral dissertation by

Emre Arslan

and have found that it is complete and satisfactory in all respects,
and that any and all revisions required by the final
examining committee have been made.

Committee Members:

Prof. Ertuğrul Başar (Advisor)

Prof. Sinem Çöleri

Dr. Öğr. Üyesi Murat Kuşcu

Prof. Ali Emre Pusane

Doç. Erdoğan Aydın

Date:

Dedicated to my lovely wife and daughter

ABSTRACT

Novel Over-the-Air Methods and Practical Approaches for Reconfigurable Intelligent Surfaces System Designs and Analyses
Emre Arslan
Doctor of Philosophy in Electrical and Electronics Engineering
March 5, 2025

The rapid evolution of wireless communication networks towards 6G and beyond requires innovative solutions to enhance spectral efficiency, improve system reliability, and manage the growing complexity of modern communication systems. This thesis explores the integration of reconfigurable intelligent surfaces (RIS) with communication systems to address fundamental challenges in wireless networks, such as challenges in the channel, overall system efficiency, system scalability, practicality and more. By leveraging RIS technology, the wireless propagation environment can be dynamically reconfigured to optimize signal transmission, mitigate interference, and enhance network performance. This thesis presents novel over-the-air (OTA) approaches to RIS-aided communication systems, considering both passive and active RIS architectures as well as their practical implications in real-world deployments.

Chapter 2 investigates an virtual OTA equalization technique enabled by RIS, demonstrating how RIS phase alignment can effectively eliminate inter-symbol interference (ISI) and convert frequency-selective fading channels into frequency-flat channels. Chapter 3 includes a study proposing RIS-aided uplink non-orthogonal multiple access (NOMA) schemes, optimizing resource allocation and improving outage probability performance for two users. Chapter 4 introduces a hybrid RIS architecture for OTA index modulation (IM), integrating passive and active RIS elements to achieve superior spectral efficiency and reduced detection complexity. Chapter 5 focuses on network-independent RIS architectures, proposing a user-controlled RIS system that enhances practicality, signal quality and energy efficiency in a simple and practical manner without relying on centralized network control. Chapter 6 discusses RIS identification techniques in mobile networks, addressing critical challenges related to RIS security, authentication, and interference mitigation, introduc-

ing a new and important concept for RIS deployment to the literature. Chapter 7 presents a power-differentiated dual-code index modulation (RIS-PD-DCIM) scheme that improves spectral efficiency and performance through optimal RIS partitioning strategies.

The contributions of this thesis provide a comprehensive framework for RIS-aided communication systems, addressing key limitations in existing wireless technologies and paving the way for the seamless integration of RIS into 6G networks. The proposed methodologies and system models demonstrate the potential of RIS to revolutionize wireless communications by offering enhanced system designs, improved spectral and energy efficiency, and robust performance in dynamic environments. These findings contribute to the ongoing efforts in the research community to develop practical, scalable, and intelligent wireless networks for the future.

ÖZETÇE

Doktora Tez Başlığı
Emre Arslan
Elektrik ve Elektronik Mühendisliği, Doktora
5 Mart 2025

Kablosuz iletişim ağlarının 6G ve ötesine doğru hızla evrilmesi, spektral verimliliğin artırılması, sistem güvenilirliğinin iyileştirilmesi ve modern iletişim sistemlerinin giderek artan karmaşıklığının yönetilmesi için yenilikçi çözümler gerektirmektedir. Bu tez, kablosuz ağlarda karşılaşılan temel zorlukları ele almak amacıyla yeniden yapılandırılabilir akıllı yüzeylerin (RIS) iletişim sistemleriyle entegrasyonunu incelemektedir. Kanal karakteristikleri, genel sistem verimliliği, sistem ölçeklenebilirliği, pratik uygulanabilirlik gibi kritik konular ele alınarak, RIS teknolojisinin kullanımıyla kablosuz yayılım ortamının dinamik olarak yeniden yapılandırılması, sinyal iletiminin optimize edilmesi, girişimlerin azaltılması ve ağ performansının iyileştirilmesi hedeflenmektedir. Bu tez, RIS destekli iletişim sistemlerine yönelik yenilikçi hava üzerinden (OTA) yaklaşımlar sunmakta olup, hem pasif hem de aktif RIS mimarilerini ve bunların gerçek dünya uygulamalarındaki pratik sonuçlarını ele almaktadır.

2. bölüm, RIS destekli hava üzerinden dengeleme (OTA equalization) metodunu inceleyerek, RIS faz hizalamasının semboller arası girişimi (ISI) nasıl etkili bir şekilde ortadan kaldırabileceğini ve frekans seçici sönümleme kanallarını frekans düzlemine çevirebileceğini göstermektedir. 3. bölüm, RIS destekli yukarı yönlü ortogonal olmayan çoklu erişim (NOMA) şemaları önererek kaynak tahsisinin optimize edilmesini ve iki kullanıcı için kesinti olasılığı performansının iyileştirilmesini ele almaktadır. 4. bölüm, hava üzerinden indis modülasyonu için hibrit RIS mimarilerini tanıtarak, pasif ve aktif RIS elemanlarının entegre edilmesiyle üstün spektral verimlilik ve azaltılmış algılama karmaşıklığı elde edilmesini sağlamaktadır. 5. bölüm, ağdan bağımsız RIS mimarilerine odaklanarak, merkezi ağ kontrolüne bağlı kalmadan sinyal kalitesi ve enerji verimliliğini artıran kullanıcı kontrollü pratik bir RIS sistemi önermektedir. 6. bölüm, mobil ağlarda RIS tanımlama (identification) tekniklerini inceleyerek, RIS güvenliği, kimlik doğrulama ve girişim azaltma

ile ilgili kritik zorlukları ele almakta ve literatüre RIS dağıtımı açısından yeni ve önemli bir kavram kazandırmaktadır. 7. bölüm, güç farklılaştırmalı çift kodlu indis modülasyonu (RIS-PD-DCIM) şeması sunarak, optimal RIS bölme stratejileri ile spektral verimliliği ve sistem performansını iyileştirmeyi amaçlamaktadır.

Bu tezin katkıları, RIS destekli iletişim sistemleri için kapsamlı bir çerçeve sunarak mevcut kablosuz teknolojilerdeki temel sınırlamaları ele almakta ve RIS'in 6G ağlarına sorunsuz entegrasyonu için bir yol haritası çizmektedir. Önerilen yöntemler ve sistem modelleri, RIS'in kablosuz iletişimde devrim yaratma potansiyelini ortaya koyarak, gelişmiş sistem tasarımları, iyileştirilmiş spektral ve enerji verimliliği ile dinamik ortamlarda güçlü performans sunmaktadır. Bu bulgular, araştırma topluluğunun gelecekte pratik, ölçeklenebilir ve akıllı kablosuz ağlar geliştirme çabalarına önemli katkılar sağlamaktadır.

ACKNOWLEDGMENTS

I would like to express my sincere gratitude to my advisor, Dr. Ertugrul Basar, for his continuous support and motivation. It has been a a fruitful and nice journey together.

I would like to thank my father for encouraging and pushing me to never give up and always do my best.

Additionally, I would like to thank my mother for raising me to be who I am today and for her constant love.

I would especially like to thank my fellow partners in science and very dear and close friends Ali Tugberk Dogukan and Fatih Kilinc for their continuous support, motivation and kind friendship. Hardships are overcome easier with brothers by your side.

Last but not least I would like to thank my wife for always believing in me and pushing me to be my best.

Everything I have ever accomplished, every opportunity given to me, every hardship overcome, my mental and physical strength, the amazing people I have met throughout my years, everything is thanks to Allah s.w.t., Elhamdulillah.

CONTENTS

LIST OF TABLES

LIST OF FIGURES

ABBREVIATIONS

AWGN	Additive White Gaussian Noise
BER	Bit Error Rate
BS	Base Station
CB	Codebook
CIM	Code Index Modulation
CSI	Channel State Information
DL	Downlink
EE	Energy Efficiency
FFT	Fast-Fourier Transform
IM	Index Modulation
IoT	Internet-of-Things
ISI	Inter-Symbol Interference
KPI	Key Performance Indicator
LC	Low Complexity
LLR	Log-Likelihood Ratio
LOS	Line-of-Sight
MIMO	Multiple-Input Multiple-Output
ML	Maximum Likelihood
NOMA	Non-orthogonal Multiple Acess
NLOS	Non-Line-of-Sight
NU/FU	Near User/Far User
OFDM	Orthogonal Frequency Division Multiplexing
OTA	Over-the-Air
PEP	Pairwise Error Probability

QAM	Quadrature Amplitude Modulation
QoS	Quality of Service
RIS	Reconfigurable Intelligent Surface
SC	Superposition Coding
SIC	Successive Interference Cancelation
SISO	Single Input Single Output
SNR	Signal-to-Noise Ratio
SSK	Space Shift Keying
UE	User Equipment
5G	Fifth-Generation Wireless
6G	Sixth-Generation Wireless
3GPP	Third Generation Partnership Project

Chapter 1

INTRODUCTION

In this chapter, the importance of reconfigurable intelligent surface (RIS) technology will be emphasized along with a brief introduction to RIS technology for 5G and beyond wireless communications networks. The contributions of this thesis to the literature will also be discussed.

1.1 On Reconfigurable Intelligent Surfaces

The deployment of fifth-generation (5G) wireless networks has introduced significant advancements in communication technology, including enhanced data rates, ultra-reliable low-latency communication (URLLC), and massive machine-type communication (mMTC) [Jiang and Liu, 2016]. However, despite these improvements, several limitations remain, including insufficient spectrum efficiency, limited energy efficiency, and challenges in achieving ubiquitous connectivity in complex environments. As we move towards the development of sixth-generation (6G) networks, it is essential to address these shortcomings and introduce novel solutions that will enable more efficient, intelligent, and sustainable communication systems. The growing demands of emerging applications such as holographic communication, intelligent automation, and immersive virtual environments necessitate a fundamental improvement of wireless communication architectures. The shift from 5G to 6G will require more strict demands and transformative innovations in resource usage, network intelligence, and energy sustainability [Wang et al., 2023a]. Future networks must be capable of supporting ultra-reliable connectivity, instantaneous response times, and seamless integration of diverse technologies, all while maintaining cost-effectiveness and environmental sustainability.

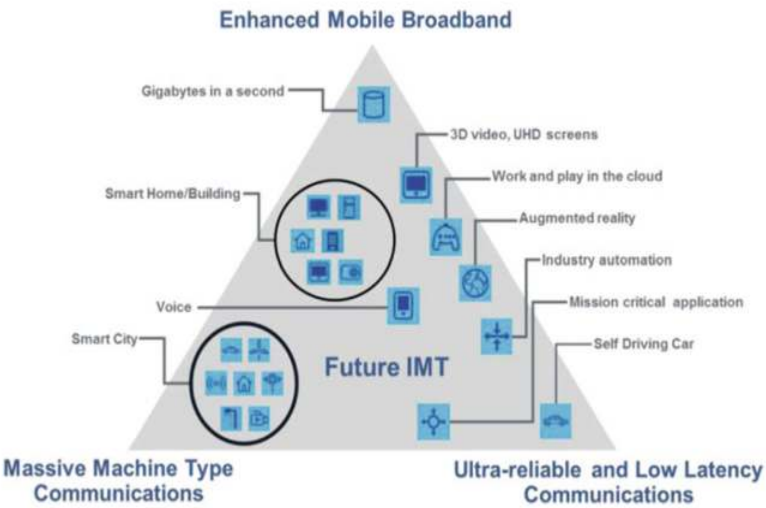

Figure 1.1: 5G Triangle [Wang et al., 2023a].

6G is expected to offer revolutionary enhancements in wireless networks, such as terahertz (THz) communications, integrated sensing and communication (ISAC), artificial intelligence (AI)-driven network management, and RIS. These advancements will enable these strict requirements such as ultra-high data rates, extreme reliability, and seamless connectivity across diverse environments. However, achieving these objectives presents multiple technical challenges, including the unpredictability of the wireless channel, increased complexity in resource allocation, and the need for novel architectures capable of optimizing network performance in real time. The introduction of new frequency bands in the THz spectrum, for example, promises high bandwidth availability but also introduces substantial propagation losses and vulnerability to atmospheric absorption. Overcoming these issues will require sophisticated signal processing techniques, new antenna architectures, and the ability to dynamically adapt transmission parameters to environmental variations.

One of the most critical challenges in wireless communication systems is the stochastic nature of the wireless channel and it is critical to analyse and consider it in future communication systems [Wang et al., 2020]. The radio environment is in-

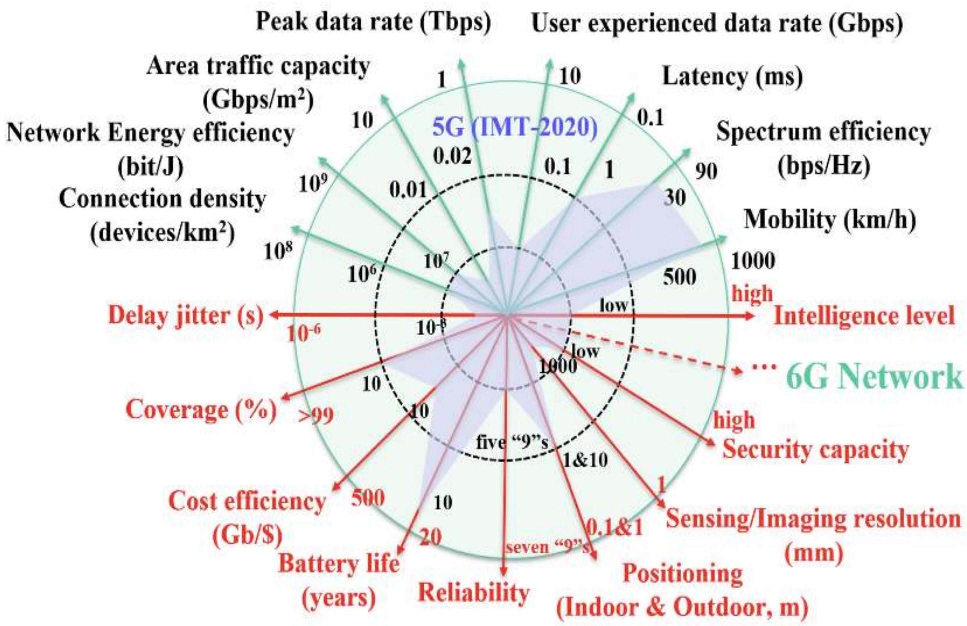

Figure 1.2: 6G Requirements [Jiang and Liu, 2016].

herently dynamic, influenced by factors such as multipath fading, Doppler shifts, and interference from other devices. Current approaches to mitigate these effects include channel estimation, equalization, and adaptive modulation techniques implemented at the transmitter (Tx) and receiver (Rx) [Drakshayini and Kounte, 2022a, Drakshayini and Kounte, 2022b]. However, these techniques are often computationally intensive and rely on imperfect estimations, leading to suboptimal performance. The unpredictable nature of real-world propagation environments further magnify these challenges. Wireless signals experience severe attenuation due to obstacles, weather conditions, and mobility-induced variations, all of which contribute to significant fluctuations in signal strength and quality. Conventional channel estimation techniques attempt to model these variations using statistical methods and machine learning-based prediction models, yet their accuracy is limited by environmental complexity and computational constraints.

Channel estimation methods, such as pilot-based and blind estimation techniques, attempt to predict and compensate for channel variations [Simeone et al., 2004, Shin et al., 2007]. However, these methods suffer from several drawbacks, including increased overhead, high power consumption, and limited effectiveness in high-mobility scenarios. Moreover, while advanced signal processing techniques can mitigate the effects of channel impairments at the Tx or Rx, they do not offer a mechanism to control the propagation environment itself, limiting their effectiveness in achieving robust communication performance. The increasing demand for reliable, high-speed connectivity necessitates a paradigm shift in how wireless networks interact with their surrounding environments. Rather than passively adapting to channel impairments, future networks must incorporate intelligent mechanisms that can dynamically manipulate wireless propagation conditions to ensure optimal performance. Addressing these challenges will require a combination of advanced signal processing techniques, proactive network management strategies, and the integration of emerging technologies such as reconfigurable intelligent surfaces [Basharat et al., 2021, Basar, 2020b, Basar, 2021].

A promising solution to overcome channel-related challenges in 6G networks is the use of RISs. RIS technology enables the manipulation of the wireless environment by dynamically controlling characteristics of reflected electromagnetic waves [Wang and Swindlehurst, 2023]. By intelligently reconfiguring the phase shifts of incident signals, RIS can enhance signal quality, improve spectral efficiency, and reduce interference. The core principle behind RIS involves embedding a large array of passive or active tunable elements into wireless propagation paths. These elements can be dynamically adjusted to alter the way signals are reflected or transmitted, thereby creating optimized propagation conditions for different network scenarios. Unlike traditional relays or beamforming techniques, RIS offers a highly energy-efficient approach to channel control, requiring minimal power consumption and avoiding the need for complex active processing at the signal relay points [Tasci et al., 2022a].

RISs can be categorized into three main types. Passive RIS consists of tunable metasurfaces that reflect signals without requiring active power consumption [Zhang et al., 2022b]. Active RIS, on the other hand, is capable of amplifying incoming signals, thereby improving signal strength at the receiver [Zhang et al., 2022b]. A hybrid RIS combines the benefits of passive and active RIS to achieve better efficiency and flexibility [Yigit et al., 2022]. The operation modes of RIS include reflective mode, where signals are redirected towards intended users to improve coverage, and absorbing mode, which reduces interference by absorbing unwanted signals. Additionally, RIS can operate in refracting or transmissive mode, allowing signals to pass through while controlling their characteristics, as well as in transparent mode, which offers an unobtrusive integration into existing infrastructure such as building windows, enhancing system design flexibility [Wang and Swindlehurst, 2023].

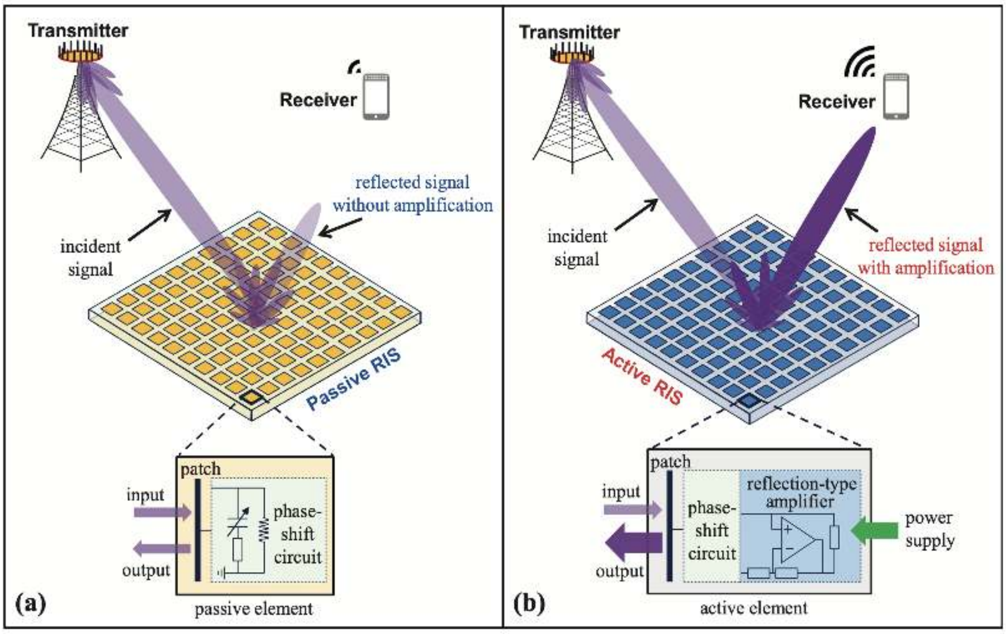

Figure 1.3: Hardware Architectures of Passive and Active RISs [Zhang et al., 2022b].

Current studies on RIS have explored various aspects, including its integration with multiple-input multiple-output (MIMO) systems [Wang et al., 2023b], its role in non-orthogonal multiple access networks [Liu et al., 2022b], and its potential in vehicular and IoT communications [Ai et al., 2021, Niu et al., 2022]. However, the proposed system designs need to be improved in creative manners to meet the strict requirements of future wireless communication systems. Furthermore, existing literature often relies on simplified assumptions, such as perfect channel state information (CSI) and ideal hardware configurations, which may not reflect practical deployment scenarios. Additionally, system-level designs and large-scale implementations of RIS remain underexplored. To fully realize the benefits of RIS, future research must address key challenges such as the development of efficient phase control algorithms, the integration of RIS with practical considerations and low-complexity optimization techniques, and the creation of scalable deployment strategies for real-world communication environments. Moreover, industry stakeholders demand RIS solutions that are cost-effective, easy to deploy, and compatible with current wireless standards, further underscoring the need for practical and commercially viable RIS implementations [Liu et al., 2022a].

1.2 Research Objectives and Contributions

The primary objective of this thesis is to develop and propose novel communication techniques and system designs that integrate RIS with advanced wireless communication paradigms to enhance the performance of next-generation communication systems over-the-air at the RIS, particularly in the context of 6G and beyond. The research contributions can be categorized into the following key areas:

- Novel system designs supported by simulation and theoretical analysis for improved spectral efficiency and communication reliability: This thesis introduces new RIS-assisted wireless communication frameworks that significantly enhance spectral efficiency, BER, and overall system reliability. By proposing innovative schemes and RIS-based strategies, the research develops efficient system models that optimize resource allocation, mitigate interference, and enhance signal transmission under diverse propagation conditions, including scenarios with imperfect CSI. These novel system designs are supported by simulations and theoretical analysis, modeling, and extensive performance evaluations, ensuring a comprehensive understanding of RIS-based communication under different network conditions.

- Practicality, deployment considerations, and real-world feasibility: In contrast to many existing RIS studies that rely on simplified and often unrealistic assumptions, the latter studies in this thesis places a strong emphasis on practical implementation aspects. It investigates network-independent RIS architectures, RIS identification techniques, and deployment strategies, ensuring that the proposed solutions are scalable, efficient, and feasible for real-world wireless networks. Furthermore, the study explores practical use cases, addressing challenges such as hardware constraints, computational efficiency, and compatibility with existing and future wireless infrastructures.

- Low-complexity and energy-efficient communication solutions: The proposed RIS-assisted schemes are designed to maximize system performance while minimizing computational complexity and energy consumption. By leveraging optimized RIS partitioning strategies, hybrid RIS configurations, and efficient detection algorithms, this research ensures that high-performance RIS-based communication can be achieved without excessive processing overhead, making it viable for practical 6G and beyond deployments.

By addressing both theoretical and practical challenges, this thesis contributes to the evolution of RIS-enabled wireless communication, bridging the gap between novel system designs and real-world deployment, ultimately shaping the development of scalable, intelligent, and high-performance 6G communication networks.

1.3 Overview of Thesis Structure

The structure of this thesis is organized as follows:

Chapter 2 explores an OTA virtual equalization technique through the RIS. This chapter demonstrates how RIS phase alignment can effectively eliminate ISI and transform frequency-selective fading channels into frequency-flat channels. A detailed probabilistic analysis is provided to assess the impact of RIS on ISI suppression.

Chapter 3 introduces a novel RIS-assisted uplink NOMA scheme. This chapter investigates the optimization of resource allocation and the improvement of outage probability performance for multiple users. The theoretical framework and extensive simulation results illustrate the benefits of integrating RIS with NOMA for enhanced system performance.

Chapter 4 presents an hybrid-RIS architecture designed for over-the-air IM. This chapter proposes a novel system that combines passive and active RIS elements to enhance spectral efficiency while reducing detection complexity. A low-complexity detection algorithm is introduced, and the system's superiority over benchmark schemes is demonstrated through performance evaluations.

Chapter 5 investigates network-independent RIS architectures by introducing a user-controlled RIS system. This approach enhances signal quality and energy efficiency while eliminating the need for centralized network control and providing a simle yet practical deployment scenario for RISs. The feasibility of such a system is analyzed under real-world constraints.

Chapter 6 explores the RIS identification concept and techniques for mobile networks, addressing critical challenges and concerns. A novel framework for RIS-based network is proposed, introducing an important new RIS identification concept and its benefits to the RIS literature. The effectiveness of various RIS identification techniques is assessed through analysis and simulation results and comprehensive discussions.

Chapter 7 presents a power-differentiated dual-code index modulation (RIS-PD-DCIM) scheme. This technique leverages optimal RIS partitioning strategies to improve spectral efficiency and performance while maintaining low-complexity detection. Simulation results and analysis confirm the advantages of this approach over existing RIS-based modulation schemes.

Chapter 8 concludes the thesis by summarizing the key contributions and findings. This chapter discusses the broader implications of RIS-aided communication in 6G networks and highlights potential future research directions.

This structured approach provides a comprehensive exploration of over-the-air methods and practical implementations of RIS-aided communication systems, addressing key challenges in wireless communication networks and paving the way for their seamless integration into 6G and beyond.

1.4 Summary

This thesis presents a comprehensive study of over-the-air techniques and system designs for RIS communication systems, contributing to the advancement of 6G and beyond wireless networks. Initially, the focus is placed on novel theoretical frameworks, system designs, and performance analyses that explore the integration of RIS with advanced communication paradigms, such as IM, NOMA, and hybrid RIS architectures. These studies introduce new methodologies to enhance spectral efficiency, BER, interference mitigation, and system scalability, addressing fundamental challenges in next-generation wireless communication.

Beyond theoretical advancements, this research also examines the practical aspects of RIS deployment, including hardware constraints, real-world channel effects, and implementation challenges. While many RIS studies in the literature assume idealized models and perfect CSI, this thesis takes a step further by analyzing real-world feasibility, exploring network-independent RIS architectures, practical RIS identification techniques, and scalable deployment strategies. These contributions bridge the gap between theoretical innovations and real-world applications, ensuring that the proposed RIS techniques are not only highly efficient in simulations but also viable for practical deployment.

The findings of this thesis provide a balanced approach, combining innovative system designs with practical considerations, paving the way for flexible, scalable, and high-performance communication systems that align with the evolving needs of future 6G networks.

Chapter 2

OVER-THE-AIR EQUALIZATION WITH RECONFIGURABLE INTELLIGENT SURFACES

2.1 Preface

RIS-empowered communications is on the rise and is a promising technology envisioned to aid in 6G and beyond wireless communication networks. RISs can manipulate impinging waves through their electromagnetic elements enabling some sort of control over the wireless channel. In this chapter, the potential of RIS technology is explored to perform a sort of virtual equalization over-the-air for frequency-selective channels whereas, equalization is generally conducted at either the transmitter or receiver in conventional communication systems. Specifically, using an RIS, the frequency-selective channel from the transmitter to the RIS is transformed to a frequency-flat channel through elimination of ISI components at the receiver. ISI is eliminated by adjusting the phases of impinging signals particularly to maximize the incoming signal of the strongest tap. First, a general end-to-end system model is provided and a continuous to discrete-time signal model is presented. Subsequently, a probabilistic analysis for elimination of ISI terms is conducted and reinforced with computer simulations. Furthermore, a theoretical error probability analysis is performed along with computer simulations. It is analyzed and demonstrated that conventional RIS phase alignment methods, can successfully eliminate ISI and the RIS-aided communication channel can be converted from frequency-selective to frequency-flat.

2.2 Introduction

Commercial 5G wireless network standards have successfully been developed and countries are striving to adapt to 5G as means to not trail behind. Meanwhile, the race for the next generation wireless has already begun as academia and industry advance towards 6G [Saad et al., 2020, Zhu et al., 2020, Yizhan et al., 2020]. The trend for each generation is known where the 'odd' generations (1G, 3G, 5G) have been regarded as evolutions while the even generations (2G, 4G) might be perceived as revolutions for the communication world, therefore, it is the perfect time to envision a revolution with 6G.

Future 6G applications/use-cases demand solutions to combat challenging communication engineering dilemmas. Several of these applications include truly immersive virtual/augmented reality, holographic communication, remote education and much more [Doğan-Tusha et al., 2020]. These applications require high reliability, data rates, and security all in conjunction with low-latency. Future wireless networks, particularly at the physical layer, require unique approaches in terms of flexibility, novel waveforms and techniques to satisfy its stringent requirements.

In light of the above mentioned, to tackle some of these 6G demands, there has been a growing interest among the telecommunication community in manipulating and controlling the wireless propagation environment. Reconfigurable intelligent surface (RIS)-empowered communications, is currently a hot topic with the aim of improving signal quality and dynamically reconfiguring the wireless channel [Wu and Zhang, 2020, El-Mossallamy et al., 2020, Basar and Yildirim, 2021, Gacanin and Di Renzo, 2020, Alfattani et al., 2021]. RIS has emerged as a cost-effective solution to manipulate the propagation environment with it's unique and effective functionalities such as controllable reflecting, absorbing, and shifting phases without buffering or processing the incoming signals, hence, it is qualified as a passive component [Basar, 2019].

Recently, numerous noteworthy studies have been carried out demonstrating the potential of RIS technologies towards 6G wireless networks. In the literature, RISs have been integrated with existing technologies such as orthogonal frequency division multiplexing (OFDM) and multiple-input multiple-output (MIMO) to enhance their performance. Solutions have been proposed for fast and efficient channel estimation, maximizing the average sum-rate over subcarriers, and maximizing the downlink achievable rate for the user by jointly optimizing the transmit power allocation at the BS and the passive reflection coefficients at the RIS [Yang et al., 2019, Zheng and Zhang, 2020, Yang et al., 2020e, Yang et al., 2020d, Li et al., 2021, Lin et al., 2020, Zheng et al., 2020]. The RIS concept has also been investigated to work collectively with related approaches, such as relaying and backscatter communications. Flexible and cost/power effective hybrid transmission schemes involving a relay and a passive RIS are presented in [Yildirim et al., 2021] while [Zhang et al., 2020a] investigates the limitation of phase shifts for practical RIS systems. In addition, fair comparisons have been made between relays and RISs based on SINR maximization for different scenarios such as varying pathloss models and RIS positionings [Ye et al., 2021]. Furthermore, RIS channel models have been investigated thoroughly for different scenarios such as indoor and outdoor applications and their benefits have been emphasized [Yildirim et al., 2020, Kilinc et al., 2021a].

In general, RIS literature mostly tends to focus on maximizing the sum-rate/ achievable-rate of a wireless communication system by adjusting the reflection phases of incoming signals to the RIS, hence, improving the signal-to-noise ratio (SNR) at the target receiver or receivers [Wu et al., 2021b]. However, there have been other captivating studies with different approaches such as investigating the operation of an RIS under predictable mobility considering Doppler effect and delay spread [Matthiesen et al., 2020], feasibility of mitigating multipath fading and Doppler effects stemming from mobile receivers [Basar, 2021], optimizing the orientation and distance of the RIS from the users and base-station to maximize cell-coverage [Zeng et al., 2021a] and so on [Huang et al., 2019a, Hou et al., 2020, Zhang et al., 2020b, Hong et al., 2020, Li et al., 2020, Basar, 2020b]. In general, studies in the literature mostly consider flat-fading systems, and frequency-selective fading is not sufficiently investigated within the context of RIS systems except for some promising OFDM-based RIS solutions. Conventionally, for systems without OFDM, equalization is applied at the receiver (Rx) to combat frequency selectivity; however, it is not always efficient. For example, numerous systems, such as Internet-of-Things (IoT) devices, will be connected wirelessly in the future and it is not efficient for them to implement complex equalization algorithms. Thus, over-the-air equalization with a passive RIS is an efficient alternative for these devices requiring equalization. To the best of the authors' knowledge, existing studies in the literature severely lacks a thorough analysis of equalization methods with the aid of an RIS. Specifically, ISI caused by multipath fading has been reduced by optimizing the phase shifts at the RIS with the help of an iterative algorithm very recently [Zhang et al., 2021a]. However, this study does not provide a theoretical background or a probabilistic analysis on the elimination of ISI. Nonetheless, a unified framework for multipath fading mitigation as well as a comprehensive analysis on the potential effects of ISI are still missing in the open literature.

Against this background, this chapter analyzes an RIS-aided wireless network and follows a comprehensive signal processing analysis to show that conventional RIS phase alignment schemes may be leveraged to equalize the channel over-the-air. In other words, it is shown that the considered system transforms the frequency-selective channel between the transmitter (Tx) and the RIS and/or RIS and the receiver (Rx) to frequency-flat, resulting in a end-to-end frequency flat channel from the perspective of the Rx. Specifically, the RIS adjusts its phases to eliminate only the phase terms of the strongest tap from the propagation channel. Thus, only the magnitude of the strongest tap has been boosted in a clever manner using the RIS while the other non-optimized taps are regarded as ISI terms. In other words, the effect of the ISI terms are alleviated by maximizing the desired tap of the channel response. In the literature, existing studies amplify the strongest tap to enhance communication performance, however, this study primarily aims to analyze and show that the ISI is also eliminated with the help of the RIS. We show that when the desired tap becomes at least 10 times greater in terms of squared magnitude, the ISI terms become negligible, hence, reliable transmission will be provided by suppressing the effect of ISI terms. Unlike most of the studies in the RIS literature, which aims to maximize the sum-rate, capacity or other kind of performance indicators, our primary concern in this chapter is to exploit the RIS from the perspective of ISI minimization. Rather than proposing a new system, our idea is based on the existing RIS systems subject to the frequency-selective fading channels. The considered system is practically better operated in small devices in which multi-carrier waveforms cannot be utilized to combat with ISI. The contributions of this study can be summarized and highlighted as follows:

- A unified framework is proposed to virtually eliminate the frequency-selectivity of the end-to-end system by alleviating the effect of ISI resulting from multi-path components.

- A thorough end-to-end system model of the proposed scheme from continuous-time to discrete-time domain is provided and analyzed along with computer simulations.

- The ISI elimination probability is calculated for different configurations using a probabilistic approach.

- A theoretical error probability analysis is provided along with computer simulation results for varying parameters and scenarios.

The rest of the chapter can be summarized as follows. In chapter 2.3, the generalized end-to-end system model of the proposed scheme is presented. In chapter 2.4, an analysis of the probability of ISI elimination for different scenarios is conducted. chapter 2.5 provides the error probability analysis of the system and in chapter 2.6, computer simulation results are given. Finally, in chapter 2.7 the chapter is concluded with the final remarks.

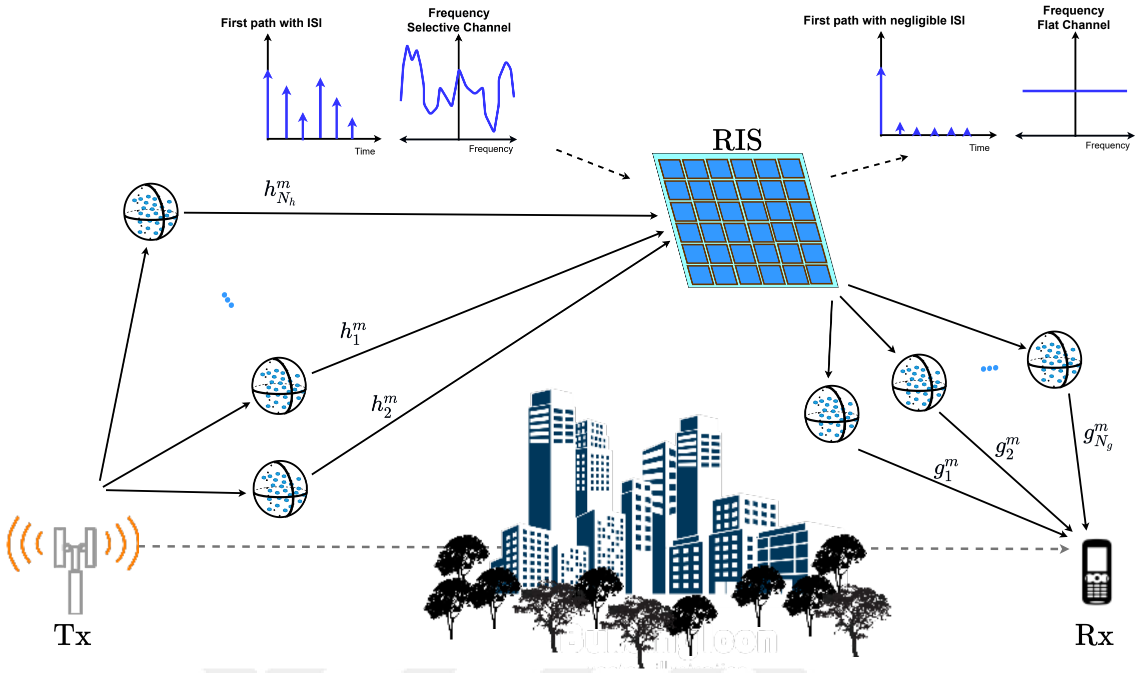

Figure 2.1: Proposed over-the-air equalization system model with N_h-paths between Tx-RIS and N_g paths between the RIS-Rx.

2.3 End-To-End System Model

In this cahpter, we consider a linear time-invariant (LTI) and wideband communication system in the presence of an RIS and present our end-to-end system model. For traceability, a user-friendly introduction in terms of signal processing steps is provided and we progress step by step to illustrate the affect of the RIS for a frequency selective channel.

In wideband communication systems, the symbol time T is shorter than the inverse of coherence bandwidth, that is, the delay spread. Since the multipath delay spread is larger than the symbol time, different multipath components interfere with each other. Therefore, in general, the multipath components of this system are resolvable and the difference of the delays between the components significantly exceeds the symbol duration. This interference results in a well known distortion called ISI which makes the channel frequency-selective. The goal of the proposed system is to virtually eliminate ISI via an RIS and transform the end-to-end frequency-selective channel to frequency-flat, i.e., by accomplishing some sort of virtual equalization over-the-air.

Under the LTI assumption, we can express a general communication system's received continuous-time signal $y(t)$ in the absence of noise using the convolution integral as

$$y(t) = \int_{-\infty}^{\infty} h_c(\tau)x(t-\tau)d\tau \tag{2.1}$$

where $h_c(t)$ is the end-to-end channel impulse response, $x(t)$ is the transmitted signal, and τ is the delay term. It is possible to transition to discrete-time by sampling the continuous-time signal $y(t)$, and rewriting the communication signal model as

$$y[n] = \sum_{k=-\infty}^{\infty} h[k]x[n-k]. \tag{2.2}$$

In baseband, the transmitted signal $x(t)$, with bandwidth $B/2$ Hz, is band-limited that is the input to an LTI-type communication system with impulse response $h_c(t)$. Since the input is band-limited, only the portion of $h_c(t)$ that exists in the bandwidth of $x(t)$ is important to us. We can obtain the continuous-time complex baseband channel as [Heath Jr, 2017, Eq. (3.348)]

$$h(t) = B \int \mathrm{sinc}(B(t-\tau))h_c(\tau)e^{j2\pi f_c \tau} d\tau, \tag{2.3}$$

where B and f_c stand for the complete bandwidth of the ideal lowpass filter and the operating frequency, respectively. In this chapter, we will consider three scenarios of frequency-selectivity: Tx-RIS is frequency-selective while RIS-Rx is frequency flat, Tx-RIS is frequency flat while RIS-Rx is frequency-selective and when the Tx-RIS and RIS-Rx channels are both frequency-selective. As illustrated in Fig. 2.1, an outdoor and RIS-assisted communication system is considered under the the blocked line-of-sight (LOS) path between the Tx and Rx. Here, we consider the most general case where the channel from the Tx to the RIS is frequency-selective and from the RIS to the Rx is also frequency-selective. When the RIS is near the Tx or Rx, which is a common assumption in the literature, the corresponding channel may be considered frequency-flat due to the close proximity of the RIS to the terminals. It should be noted that the analysis when the RIS is close to the Rx also applies to the case when the RIS is close to the Tx. Finally, we provide an additional discussion by considering the direct Tx-Rx link in chapter 2.4.4. The RIS is equipped with M passive reflecting elements that may be adjusted according to the wireless channel. In Fig. 2.1, a general system with N_h paths from the Tx to the RIS and N_g paths from the RIS to the Rx is presented. We assume a frequency-selective channel between both the Tx-RIS and RIS-Rx, that is, all the multipath components N_h and N_g are resolvable. The continuous-time impulse response of the end-to-end channel in Fig. 2.1 can be given as

$$h_c(t) = \sum_{l_1=1}^{N_h} \sum_{l_2=1}^{N_g} \sum_{m=1}^{M} \alpha_{l_1} \beta_{l_2} \delta(t - \tau_{l_1}^m - \xi_{l_2}^m) e^{j\theta_m}, \tag{2.4}$$

where α_{l_1}, β_{l_2}, $\tau_{l_1}^m$, $\xi_{l_2}^m$, represent the complex channel coefficients and delays of the l_1th and l_2th path through the mth RIS element, corresponding to the Tx-RIS and RIS-Rx channels, respectively. Furthermore, $e^{j\theta_m}$ represents the adjustable phase term for the mth RIS element. Since the RIS acts as an LTI filter, $e^{j\theta_m}$ is not dependent on time for one symbol duration.

The continuous-time channel response in (2.4) can be written in discrete form as follows [Heath Jr, 2017, Eq. (3.386)]

$$h[k] = Th(kT), \tag{2.5}$$

where $T = \frac{1}{B}$. By applying an ideal lowpass filter, with sinc type Nyquist pulse shaping, and the same bandwidth as the input signal similarly from (2.3), we may simplify (2.4) to discrete form by using (2.5) and using [Heath Jr, 2017, Eq. (3.385)] obtain

$$h[n] = \int \text{sinc}(n - B\tau) h_c(\tau) e^{-j2\pi f_c \tau} d\tau = \tag{2.6}$$
$$\sum_{l_1=1}^{N_h} \sum_{l_2=1}^{N_g} \sum_{m=1}^{M} \alpha_{l_1} \beta_{l_2} e^{j\theta_m} \times \text{sinc}(n - B(\tau_{l_1} + \xi_{l_2})) e^{-j2\pi f_c (\tau_{l_1}^m + \xi_{l_2}^m)}.$$

It should be noted that since the delay differences coming from the RIS elements are insignificant compared to symbol duration, the $(\cdot)^m$ terms stemming from (2.4) inside the sinc function in (2.6) are removed and the delay for the 1st RIS element is used for all RIS elements. In (2.6), $\tau_{l_1} + \xi_{l_2}$ may be a fraction of a symbol period resulting in an impairment where the receiver does not sample precisely at the right time. Therefore, to counter this impairment, symbol synchronization is employed at the Rx to fix the sample timing error by enabling the delays $\tau_{l_1}+\xi_{l_2}$ to become integer fractions of the symbol duration [Heath Jr, 2017]. When symbol synchronization is applied at the receiver, (2.6) can be re-expressed as follows [Heath Jr, 2017]

$$h[n] = \sum_{l_1=1}^{N_h} \sum_{l_2=1}^{N_g} \sum_{m=1}^{M} h_{l_1}^m g_{l_2}^m e^{j\theta_m} \delta(n - B\tilde{\tau}_{l_1} - B\tilde{\xi}_{l_2}), \tag{2.7}$$

where $\tilde{\tau}$ and $\tilde{\xi}$ represent the non-fractional (integer) delays of the paths after symbol synchronization. It is worth noting that the $\delta(\cdot)$ in (2.7) is the Kronecker delta function while in (2.4) is direc delta. Additionally, the delay terms in the exponential of (2.6) are now combined with the channel coefficients for the m^{th} element of each path, which are denoted as

$$\begin{aligned} h_{l_1}^m &= \alpha_{l_1} e^{-j2\pi f_c \tau_{l_1}^m}, \\ g_{l_2}^m &= \beta_{l_2} e^{-j2\pi f_c \xi_{l_2}^m}. \end{aligned} \tag{2.8}$$

Hereby, the complex baseband received signal $y(t)$ may be written in discrete form as in (2.2), by sampling at integer multiples of T as $y[n] = y(nT)$. The received signal corrupted with additive white Gaussian noise (AWGN) samples $w[n]$ where $w \sim \mathcal{CN}(0, W_0)$ with $\mathcal{CN}(0, \sigma^2)$ denoting complex Gaussian distribution with variance σ^2, may be expressed as

$$y[n] = \sum_{l_1=1}^{N_h} \sum_{l_2=1}^{N_g} \sum_{m=1}^{M} h_{l_1}^m g_{l_2}^m e^{j\theta_m} x[n - B\tilde{\tau}_{l_1} - B\tilde{\xi}_{l_2}] + w[n]. \tag{2.9}$$

For simplicity, throughout the chapter we denote the strongest tap with the first tap where $(l_1, l_2) = (1, 1)$. If we arrange the first path term and other terms separately, which will be treated as ISI later on, the received signal can be reorganized as

$$y[n] = \sum_{m=1}^{M} h_1^m g_1^m e^{j\theta_m} x[n - B\tilde{\tau}_1 - B\tilde{\xi}_1] + \sum_{\substack{l_1=1 \\ (l_1,l_2)\neq(1,1)}}^{N_h} \sum_{l_2=1}^{N_g} \sum_{m=1}^{M} h_{l_1}^m g_{l_2}^m e^{j\theta_m} x[n - B\tilde{\tau}_{l_1} - B\tilde{\xi}_{l_2}] + w[n]. \tag{2.10}$$

Even when the symbol timing has been corrected, another impairment occurs with larger delays due to an unknown propagation delay, which is a multiple of the symbol period. These integer offsets create a mismatch between the indices of the transmitted and received symbols, and the correction of this impairment requires frame synchronization [Heath Jr, 2017]. After frame synchronization is applied, the discrete-time received signal in (2.10) is rewritten as

$$y[n] = \sum_{m=1}^{M} h_1^m g_1^m e^{j\theta_m} x[n] + \sum_{\substack{l_1=1 \\ (l_1,l_2)\neq(1,1)}}^{N_h} \sum_{l_2=1}^{N_g} \sum_{m=1}^{M} h_{l_1}^m g_{l_2}^m e^{j\theta_m} \times x[n - ((B\tilde{\tau}_{l_1} + B\tilde{\xi}_{l_2}) - (B\tilde{\tau}_1 + B\tilde{\xi}_1))] + w[n], \tag{2.11}$$

where $h_1^m g_1^m = |h_1^m||g_1^m|e^{j\phi_m}$, $h_{l_1}^m g_{l_2}^m = |h_{l_1}^m||g_{l_2}^m|e^{j\psi_m^{l_1,l_2}}$, and $|\cdot|$ is the absolute value operator. Hence, we may express the signal-to-interference-noise ratio (SINR) γ, of the system as follows:

$$\gamma = \frac{E_s \left|\sum_{m=1}^{M} |h_1^m||g_1^m|e^{j\phi_m} e^{j\theta_m}\right|^2}{E_s \sum_{\substack{l_1=1 \\ (l_1,l_2)\neq(1,1)}}^{N_h} \sum_{l_2=1}^{N_g} \left|\sum_{m=1}^{M} |h_{l_1}^m||g_{l_2}^m|e^{j\psi_m^{l_1,l_2}} e^{j\theta_m}\right|^2 + W_0}. \tag{2.12}$$

Here E_s is the energy of the transmitted signal, $\phi_m = \angle(h_1^m g_1^m)$, and $\psi_m^{l_1,l_2} = \angle(h_{l_1}^m g_{l_2}^m)$, where $\angle(\cdot)$ denotes the phase of a complex term. By adjusting the RIS phases according to the first tap as $\theta_m = -\phi_m$, the phase terms of the numerator are eliminated and γ is simplified to

$$\gamma = \frac{E_s (\sum_{m=1}^{M} |h_1^m||g_1^m|)^2}{E_s \sum_{\substack{l_1=1 \\ (l_1,l_2)\neq(1,1)}}^{N_h} \sum_{l_2=1}^{N_g} \left|\sum_{m=1}^{M} |h_{l_1}^m||g_{l_2}^m|e^{j\psi_m^{l_1,l_2}} e^{j\theta_m}\right|^2 + W_0}. \tag{2.13}$$

Here we aim to arrange $e^{j\theta_m}$ specifically to cancel out the phase terms of the first path ϕ_m, that is, the phase of the numerator. Hence, the numerator of the SINR becomes real valued while the denominator with the ISI components are complex and deteriorated with the additional random phases. In this way, we can maximize the first and strongest tap of the system making it several times more powerful in terms of magnitude than the combined ISI terms, which will be further analyzed in chapter 2.4 to eliminate the ISI effect.

2.4 Inter-Symbol Interference Elimination: A Probabilistic Approach

In this chapter, the ISI elimination concept introduced in chapter 2.2 is analyzed with a detailed probabilistic approach via computer simulation results. Two scenarios of an RIS system are analyzed. The first is when the RIS is close to the Tx or Rx resulting in the Tx-RIS or RIS-Rx link to be frequency flat while the other is frequency selective, characterized by Scenario 1. On the other hand, the latter case is when both Tx-RIS and RIS-Rx links of the RIS are frequency selective (Scenario 2).

2.4.1 Scenario 1

In this this subchapter, we assume only one path from the RIS to the Rx ($N_g = 1$) since the corresponding channel experiences flat fading due to close positioning of the RIS to the Rx. It should be noted that for the case of ($N_h = 1$), the same results in this chapter are valid. We remove the underscore and denote the single path from the RIS-Rx simply as g^m. The channel fading coefficients of the Tx-RIS path, $h_{l_1}^m$ where $l_1 = 1, \cdots, N_h$ and the single path from the RIS to the Rx, g^m, reflecting from the m^{th} RIS element $m = 1, \ldots, M$ are independent and identically distributed under the Rayleigh fading assumption for a worst-case scenario analysis. Hence, these channel coefficients follow the distribution $h_{l_1}^m, g^m \sim \mathcal{CN}(0, \sigma_i^2)$, where σ_i^2 and $i \in \{h_l, g\}$ is a function of the large scale path loss. We may express the end-to-end channels for the first path and the ISI paths respectively as A and B:

$$A = \sum_{m=1}^{M} h_1^m e^{j\theta_m} g^m = \sum_{m=1}^{M} |h_1^m||g^m|,$$
$$B = \sum_{l_1=2}^{N_h} b_{l_1} = \sum_{l_1=2}^{N_h} \sum_{m=1}^{M} h_{l_1}^m e^{j\theta_m} g^m, \quad (2.14)$$

where $e^{j\theta_m} = e^{-j(\angle h_1^m + \angle g^m)}$. Since h_1^m and g^m are independently Rayleigh distributed random variables, the mean and the variance of their product are $\mathrm{E}[|h_1^m||g^m|] = \frac{\sigma_{h_1}\sigma_g\pi}{4}$ and $\mathrm{VAR}[|h_1^m||g^m|] = \sigma_{h_1}^2\sigma_g^2(1-\frac{\pi^2}{16})$, respectively. When the number of RIS elements M is significantly large, from the Central Limit Theorem, A converges to a real Gaussian distribution random variable with $A \sim \mathcal{N}(\frac{M\pi\sigma_{h_1}\sigma_g}{4},\, M\sigma_{h_1}^2\sigma_g^2(1-\frac{\pi^2}{16}))$. On the other hand, since the phase terms exist in the ISI paths, b_{l_1} converges to a complex Gaussian random variable. The mean and variance of the product of the terms in b_{l_1} are calculated as $\mathrm{E}[h_{l_1}^m e^{j\theta_m} g^m] = 0$ and $\mathrm{VAR}[h_{l_1}^m e^{j\theta_m} g^m] = M\sigma_{h_{l_1}}^2\sigma_g^2$ resulting in $B \sim \mathcal{CN}(0,\, M(N_h-1)\sigma_{h_{l_1}}^2\sigma_g^2)$. As it can be seen from (14), A and the B have g^m as a common term; however, they are independent since they are uncorrelated and Gaussian distributed. To find their correlation coefficient, the covariance of A and B is required and since B has zero mean, it may be expressed as

$$\mathrm{E}[AB] = \mathrm{E}\left[\left(\sum_{m=1}^{M} h_1^m e^{j\theta_m} g^m\right)\left(\sum_{l_1=2}^{N_h}\sum_{m=1}^{M} h_{l_1}^m e^{j\theta_m} g^m\right)\right]. \quad (2.15)$$

After adjusting the RIS phases according to the first path, (2.15) may be re-expressed as

$$\mathrm{E}[AB] = \mathrm{E}\left[\left(\sum_{m=1}^{M} |h_1^m||g^m|\right)\left(\sum_{l_1=2}^{N_h}\sum_{m=1}^{M} h_{l_1}^m e^{-j\angle h_1^m}|g^m|\right)\right]. \quad (2.16)$$

Here, h_{l_1} is a complex Gaussian term with zero mean hence, $\mathrm{E}[AB] = 0$. Therefore, the correlation coefficient of A and B is also zero resulting in A and B being uncorrelated. Furthermore, they are Gaussian distributed and independent.

We assume that when A is at least 10 times greater in squared magnitude than the power of the ISI terms, the ISI terms will be negligible and can be ignored. To generalize this, the probability that A is X times greater in squared magnitude than the sum of b_{l_1} terms, where $b_{l_1} = \sum_{m=1}^{M} h_{l_1}^{m} e^{-j\angle h_1}|g^m|$ also converges to a complex Gaussian random variable, may be expressed as follows:

$$P\left(A^2 - X\sum_{l_1=2}^{N_h}|b_{l_1}|^2 > 0\right) = 1 - P(C < 0) = 1 - \int_{-\infty}^{0} f_C(c)dc, \quad (2.17)$$

where $C = A^2 - X\sum_{l_1=2}^{N_h}|b_{l_1}|^2$, and $f_C(c)$ is the probability density function (PDF) of C. Therefore, to ensure successful ISI elimination, we assume that X would be at least 10. In (17), A^2 and $\sum_{l_1=2}^{N_h}|b_{l_1}|^2$ follow non-central chi-square distribution with one degree of freedom and central chi-square distribution with $2(N_h - 1)$ degrees of freedom, respectively. Here, C is the difference of independent non-central and central chi-squared random variables [Simon, 2007]. Thus, we would need to integrate the PDF of the difference of non-central chi-squared and central chi-squared random variables accordingly. However, the PDF is expressed in the form of infinite series in Whittaker functions where themselves are expressed in terms of the confluent hypergeometric function. Due to the complexity of the PDF calculation and the absence of functions in standard mathematical software as mentioned in [Simon, 2007], it is extremely complicated to approach this method. On the other hand, the characteristic function (CF) of C is simply derived and expressed as:

$$\Psi_C(\omega) = \frac{1}{(1 - 2j\omega\sigma_1^2)^{0.5}(1 + 2j\omega\sigma_2^2)^{(N_h-1)})}\exp\left(\frac{j\omega\mu_1^2}{1 - 2j\omega\sigma_1^2}\right) \quad (2.18)$$

where μ_1^2, σ_1^2, and σ_2^2 stand for the non-centrality parameter which is the mean squared of A, variance of A, and variance of $\sqrt{X}B$, respectively. Since M is directly multiplied with a power of σ_i, in the statistics provided for A and B, for a small σ_i the number of RIS elements M is not expected to significantly affect the result. Using the Gil-Pelaez's inversion formula [Mathai and Provost, 1992a], it is possible to obtain the cumulative distribution function (CDF) of this difference of chi-squared random variables as

$$F_C(c) = \frac{1}{2} - \int_{0}^{\infty} \frac{\Im\{e^{-jwc}\Psi_C(w)\}}{w\pi}dw \quad (2.19)$$

where $\Im$ denotes the imaginary part, $F_C(c) = P(C \leq c)$ is the CDF and $\Psi_C(w)$ is the CF of C. Solving for $c = 0$ and using numerical integration, the probability of A being X times greater than B may be obtained.

2.4.2 Scenario 2

In this subchapter, the scenario where the channels from the Tx-RIS and RIS-Rx are both frequency selective is taken into consideration. Similar to the previous case, the end-to-end channels for the first path and the ISI paths may be represented as

$$\begin{aligned} A &= \sum_{m=1}^{M} h_1^m e^{j\theta_m} g_1^m = \sum_{m=1}^{M} |h_1^m||g_1^m|, \\ B &= \sum_{l_1=2}^{N_h}\sum_{l_2=2}^{N_g} b_{l_1,l_2} = \sum_{l_1=2}^{N_h}\sum_{l_2=2}^{N_g}\sum_{m=1}^{M} h_{l_1}^m e^{j\theta_m} g_{l_2}^m, \end{aligned} \tag{2.20}$$

where $e^{j\theta_m} = e^{-j(\angle h_1^m + \angle g_1^m)}$. The mean and the variance of A remains the same and A has the same distribution. On the other hand, the mean and variance of b_{l_1,l_2} can be recalculated as $\mathrm{E}[h_{l_1}^m e^{j\theta_m} g_{l_2}^m] = 0$ and $\mathrm{VAR}[h_{l_1}^m e^{j\theta_m} g_{l_2}^m] = M\sigma_{h_{l_1}}^2 \sigma_{g_{l_2}}^2$ resulting in $B \sim \mathcal{CN}(0,\, M(N_g-1)(N_h-1)\sigma_{h_{l_1}}^2\sigma_{g_{l_2}}^2)$. A and B remain uncorrelated which can be seen by reapplying (2.15) and (2.16) to obtain

$$\mathrm{E}[AB] = \mathrm{E}\left[\left(\sum_{m=1}^{M} |h_1^m||g_1^m|\right)\left(\sum_{l_1=2}^{N_h}\sum_{l_2=2}^{N_g}\sum_{m=1}^{M} h_{l_1}^m e^{-j\angle\theta_m} g_{l_2}^m\right)\right]. \tag{2.21}$$

the probability that A is X times greater in squared magnitude than B may be expressed as follows:

$$P\left(A^2 - X\sum_{l_1=2}^{N_h}\sum_{l_2=2}^{N_g} |b_{l_1,l_2}|^2 > 0\right) = 1 - P(C<0) = 1 - \int_{-\infty}^{0} f_C(c)dc, \tag{2.22}$$

where $C = A^2 - X\sum_{l_1=2}^{N_h}\sum_{l_2=2}^{N_g} |b_{l_1,l_2}|^2$. In (2.22), A^2 and $\sum_{l_1=2}^{N_h}\sum_{l_2=2}^{N_g} |b_{l_1,l_2}|^2$ follow non-central chi-square distribution with one degree of freedom and central chi-square distribution with $2(N_h-1)(N_g-1)$ degrees of freedom, respectively. Due to the complexity of the resulting PDF, we proceed with the Gil-Pelaez's inversion formula and the CF once more. The CF of C may be expressed as follows:

$$\Psi_C(\omega) = \frac{1}{(1-2j\omega\sigma_1^2)^{0.5}(1+2j\omega\sigma_2^2)^{(N_h-1)(N_g-1)}} \exp\left(\frac{j\omega\mu_1^2}{1-2j\omega\sigma_1^2}\right), \tag{2.23}$$

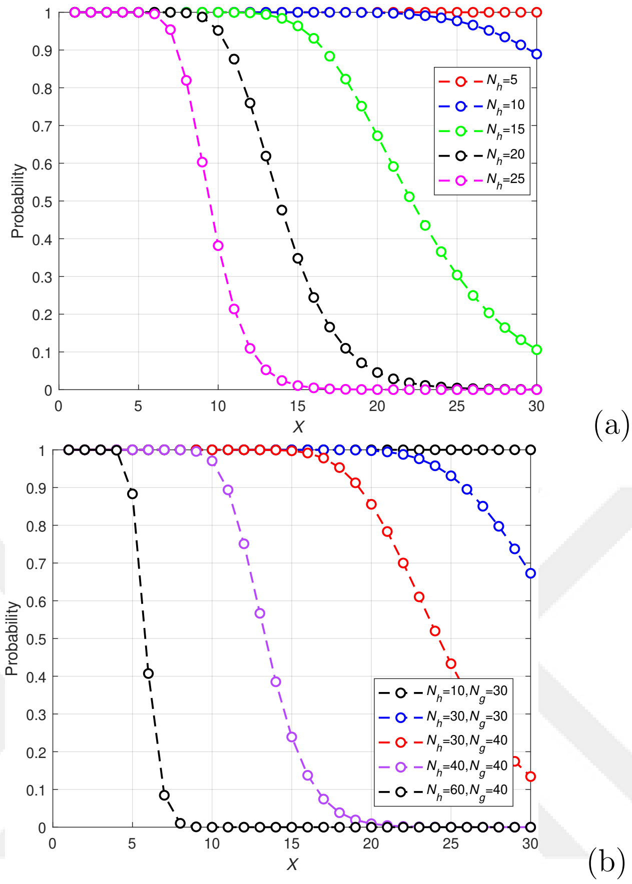

Figure 2.2: Probability of RIS-induced first tap channel coefficient being X times greater in squared magnitude than ISI term for $M = 256$ and varying N_h for (a) Scenario 1 where $\sigma_i = 10^{-3}$ and (b) Scenario 2 where $\sigma_i = 10^{-2}$.

where μ_1^2, σ_1^2, and σ_2^2 stand for the non-centrality parameter which is the mean square of A, variance of A, and variance of $\sqrt{X}B$, respectively. Using (2.19), we may obtain the CDF $F_C(c) = P(C \leq c)$, solve for $c = 0$ and calculate the probability of A being at least 10 times greater than B using numerical integration.

2.4.3 ISI Elimination for Scenarios 1 and 2

Computer simulation results in this chapter provide a clear visualization of the probability of the strongest path being X times greater in squared magnitude than the combined ISI paths allowing us to clearly express that they are negligible and eliminated. Both scenarios of ISI elimination are discussed.

In Fig. 2.2(a), we provide the ISI elimination probability for Scenario 1 for varying N_h at $M = 256$ and $\sigma_i = 10^{-2}$. It should be noted that for practical values of $\sigma_i < 10^{-3}$ we observe very high probabilities of ISI elimination and purposefully increased σ_i for observational purposes. It can be seen that under the worst-case scenario with a uniform power-delay-profile (PDP), high σ_i, and Rayleigh distribution, the probability of the first path being at least $X = 10$ times greater in squared magnitude than the ISI paths is about 99% at $N_h = 15$. In general, Fig. 2.2(a) demonstrates that for varying total number of paths (N_h), i.e., $N_h - 1$ ISI paths, the probability that the first tap is 10 times greater in squared magnitude than the combined ISI terms is very high for even severe conditions. It can also be seen that not only is it 10 times greater, the first tap is more than 30 times greater in squared magnitude than the combined ISI paths for many of cases. In Fig. 2.2(b), we vary both N_h and N_g for $M = 32$ and $\sigma_i = 10^{-3}$. Even with frequency selectivity at both links of the RIS and numerous ISI paths, for practical values of σ_i the ISI is completely eliminated. For a severe number of ISI taps at high fading power, we can still see that the ISI is eliminated 98% of the time for $N_h = 40, N_g = 40$. Even though the ISI is almost completely negligible in scenarios with smaller σ_i, we can see that as the number of ISI terms increases, the probability of the ISI elimination degrades. However, the probability of ISI elimination for even a large number of ISI paths is high. In Fig. 2.3, N_h and N_g are set to constant values for both scenarios of frequency selectivity to examine the performance of varying M values, i.e., RIS sizes. It can be seen that for a small σ_i, the probability of ISI elimination is unchanged with the RIS size, because as M increases, the results stay the same and the curves fully overlap each other for all scenarios along with cases of N_h and N_g. This goes for any RIS size and number of paths. As mentioned previously, this is because in the statistics of A and B, M is multiplied with σ_i values thus, for a small σ_i, the effect of M in the probability of elimination is greatly reduced. On the other hand, if σ_i were to be a very large value which is not practical, a change in M may impact the results and the curves in Fig. 2.3 would not overlap.

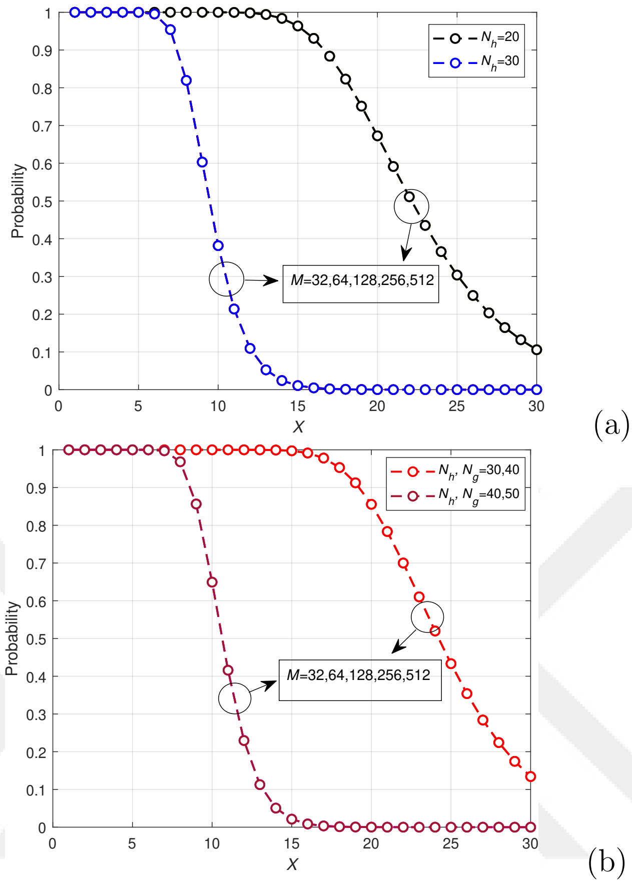

Figure 2.3: Probability of RIS-induced first tap being X times greater in squared magnitude than ISI term for varying M under (a) Scenario 1 where $\sigma_i = 10^{-3}$ and (b) Scenario 2 where $\sigma_i = 10^{-2}$.

It should be noted that for all computer simulations, we assume a uniform PDP, unless stated otherwise, which models a worst-case scenario, hence, for other PDPs the results would be superior. Additionally, for a smaller σ_i, the probability of negligible ISI approaches even closer to unity. We can conclude that even in the worst-case scenario, we can eliminate the ISI and maximize the squared magnitude of the first tap. For practical values of σ_i, we were not able to see an effect on changing the ISI paths or RIS elements because we would obtain perfect ISI elimination thanks to the RIS operation, hence for observational purposes we provided worst-case scenarios. These probabilities remain outstanding and ensure that the ISI is almost negligible, which will be further verified in terms of error performance analysis in the next chapter.

2.4.4 General Framework for ISI Elimination

In this subchapter, we assume there is a direct path from the Tx-Rx, hence, ISI elimination would need to be approached with caution and alternative perspectives. When there is a direct path from the Tx-Rx, the recieved discrete-time baseband signal may be expressed as:

$$y[n] = \sum_{d=1}^{D} h_d x[n - B\tilde{\zeta}_d] + \sum_{l_1=1}^{N_h} \sum_{l_2=1}^{N_g} \sum_{m=1}^{M} h_{l_1}^m g_{l_2}^m e^{j\theta_m} \times x[n - (B\tilde{\tau}_{l_1} + B\tilde{\xi}_{l_2})] + w[n], \tag{2.24}$$

where D is the number of direct paths from the Tx-Rx, h_d is the channel coefficient for the d^{th} direct path and $\tilde{\zeta}$ is the corresponding integer delay. In this case, there exists multiple PDPs. The received signals from the RIS may arrive at a different time than the direct signal paths to the Rx which can be a ameliorating or deteriorating factor depending on the scenario. Assuming the strongest and fastest tap, where the phases are arranged by the RIS coherently, are aligned and nonresolvable with the first tap, thus, ending up in the same delay bin. Therefore, the RIS may be exploited to reduce ISI that may be affecting the direct path by boosting the strongest signal of the direct path. However, this time alignment is not a guarantee in practical scenarios and the RIS may instead cause additional ISI to the direct signal if the PDP taps are resolvable with the direct path taps. In such a case, the RIS may try to minimize the ISI taps through a sort of complex optimization problem. Another alternative may be to activate a full absorption mode on the RIS and possibly reduce ISI by eliminating signals that may cause interference to the dominant direct signal. These will be our future research directions to combat multipath fading comprehensively.

2.5 Theoretical Error Probability Analysis

In this chapter, the system of Fig. 2.1 is revisited, where the transmission is carried out via an RIS under a blocked link between the Tx and Rx. For the sake of simplicity and to provide a clear insight, throughout the rest of this chapter we consider a single side frequency-selective scenario (Scenario 1). For this setup, $d_{\text{Tx-Rx}}$, $d_{\text{Tx-RIS}}$, $d_{\text{RIS-Rx}}$, represent the distances between the Tx and Rx, Tx and RIS, RIS and Rx, respectively. In addition, h_{Tx}, h_{RIS}, h_{Rx}, and f_c, represent the height of the Tx, RIS, Rx, and the operating frequency, respectively. The 3GPP UMi point-to-point NLOS path loss model for a single Tx/Rx path is also considered [3rd,]. Within the $2-6$ GHz frequency band and Tx-Rx distance ranging from $10-2000$ m, the 3GPP UMi path loss model for NLOS transmission is expressed as:

$$L(d)[\text{dB}] = 36.7\log_{10}(d) + 22.7 + 26\log_{10}(f_c). \tag{2.25}$$

The fading channel between the single antenna Tx and the m^{th} RIS element, and m^{th} RIS element to the single antenna Rx are denoted as $h_{l_1}^m$ and g^m, respectively. It is assumed that Rayleigh fading channels $h_{l_1}^m$ and g^m follow $\mathcal{CN}(0, \sigma_i^2)$ distribution where σ_i^2 is the variance of the complex Gaussian distribution. The RIS is composed of M passive and controllable reflecting elements. Revisiting chapter 2.3 with $N_g = 1$, the received signal can be written as

$$y[n] = \sum_{m=1}^{M} \alpha_1^m \beta_1^m e^{j\theta_m} x[n] + \sum_{l_1=2}^{N_h} \sum_{m=1}^{M} \alpha_{l_1}^m e^{j\theta_m} \times x[n-(B\tilde{\tau}_{l_1} - B\tilde{\tau}_1)] + w[n], \tag{2.26}$$

where $e^{j\theta_m}$ is the adjustable phase shift introduced by the m^{th} RIS element, $x[n]$ stands for the data symbol selected from Q-ary phase shift keying/quadrature amplitude modulation (PSK/QAM) constellations, and $w \sim \mathcal{CN}(0, W_0)$ is the AWGN term.

With the assumption of knowledge of the channel phases at the RIS [Wu et al., 2021b], it can be seen that by adjusting the θ_m term at the RIS, that is, $\theta_m = -\phi_m$ for $m = 1, \cdots, M$, the SINR can be maximized since the channel phases of the first tap is eliminated. Additionally, we assume that the ISI becomes negligible when the

Table 2.1: Fitted Gamma Distribution Parameters for Varying P_t and ISI Terms

# of Taps	P_t (dB):	5	10	15	20	25	30
$N_h = 1$	κ	51.6177	51.6967	51.7189	51.741	51.7497	51.8369
$N_h = 1$	ρ	0.00137096	0.00432819	0.0136773	0.0432479	0.136713	0.431585
$N_h = 2$	κ	51.6532	51.7883	51.8742	50.9644	41.8229	19.6424
$N_h = 2$	ρ	0.00136879	0.00430832	0.013516	0.0427256	0.156152	0.921367
$N_h = 5$	κ	51.7566	52.0687	52.3222	49.2235	31.7999	13.2366
$N_h = 5$	ρ	0.00136239	0.0042491	0.013054	0.0409241	0.166368	0.845089
$N_h = 9$	κ	51.8945	52.4418	52.9093	48.0063	28.909	14.2753
$N_h = 9$	ρ	0.00135392	0.0041721	0.0124799	0.0381424	0.145555	0.509455

first tap is 10 times greater in squared magnitude than the ISI paths. Substituting (2.14) into (2.13) the maximized SINR (γ_m) can be approximated as:

$$\gamma_m = \frac{E_s A^2}{E_s \sum_{l_1=2}^{N_h} |b_{l_1}|^2 + W_0}. \tag{2.27}$$

Since A^2 is a non-central chi-squared random variable with one degree of freedom and $B = \sum_{l_1=2}^{N_h} |b_{l_1}|^2$ is central chi-squared with $2(N_h - 1)$ degrees of freedom, their SINR ratio γ_m cannot be exactly derived and to the best of the authors' knowledge, its closed form has not been reported in the open literature. Thus, a semi-analytical approach is conducted where the distribution of γ_m is generated via MATLAB using dfittool by carefully considering A and B terms.

As we may recall, A^2 is a chi-squared distributed random variable which is a specific case of the gamma distribution. Since the effect of the ISI term B in γ_m is negligible, we expect γ_m to fit the gamma distribution. Fig. 2.4(a) shows the PDF of γ_m and its fit to the gamma distribution for varying number of ISI terms ($N_h - 1$)

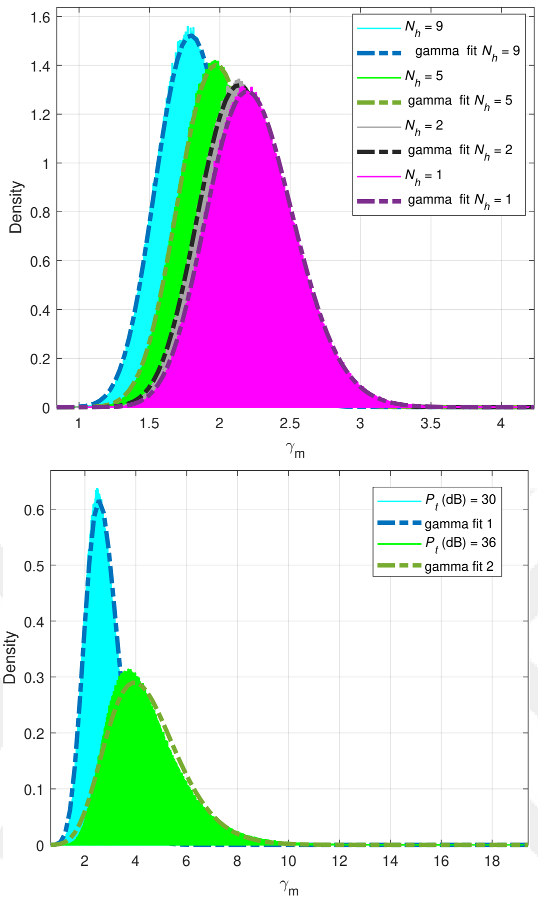

Figure 2.4: (a) Density distribution of γ_m for varying N_h and (b) gamma distribution fit for varying P_t.

with a fixed RIS size of $M = 128$ and $P_t = 20$ dB. Using the dfittool in MATLAB, it can be confirmed that the distribution of γ_m fits the gamma distribution. As the number of ISI terms are increased, the PDFs of the distributions begin to differ from one another and for a large number of N_h, as seen from the case of $N_h = 9$, the ISI terms start to show an effect and begin to slightly deviate from an exact fit to the gamma distribution. For different parameters such as M, N_h, P_t, W_0, the gamma distribution parameters vary and a general expression cannot be derived to express the gamma distribution parameters for given specifications. On the other hand, Fig. 2.4(b) shows the PDF for $M = 64$ for $P_t = 30$ dB and $P_t = 36$ dB. It can be seen that for $P_t = 30$ dB, the gamma distribution fits perfectly; however for a higher SINR where $P_t = 36$ dB, the gamma distribution does not fit perfectly. This is because as the SINR increases, the effect of the noise diminishes and the ISI terms in B starts to become more effective. Thus, the distribution is affected and deviated from the chi-squared distribution, which is a form of the gamma distribution.

To be used in theoretical derivations, for each configuration, the shape κ and scale ρ parameters for the gamma distribution need to be generated. Table I provides the gamma distribution parameters for $M = 128$ under $W_0 = -130$ dBm noise power required to calculate the moment generating function (MGF) for different scenarios. Specifically, the gamma distribution has the following MGF

$$M_{\gamma_m}(s) \approx (1 - \rho s)^{-\kappa}, \ \text{ for } \ s < \frac{1}{\rho}. \tag{2.28}$$

From (2.28), we can obtain the average SEP for Q-PSK signaling as in [Yildirim et al., 2020],

$$P_e \approx \frac{1}{\pi} \int_0^{(Q-1)\pi/Q} M_\gamma \left(\frac{-\sin^2(\pi/Q)}{\sin^2 \eta} \right) d\eta, \tag{2.29}$$

which for binary PSK (BPSK) simplifies to

$$P_e \approx \frac{1}{\pi} \int_0^{\pi/2} \left(1 + \frac{\rho}{\sin^2 \eta} \right)^{-\kappa} d\eta. \tag{2.30}$$

2.6 Simulation Results

In this chapter, computer simulation results for the proposed over-the-air equalization system (Scenario 1) with an RIS presented. First, the bit-error rate (BER) of the system is evaluated and compared to theoretical results for varying M and discussed in detail. Subsequently, the BER performance for discrete phases and ideal phases are assessed. Finally, a comparison of the proposed intelligent reflection and plain reflection, where the ISI terms remain, is presented for increasing RIS element size M.

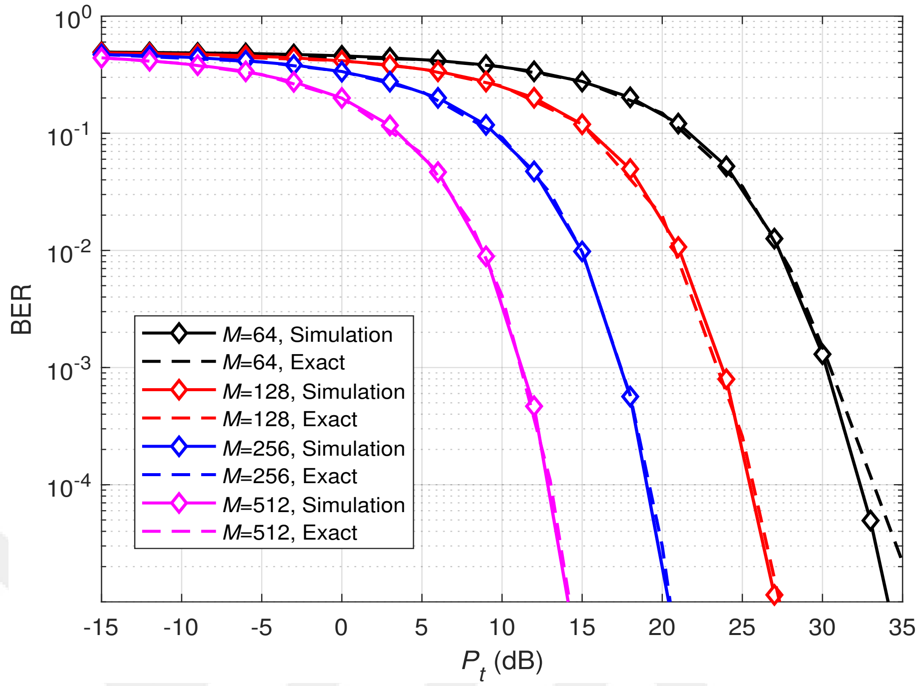

Figure 2.5: Comparison of exact and simulated results for varying number of RIS elements M.

For all computer simulations, path loss is included and the simulation parameters in Table 2.2 are used. For the BER analyses, the noise power is fixed to -130 dBm and the transmit power P_t is varied.

In Figs. 2.5 and 2.6, we present the BER results to verify the effectiveness of ISI elimination for $N_h = 2$ and varying M. It is clear that as the number of RIS elements M increases, the performance significantly increases and less P_t is needed to achieve the same error performance. However, there is a trade-off between cost and performance as M increases. Specifically, from Fig. 2.5, it can be confirmed that the ISI is negligible. At high BER values and M, computer simulation results exactly match the theoretical curves, which are the exact curves obtained from (2.30), and confirm the elimination of ISI. As seen from the the case of $M = 64$ at high P_t values, where the noise effect is negligible, the exact BER curves slightly differ than the simulated BER curves and this is because the negligible ISI terms beginning to present themselves which affects the distribution of γ_m as discussed in the previous

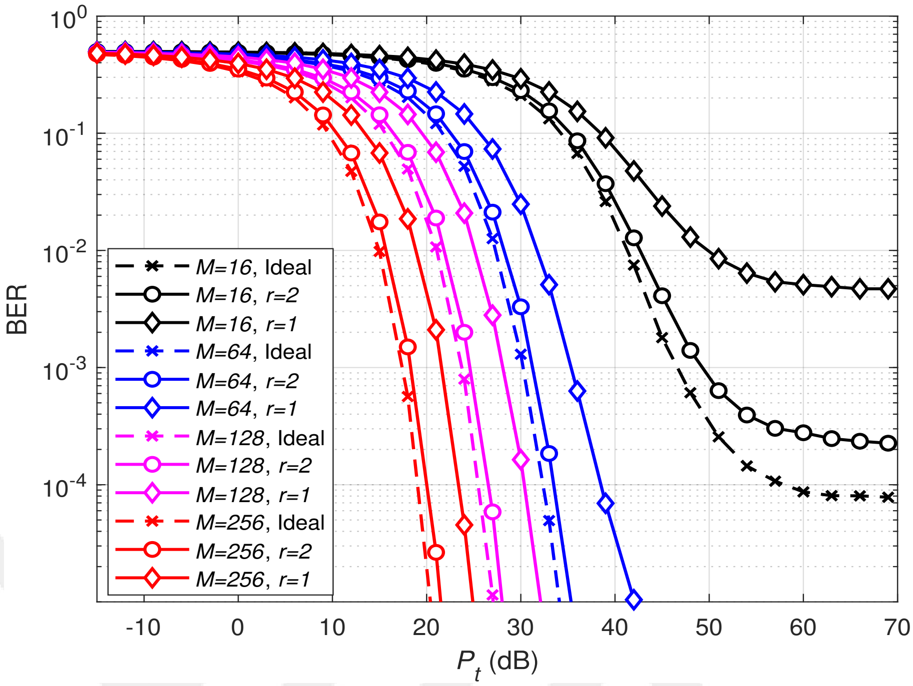

Figure 2.6: Performance of discrete phase compared to ideal phase for varying M.

chapter. However, for a greater M, even at low BER values, the ISI is nowhere to be seen because as M increases, the effect of the first tap becomes more significant. In other words, the ISI elimination probability is the same for all M as we recall from Fig. 2.3, however, as M increases in the BER results, the effect of the numerator in (2.27) becomes more dominant than the remaining ISI terms in the denominator thus, diminishing its effect even more.

Fig. 2.6 compares the BER performances for ideal and discrete phase adjustments, where r is the bit resolution of the discrete phase levels. For ideal phase adjustments, the phase term at the RIS is set exactly to eliminate the phase of the channel of the first tap. On the other hand, for discrete phase adjustments, the phase shifts at the RIS can only take certain values according to r and it rounded to the closest phase term to maximize the first tap. For example, when $r = 2$, there are $2^r = 4$ possible phases to choose from to maximize the first tap. Since discrete phases may not completely align the phase terms of the first tap, the full potential of the first tap maximization and ISI elimination cannot be achieved. However, if

Table 2.2: Computer Simulation Parameters

Parameter	Value
f_c [GHz]	5
$d_{\text{Tx-Rx}}$[m]	55.73
$d_{\text{Tx-RIS}}$[m]	35.51
$d_{\text{RIS-Rx}}$ [m]	20.22
h_{Tx} [m]	10
h_{RIS} [m]	4
h_{Rx} [m]	1
W_0 [dBm]	-130

the RIS is large enough, even 1 bit phases, $r = 1$, are enough to boost the desired signal terms. As it can be seen, the discrete case performs noticeably worse compared to the ideal case. For a large M, we do not observe an error floor, on the other hand, for a small number of RIS elements, such as $M = 16$, the RIS size is not sufficient to remove ISI and an irreducible error floor is observed. The parameter $M = 16$ is simply not sufficient number of RIS elements to provide the required performance similar to the case when using the central limit theorem, we would need a certain number of repetitions or samples for it to satisfy. As the resolution is decreased from 2 to 1, the error floor increases drastically. Fig. 2.7 compares the SINR of the proposed over-the-air equalization scheme with a blind reflection from the RIS with no ISI elimination for $N_h = 4$, $P_t = 30$ dB and varying M under uniform and exponential PDPs, respectively. By a plain and blind reflection, we consider a lossless reflection without any phase adjustment at the RIS elements, hence, not affecting the phases of the taps to eliminate the ISI. Fig. 2.7(a) presents the performance improvement considering uniform PDP for the worst-case scenario. On the other hand, Fig. 2.7(b) considers a more realistic exponential PDP. Comparing Figs. 2.7(a) and 2.7(b), it can be observed that the more realistic case, an exponential PDP, outperforms the worst-case uniform PDP scenario in terms of ISI

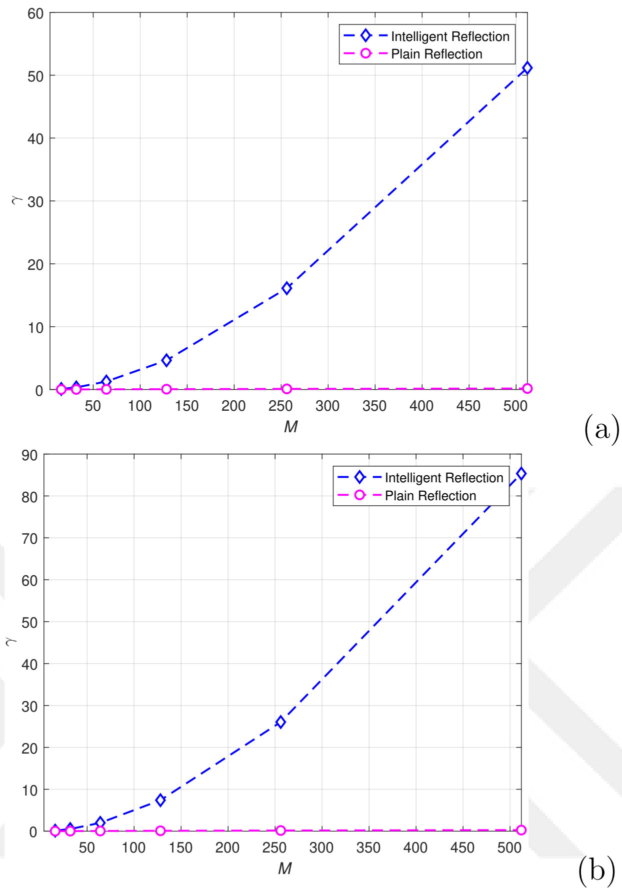

Figure 2.7: (a) SINR comparison of the intelligent reflection and non-intelligent reflection for varying M and (a) an uniform PDP (b) an exponential PDP.

minimization. This is because more power is allocated to the first tap in the exponential PDP case hence, exponentially reducing the power of the remaining ISI taps resulting in an increased SINR. It can also be concluded that the intelligent reflection significantly outperforms the plain reflection. This is because the ISI is made negligible for the intelligent reflection while in the plain reflection case, since equalization is not performed, ISI makes communication not possible which is seen by an almost zero SINR for any RIS size. When revisiting the BER curves and examining Fig. 2.7 together, they complement each other where as M increases, the SINR also exponentially increases thus, improving the BER.

2.7 Conclusion

The main motivation of this study has been to provide a unique framework and perspective to RIS-based systems and virtual equalization for frequency-selective channels. It has been shown that an efficient over-the-air equalization concept, independent from the Tx and Rx, can be realized by utilizing the RIS. The RIS adjusts the phases of its elements according to the incoming signals to maximize the magnitude of the first tap, making the ISI terms negligible, hence, maximizing the SINR performance. A complete end-to-end system model and a probabilistic analysis of ISI elimination have been provided. In addition, a theoretical error probability analysis in conjunction with computer simulation results have shown the advantages of the proposed scheme. Future works may include an extension of this model to different scenarios, such as when a direct link exists between the Tx and Rx. Also, in the future this model may be analyzed under different channel fading distributions, multiple RISs and for mobile nodes.

Chapter 3

RECONFIGURABLE INTELLIGENT SURFACE ENABLED OVER-THE-AIR UPLINK NOMA

3.1 Preface

Innovative RIS technologies are rising and recognized as promising candidates to enhance 6G and beyond wireless communication systems. RISs acquire the ability to manipulate electromagnetic signals, thus, offering a degree of control over the wireless channel and the potential for many more benefits. Furthermore, active RIS designs have recently been introduced to combat the critical double fading problem and other impairments passive RIS designs may possess. In this chapter, the potential and flexibility of active RIS technology are exploited for uplink systems to achieve virtual non-orthogonal multiple access (NOMA) through power disparity over-the-air rather than controlling transmit powers at the user side. Specifically, users with identical transmit power, path loss, and distance can communicate with a base station sharing time and frequency resources in a NOMA fashion with the aid of the proposed hybrid RIS system. Here, the RIS is partitioned into active and passive parts and the distinctive partitions serve different users aligning their phases accordingly while introducing a power difference to the users' signals to enable NOMA. First, the end-to-end system model is presented considering two users. Furthermore, outage probability calculations and theoretical error probability analysis are discussed and reinforced with computer simulation results.

3.2 Introduction

Wireless communication systems are evolving rapidly in all communication layers, especially in the physical and MAC layers, to meet stringent 6G requirements.

Specifically, in the physical layer, promising approaches and advancements have been investigated to enhance wireless communication quality and performance [Chowdhury et al., 2020, Rappaport et al., 2019, Sahin et al., 2021, Huang et al., 2020b]. In general, the environment and channels in these wireless communication systems have been considered uncontrollable, which may lead to performance degradation by negatively affecting the communication efficiency, quality-of-service (QoS), and more [Basar et al., 2019, Zhang et al., 2021b].

Recent advancements in meta materials have led to reconfigurable intelligent surfaces (RISs) to control the wireless channel passively and, thus, enhance communication performance [Basar, 2019, Huang et al., 2020b, Kilinc et al., 2021b]. This popular technology has greatly attracted the attention of both academia and industry. A RIS is a large array with many cost-effective elements that can reflect, adjust, absorb and even amplify impinging signals with an adjustable reflecting coefficient [Di Renzo et al., 2020]. By doing so, RISs may artificially enhance existing wireless communication by suppressing interference [Arslan et al., 2021, Zhang et al., 2021a, ElMossallamy et al., 2021], increasing capacity [Su et al., 2020a, Perović et al., 2020], extending coverage [Zeng et al., 2021b, Tapio et al., 2021a, Wu et al., 2021a], and providing energy efficiency [Tasci et al., 2022b, Huang et al., 2019c, Hua et al., 2021a], all without the need for additional RF chains. RISs may also be used in applications such as localization, Wi-Fi, etc. Hence, RIS technology is a promising tool to exploit in wireless communication systems. However, RISs do come with problems of their own. RISs typically work best in scenarios where direct links do not exist or are substantially weak [Zhang et al., 2021b, Aygül et al., 2021, Yang et al., 2020c]. Furthermore, a major challenge in RIS technology is the multiplicative path loss of the transmitter-RIS-receiver link, making significant gains very difficult for passive RIS designs [Zhang et al., 2021b, Wu et al., 2021c, Zhi et al., 2022, Tasci et al., 2022b].

3.2.1 Related Work

To combat the critical problem of multiplicative path loss, sacrificing from the fully passive structure, the active RIS concept has been introduced [Zhang et al., 2021b, Zhi et al., 2022]. In hopes of overcoming the high path loss problem, active RISs not only reflect the signals at the RIS but also amplify and strengthen the power of the impinging signals at the expense of additional power consumption and additional thermal noise introduced through the active elements [Zhi et al., 2022]. Active RIS technology brings additional flexibility to RIS, which is possible to achieve more than just mitigating the multiplicative path loss. By combining passive and active RIS technologies, hybrid systems may be constructed to enhance communication system performances and novel solutions [Wu et al., 2021c, Basar and Poor, 2021]. Albeit its numerous benefits, active RIS designs also have drawbacks such as increased hardware complexity, increased power consumption and costs [Tasci et al., 2022b]. Hence, hybrid designs considering passive and active architectures are more promising.

Passive and active RIS technologies have also been exploited and analyzed in NOMA schemes. A simple design is proposed in [Ding and Poor, 2020] by employing multiple passive RISs and effectively aligning the direction of users' channel vectors to aid in NOMA. The sum rate is maximized in downlink MISO RIS-NOMA systems through joint beamforming designs at the BS and RIS. The downlink transmit power is minimized for RIS NOMA through joint optimization at the BS transmit beamformers and RIS phases. Moreover, the impact of coherent and random phase shift designs at the RIS are evaluated [Mu et al., 2019, Fu et al., 2019, Ding et al., 2020]. In addition, a power domain downlink NOMA scheme is proposed by exploiting an RIS to improve the reliability of the two-user system, and its bit-error rate is evaluated in [Thirumavalavan and Jayaraman, 2020]. Furthermore, the impact of hardware impairments in terms of performance metrics is studied, and outage probability and throughput performances are derived in [Hemanth et al., 2020]. On the other hand, studies on uplink-NOMA exploiting RISs have also been conducted to enhance coverage, derive the outage probabilities and ergodic rates, and grant-free ultra-reliable uplink sensor data transmission exploiting diversity to obtain reliability [Cheng et al., 2021, Melgarejo et al., 2020]. Passive RIS-aided NOMA systems are prevalent in the literature; however, active and hybrid RIS-aided NOMA systems have yet to be explored, especially for uplink scenarios. As it can be concluded, RIS is a superior technology to aid NOMA wireless communication systems and is attracting the attention of researchers. However, the RIS-aided NOMA literature has yet to mature. Moreover, to the best of the authors' knowledge, an active or a hybrid RIS has not been the primary enabler of NOMA, especially in the uplink. In addition, RIS-assisted uplink-NOMA has not been considered in the literature.

3.2.2 Main Contributions

In this study, a hybrid RIS is partitioned into two parts as active and passive parts. Benefiting from both active and passive RIS technologies, a novel system is proposed to enable uplink-NOMA over-the-air to the users, where the QoS of both users is enhanced by using a hybrid design rather than a fully active design. In conventional uplink-NOMA, the users require a power allocation scheme to share the same time and frequency resources [Cheng et al., 2021, Wang et al., 2022, Li et al., 2022]. On the contrary, in the proposed method, the users may transmit with the same power and not worry about interference with the confidence of the RIS, providing them their required QoS. The active part of the RIS is coherently aligned for one user and amplifies its signal; on the other hand, the passive part is coherently aligned for the other user with no amplification in an entirely passive manner. The first user's signal is coherently aligned and boosted by the active part of the RIS to enable a certain power disparity from the other user, enabling NOMA and SIC at the BS. The passive part of the RIS requires no amplification since the active part already obtains a power difference. However, it is aligned for the second user to improve its signal-to-interference and noise ratio (SINR) as in conventional passive RIS methods.

The major contributions of this study are listed as follows:

- A novel communication system is proposed to virtually enable uplink-NOMA over the air with a single hybrid RIS.

- A thorough end-to-end system model of the proposed scheme is provided and analyzed along with computer simulations.
- The outage probability is derived and calculated for different configurations and confirmed with simulations.
- A theoretical error probability analysis is provided along with computer simulation results for varying parameters and scenarios considering different successive interference cancellation (SIC) performances.
- Two scenarios for a fixed active RIS gain case and an optimized RIS gain case are presented. The performances of both cases are compared and discussed.
- Bit-error rate (BER) computer simulations have been performed with perfect and imperfect channel state information (CSI) conditions.
- Achievable rate and energy efficiency (EE) comparisons have been presented for the proposed hybrid NOMA scheme against conventional fully active and fully passive RIS orthogonal multiple access (OMA) scenarios existing in the literature.

3.2.3 Chapter Organizations

The rest of the chapter is organized as follows, chapter 3.3 presents the end-to-end system model of the proposed scheme. chapter 3.4 presents a theoretical analysis of the outage probability for different scenarios. chapter 3.5 discusses the RIS power consumption and amplification factor. Furthermore, computer simulation results including outage probability, QoS, effect of interference cancellation errors, achievable rate, energy efficiency and bit-error rate are provided and discussed in chapter 3.6. Finally, the chapter is concluded with the final remarks in chapter 3.7.

3.3 End-To-End System Model

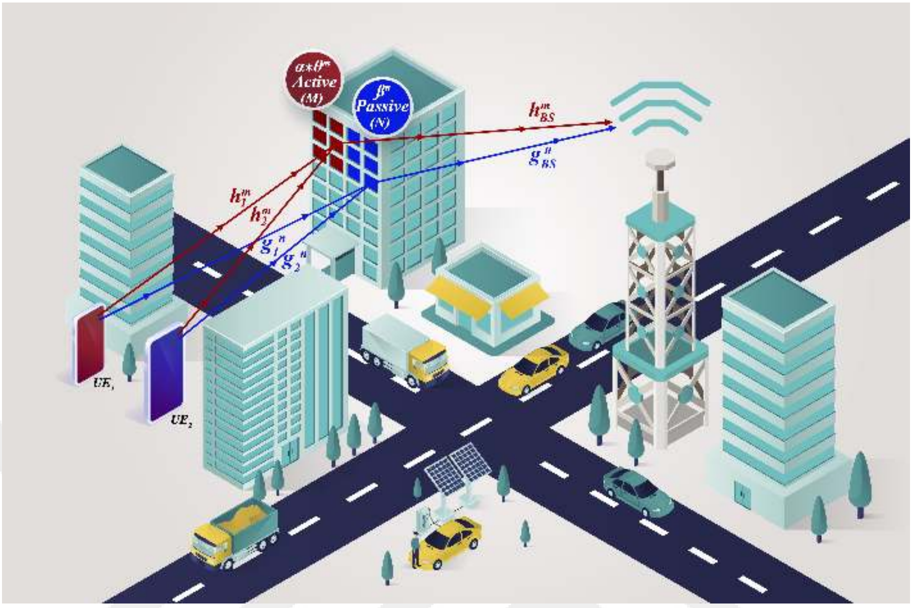

Figure 3.1: Proposed over-the-air uplink-NOMA system model for $K = 2$ users.

This chapter presents the system model for the proposed over-the-air uplink-NOMA scheme. In the proposed system, we consider a two-user $(U_k, k \in 1, \cdots, K)$ network where $K = 2$, uplink scenario operating under frequency-flat Rayleigh fading channels in the presence of an RIS. Both users are served through the same frequency and time slots with single-carrier signals. In conventional uplink-NOMA systems, the users' transmit power needs to be optimized to enable NOMA, and different transmit powers are generally assigned to near and far users. In the proposed system, the users transmit with the same power P_t without worrying about the power difference as the power reception difference required by SIC receiver is satisfied by a hybrid RIS that is partitioned into two parts, i.e., active and passive as shown in Fig. 3.1. Practically, The CSI of users and RIS can be obtained by applying different channel acquisition methods such as those proposed in [Hu et al., 2021, Abdallah et al., 2022]. Hence, considering available CSI, the BS can optimize RIS phase shifts and send them back to the RIS controller via a dedicated wired [Tan et al., 2016] or wireless channel [Wu and Zhang, 2019]. Assuming the CSI is available at the BS and RIS, the active part of the RIS with M elements has amplifiers in every element and is coherently aligned for one user, either user 1 (U_1) or user 2 (U_2), while the other passive part with N elements is coherently aligned for the other user. In other words, $\boldsymbol{\theta} \triangleq [e^{j\phi_1}, \cdots, e^{j\phi_M}]^{\mathrm{T}} \in \mathbb{C}^{M\times 1}$ and $\boldsymbol{\beta} \triangleq [e^{j\xi_1}, \cdots, e^{j\xi_N}]^{\mathrm{T}} \in \mathbb{C}^{N\times 1}$ are the phase alignment vectors at the active and passive parts of the RIS, respectively, where $[\cdot]^{\mathrm{T}}$ represents transposition operator.

The received signal at the base station can be written as

$$\begin{aligned} y =& \sqrt{P_t}\sum_{k=1}^{K}\left(\sqrt{\alpha}\sum_{m=1}^{M} h_k^m \theta^m h_{BS}^m x_k + \sum_{n=1}^{N} g_k^n \beta^n g_{BS}^n x_k\right) \\ &+ \sqrt{\alpha}\sum_{m=1}^{M} z^m \theta^m h_{BS}^m + w_0, \end{aligned} \tag{3.1}$$

where x_k, α, θ^m, and β^n, are the modulated PSK/QAM symbol transmitted by the k^{th} user, amplification factor at the active part of the RIS, m^{th} element of $\boldsymbol{\theta}$, $m = 1, \cdots, M$, and the n^{th} element of $\boldsymbol{\beta}$, $n = 1, \cdots, N$, respectively. Additionally, z^m and w_0 stand for the noise term from the amplifier at the m^{th} RIS element and additive white Gaussian noise (AWGN) sample which follows the distributions $\mathcal{CN}(0, \sigma_z^2)$ and $\mathcal{CN}(0, W_0)$, respectively. Furthermore, h_k^m, g_k^n, h_{BS}^m, and g_{BS}^n respectively, stand for the independent and identically distributed (i.i.d) Rayleigh fading channel coefficients of the k^{th} user to the m^{th} element of the active part of the RIS, k^{th} user to the n^{th} element of the passive part of the RIS, the m^{th} element of the active part of the RIS to the BS, and the n^{th} element of the passive part of the RIS to the BS.

The channel coefficients follow the distribution of $\mathcal{CN}(0, \sigma^2)$, where $\sigma^2 = \frac{1}{L}$ and L is the large scale path loss factor. For the first user (U_1), at the active part of the RIS, the m^{th} element is coherently aligned as follows: $\theta^m = e^{j\phi^m} = e^{-j\angle(h_1^m h_{BS}^m)}$. On the other hand, for the second user (U_2), at the passive part of the RIS, the n^{th} element is coherently aligned as follows: $\beta^n = e^{j\xi^n} = e^{-j\angle(g_2^n g_{BS}^n)}$. Equivalently, the received signal in (3.1) may be rewritten as

$$y = \sqrt{P_t}\sum_{k=1}^{K}\left(\sqrt{\alpha}\mathbf{h}_k^{\mathrm{T}}\bar{\boldsymbol{\theta}}\mathbf{h}_{BS} + \mathbf{g}_k^{\mathrm{T}}\bar{\boldsymbol{\beta}}\mathbf{g}_{BS}\right)x_k + \sqrt{\alpha}\mathbf{z}\bar{\boldsymbol{\theta}}\mathbf{h}_{BS} + w_0, \tag{3.2}$$

$$\gamma_1 = \frac{P_t(|\sqrt{\alpha}\sum_{m=1}^{M}|h_1^m||h_{BS}^m| + \sum_{n=1}^{N} g_1^n\beta^n g_{BS}^n|^2)}{P_t(|\sqrt{\alpha}\sum_{m=1}^{M} h_2^m\theta^m h_{BS}^m + \sum_{n=1}^{N}|g_2^n||g_{BS}^n||^2) + \sigma_z^2\alpha\sum_{m=1}^{M}|\theta^m h_{BS}^m|^2 + W_0}$$
$$\gamma_2 = \frac{P_t(|\sqrt{\alpha}\sum_{m=1}^{M} h_2^m\theta^m h_{BS}^m + \sum_{n=1}^{N}|g_2^n||g_{BS}^n||^2)}{\sigma_z^2\alpha\sum_{m=1}^{M}|\theta^m h_{BS}^m|^2 + W_0} \tag{3.3}$$

where $\mathbf{h}_k = [h_k^1, \cdots, h_k^M]^{\mathrm{T}}$, $\mathbf{g}_k = [g_k^1, \cdots, g_k^N]^{\mathrm{T}}$, $\mathbf{h}_{BS} = [h_{BS}^1, \cdots, h_{BS}^M]^{\mathrm{T}}$, and $\mathbf{g}_{BS} = [g_{BS}^1, \cdots, g_{BS}^N]^{\mathrm{T}}$ are the channel coefficient vectors between the k^{th} user and the active and passive parts of the RIS, and between the RIS and BS for the active and passive parts, respectively. Furthermore, $\mathbf{z} = [z^1, \cdots, z^M]^{\mathrm{T}}$ is the noise term vector from the active elements of the RIS. Additionally, $\bar{\boldsymbol{\theta}} = \mathrm{diag}(\boldsymbol{\theta})$ and $\bar{\boldsymbol{\beta}} = \mathrm{diag}(\boldsymbol{\beta})$, where $\mathrm{diag}(\cdot)$ is the diagonalization operator. Hence, the SINR of U_1 and U_2 may be expressed as in (3.3), shown at the following page.

As in classical NOMA, U_1 directly decodes its signal while U_2 requires SIC to decode U_1 and subtract its own signal from the received signal. It can be seen from Fig. 3.1 as well as from the SINR equations, the signals of the users imping on all of the partitions of the RIS, thus, causing interference. However, as we will later discuss, this does not affect the NOMA communication due to the coherent aligning and amplification of the user making it much greater than the user supported by the passive side which is only coherently aligned and not amplified.

3.4 Theoretical Outage Probability Analysis

In this chapter, the outage probability calculations are considered. For the sake of simplicity, the SINRs of the users impinging on the active and passive parts of the RIS are respectively re-expressed as

$$\gamma_1 = \frac{P_t|A+B|^2}{P_t|C+D|^2 + \sigma_z^2\alpha\sum_{m=1}^{M}|E|^2 + F}, \tag{3.4}$$

$$\gamma_2 = \frac{P_t|C+D|^2}{\sigma_z^2\alpha\sum_{m=1}^{M}|E|^2 + F}. \tag{3.5}$$

where $A = \sqrt{\alpha}\sum_{m=1}^{M} |h_1^m||h_{BS}^m|$, $B = \sum_{n=1}^{N} g_1^n \beta^n g_{BS}^n$, $C = \sqrt{\alpha}\sum_{m=1}^{M} h_2^m \theta^m h_{BS}^m$, $D = \sum_{n=1}^{N} |g_2^n||g_{BS}^n|$, $E = \theta^m h_{BS}^m$, and $F = W_0$. Since A, B, C, and D terms include summation over RIS elements and since the RIS elements are sufficiently large, due to the Central Limit theorem (CLT), the channel multiplications in A, B, C and D lead to Gaussian distribution regardless of their distributions. Due to the CLT, all channel multiplications lead to the Gaussian distribution, regardless of what the distribution of all parts A, B, C, D are. These distributions are summarized in Table I. Furthermore, the derivations of the means and variances of A, B, C, and D are derived in the following lemmas.

Lemma 1. *The mean and variance of A are obtained as $\mu_A = \frac{\sqrt{\alpha} M \pi \sigma_{h_1} \sigma_{h_{BS}}}{4}$ and $\sigma_A = \alpha M \sigma_{h_1}^2 \sigma_{h_{BS}}^2 (1 - \frac{\pi^2}{16})$, respectively.*

Proof. We refer interested readers to Appendix A for the derivation steps. □

Lemma 2. *The mean and variance of B are obtained as $\mu_B = 0$ and $\sigma_B = N\sigma_{g_1}^2 \sigma_{g_{BS}}^2$, respectively.*

Proof. We refer interested readers to Appendix B for the derivation steps. □

Lemma 3. *The mean and variance of C, D, E, and F are calculated as $\mu_C = 0$, $\sigma_C = \alpha M \sigma_{h_2}^2 \sigma_{h_{BS}}^2$, $\mu_D = \dfrac{N\pi\sigma_{g_2}\sigma_{g_{BS}}}{4}$, $\sigma_D = N\sigma_{g_2}^2 \sigma_{g_{BS}}^2 \left(1 - \dfrac{\pi^2}{16}\right)$, $\mu_E = 0$, $\sigma_E = \sigma_{BS}^2$, $\mu_F = 0$, $\sigma_F = W_0$, respectively.*

Proof. We refer interested readers to Appendix C for the derivation steps. □

The outcomes of these three lemmas are summarized as in Table 3.1.

In SINR expressions, the squared sum of Gaussian random variables exists, which leads to the chi-squared distribution, which is a form of the Gamma distribution. Hence, the SINR is the ratio of chi-squared random variables, where $|A + B|^2$ and $|C + D|^2$ are non-central chi-squared random variables with two degrees of freedom and $\sigma_z^2 \alpha \sum_{m=1}^{M} |E|^2$ is a central chi-squared random variable with $2M$ degrees of freedom. As seen in Fig. 3.2, the SINRs of both users fit the Gamma distribution.

Table 3.1: Random Variable (RV) Distributions For (3)

RV	μ	σ^2	Type of RV
A	$\frac{\sqrt{\alpha}M\pi\sigma_{h_1}\sigma_{h_{BS}}}{4}$	$\alpha M\sigma_{h_1}^2\sigma_{h_{BS}}^2(1-\frac{\pi^2}{16})$	Real Gaussian
B	0	$N\sigma_{g_1}^2\sigma_{g_{BS}}^2$	Complex Gaussian
C	0	$\alpha M\sigma_{h_2}^2\sigma_{h_{BS}}^2$	Complex Gaussian
D	$\frac{N\pi\sigma_{g_2}\sigma_{g_{BS}}}{4}$	$N\sigma_{g_2}^2\sigma_{g_{BS}}^2\left(1-\frac{\pi^2}{16}\right)$	Real Gaussian
E	0	σ_{BS}^2	Complex Gaussian
F	0	W_0	Complex Gaussian

To obtain the outage probability (OP) of both users, we may use $OP_k = P(\gamma_k < 2^{r_k} - 1)$, where r_k is the minimum rate at which the QoS holds for U_k. Since equivalent steps will be used for both users, for illustrative purposes, let us focus on U_1 supported by the active part of the RIS. The random variables in the SINR are left on one side, and the CDF of the equation is solved as

$$\begin{aligned} OP_k &= P\left(\frac{P_t|A+B|^2}{P_t|C+D|^2 + \sigma_z^2\alpha\sum_{m=1}^{M}|E|^2 + F} < v\right) \\ &= P(P_t|A+B|^2 - P_t|C+D|^2 v - \sigma_z^2\alpha\sum_{m=1}^{M}|E|^2 v < Fv). \end{aligned} \tag{3.6}$$

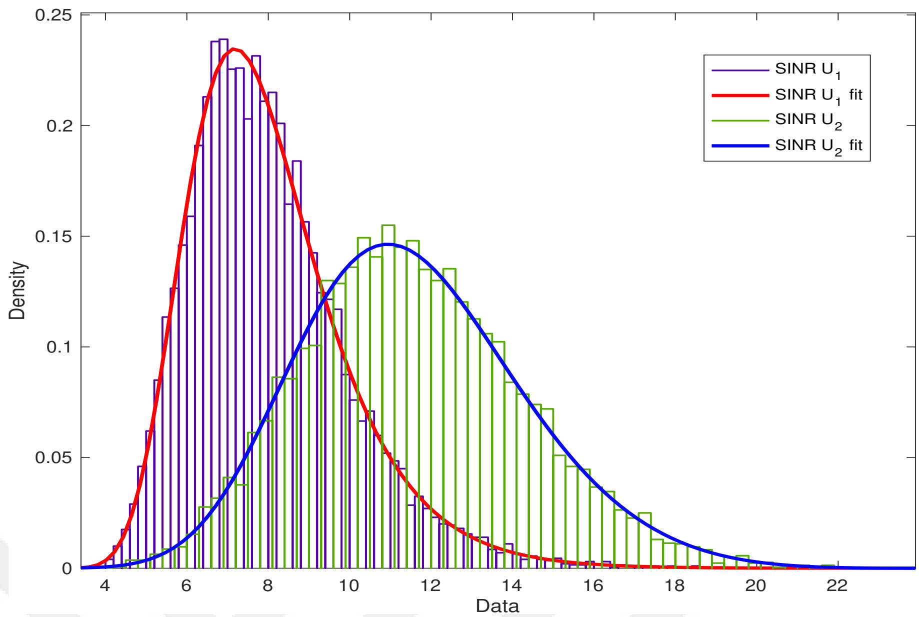

Figure 3.2: Fitted distribution of user SINRs.

The term above may be simply expressed as the CDF of G, $P(G < g) = F_G(g)$, where $G = P_t|A + B|^2 - P_t|C + D|^2 v - \sigma_z^2 \alpha \sum_{m=1}^{M} |E|^2 v$ is a difference of multiple chi-square random variables, hence, complicating mathematical calculations. However, the characteristic functions (CFs) come in handy when evaluating chi-squared random variables. The CF of a chi-squared random variable is given as [Simon, 2002]

$$\Psi_X(\omega) = \frac{1}{(1 - 2j\omega\sigma^2)^{n/2}} \exp\left(\frac{j\omega\mu^2}{1 - 2j\omega\sigma^2}\right), \tag{3.7}$$

where $X = \sum_{k=1}^{n} X_k^2$ and $X_k \sim \mathcal{N}(\mu_k, \sigma^2)$. Hence, the CF of E can be calculated.

Lemma 4. *Although the random variables $\{A, C\}$ and $\{B, D\}$ share the common terms h_{BS}^m and g_{BS}^n, respectively, they are uncorrelated due to their zero correlation coefficient.*

Proof. We refer interested readers to Appendix D for the derivation steps. □

To conduct our theoretical analysis and obtain the characteristic functions, since the random variables are uncorrelated, we may express $|A + B|^2$ and $|C + D|^2$ in terms of their real and imaginary parts as $[\Re(A)+\Re(B)]^2+[\Im(B)]^2$ and $[\Re(C)+\Re(D)]^2+[\Im(C)]^2$, respectively. This is a sum of independent non-central chi-squared and central chi-squared random variables, and since we know the statistics of the random variables, the CFs may be calculated from [Simon, 2002] using

$$\Psi_X(\omega)=\frac{1}{((1-2j\omega\sigma_1^2)(1-2j\omega\sigma_2^2)^{n/2})}\exp\left(\frac{j\omega\mu_1^2}{1-2j\omega\sigma_1^2}\right), \tag{3.8}$$

where μ_1, σ_1, and σ_2 will be substituted with the means and variances of the summation terms. Considering the sum of independent RVs as in (3.6), is the multiplication of their individual CF's [Basar, 2020a], we obtain

$$\Psi_G(w)=\Psi_{P_t|A+B|^2}(w)\Psi_{(-P_t|C+D|^2v)}(w)\Psi_{(-\sigma_z^2\alpha\sum_{m=1}^{M}|E|^2v)}(w). \tag{3.9}$$

Then, we may approach using Gil-Pelaez's inversion formula [Mathai and Provost, 1992b] since it is possible to obtain the cumulative distribution function (CDF) of this difference of chi-squared random variables as

$$F_G(g)=\frac{1}{2}-\int_0^\infty\frac{\Im\{e^{-jwg}\Psi_G(w)\}}{w\pi}dw, \tag{3.10}$$

where $\Im$ denotes the imaginary part, $F_G(g)$ is the CDF of G and $\Psi_G(w)$ is the CF of G. With this CDF expression of the difference of chi-squares, it is possible to obtain the outage probability as mentioned previously.

3.5 RIS Power Consumption and Amplification Factor

The fully connected active RIS architecture includes a power amplifier (PA) in each RIS element, and the power consumption of the active part of the RIS is dependent on the power consumed by the PAs. The power consumption of a single active RIS element is a linear function of the output signal power of the PA and modeled as

$$P_a=\frac{1}{\nu}P_o, \tag{3.11}$$

where ν and P_o denote the efficiency and output power of the power amplifier, respectively. The total transmit power available to the active part of the hybrid

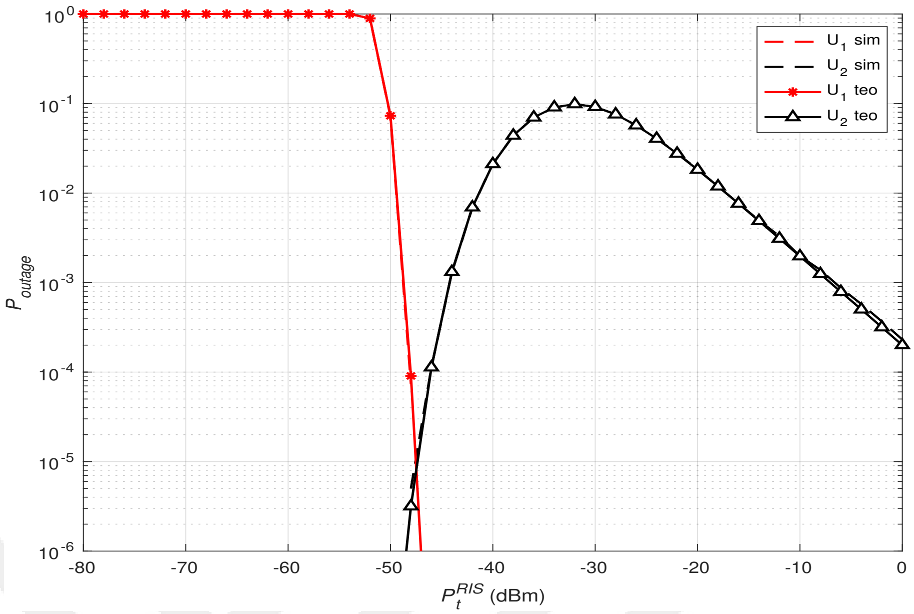

Figure 3.3: P_t^{RIS} vs outage probability to find optimal α for given default parameters.

RIS architecture is denoted by P_t^{RIS} and varied according to system requirements to sustain power domain NOMA. The output power of a single active RIS element is therefore obtained as $P_o = P_t^{RIS}/N$. To obtain the maximum output power from a single active RIS element, we need to maximize the gain of the amplifier by considering P_o constraint. Considering an ideal PA with $\nu = 1$, the gain of the amplifier is obtained as follows

$$G = \min\left(\sqrt{\frac{P_o}{P_t \mathrm{E}[\|\mathbf{h}_k\|^2]}}, G_{max}\right) \tag{3.12}$$

where G_{max} is the maximum gain of the amplifier and sets an upperbound on G. The denominator of the equation represents the average signal power at the input of the amplifier. Since we consider the uniform gain distribution for all active RIS elements, the average channel gain between the assisted user and active RIS elements is considered.

As seen in Eq. (3.12), the amplifier gain G, also referred to as α, depends on many variables and needs to be determined very carefully. The optimum gain should be obtained in order to best serve both users. Fig. 3.3 shows the effect of available power on the active RIS side for both users. It can been observed that for the parameters given in Fig. 3.3 which we consider as default parameters, the NOMA scheme can efficiently operate when -47 dBm amplifier power, which corresponds to $\alpha = 8.5$ for each RIS element, is allocated for the active part. This result shows that the required power on the active RIS side is much less than the transmission power of the users and NOMA can be provided with a very small amount of power allocation and coherent alignment of the users.

Additionally, considering α is the same for all elements, the gain α can also be expressed in terms of the system parameters as $\alpha = \frac{P_t^{RIS}/M}{P_t C_h}$, where C_h is the average channel power of the users. It is important to note that for practicality, α is limited to a minimum of 0 dB and a maximum of 30 dB [Tasci et al., 2022b]. However, for the sake of better visualization explanations, Fig. 3.3 is not limited by the practical range of α. The results mentioned in the remaining subchapters obey the aforementioned practical amplifier gain ranges. We optimize P_t^{RIS} and then we extract the optimal α based on that optimum P_t^{RIS} using the formulas above. α is selected in the fairest manner to serve both users. For the fixed α case, we look for the minimum difference of their outage performance which would be where they intersect as in Fig. 3.3. However, for the fixed alpha case, the optimal alpha is best only for that specific set of parameters and as any parameter changes, it loses its optimality.

3.5.1 Problem Formulation

In this case, we need to minimize P_t^{RIS} while maximizing the outage probability performance which can be define by the optimization problem P1:

$$\text{P1} = \min_{P_t^{RIS}, \Delta} \quad \Delta \quad \text{s.t.} \quad P_{out}^k \leq \Delta, \quad k \in \{1, 2\}. \tag{3.13}$$

Here, Δ is the auxiliary variable representing the outage probability threshold constraint for a fair P_t^{RIS} selection that serves both users. In P1, the aim is to obtain the best outage performance by using the minimum available power. To achieve this, we need to minimize both P_t^{RIS} and Δ. Since we aim at the fairness while obtaining the best performance with a minimum power consumption, we equivalently target the minimum difference in outage performance which provides the same result/concept. This can be formulated the and solved as the equivalent standard problem where P1 is transformed into P2:

$$\text{P2} = \min_{P_t^{RIS}} \quad \|P_{out}^1 - P_{out}^2\|. \tag{3.14}$$

Furthermore, we can solve P2 with a standard line search methods such as the Golden Selection algorithm and Simulated Annealing. In our simulations, we use the Golden Selection line search method to solve P2. However, different methods of α optimization may also be possible. It should be noted that we ensure maximum fairness and all of the users have a weight no less than Δ.

3.6 Simulation Results

In this subchapter, the system of Fig. 3.1 is revisited, where the transmission is carried out via an RIS under a blocked link between the users and the BS. For this setup, $d_{U_1\text{-BS}}$, $d_{U_2\text{-BS}}$, $d_{U_1\text{-RIS}}$, $d_{U_2\text{-RIS}}$, $d_{\text{RIS-BS}}$, represent the distances between the users and BS, users and RIS, RIS and BS, respectively. In addition, h_{U_1}, h_{U_2}, h_{RIS}, h_{BS}, and f_c, represent the height of the users, RIS, BS, and the operating frequency, respectively. The 3GPP UMi point-to-point NLOS path loss model for a single Tx/Rx path is also considered [3rd,]. Within the $2-6$ GHz frequency band and Tx-Rx distance ranging from $10-2000$ m, the 3GPP UMi path loss model for NLOS transmission is expressed as:

$$L(d)[\text{dB}] = 36.7\log_{10}(d) + 22.7 + 26\log_{10}(f_c). \tag{3.15}$$

The RIS is composed of M active and N passive and controllable reflecting elements.

For all computer simulations, path loss is included and the default parameters in Table II as well as the setup in Table III are used as the fixed parameters for simulations and analyses unless stated otherwise. These parameters are justified

Table 3.2: Default Parameters

Parameter	Value
P_t^{RIS} [dBm]	-47
α (linear)	8.5
$M = N$	512
P_t [dBm]	15
R^{th} [bps/Hz]	2
ϵ	0 (perfect SIC)
W_0 [dBm]	-130
n_{amp} [dBm]	-130

through practical scenarios in the Literature [3rd, , Tasci et al., 2022b, Basar et al., 2019, Arslan et al., 2021]. Fixed $\alpha = 8.5$ is considered through out the study, as it is the optimal case for the default parameters as seen from Fig. 3.3, unless it is specifically stated that the optimized case of α is use.

Typically in an RIS-aided communication system, the performance increases with the size of RIS. This behaviour can also be seen in Fig. 3.4, which includes the outage probability performance simulation and theoretical simulation for both users with respect to varying RIS size. It can be observed that for a fixed α, a minimum RIS size of 300 is needed to enable communication at both users, however, a larger RIS is preferred for a enhanced performance at the cost of additional hardware expenditure. When α is optimized, it can be seen that the performance for both users are enhanced and a smaller RIS size is sufficient to provide the same performance compared to the fixed α case. U_1 has perfect communication while U_2 is at outage until an RIS size of

Table 3.3: Computer Simulation Set-Up Parameters

Parameter	Value
f_c [GHz]	5
$d_{U_1\text{-BS}}$[m]	55.73
$d_{U_2\text{-BS}}$[m]	55.73
$d_{U_1\text{-RIS}}$[m]	35.51
$d_{U_2\text{-RIS}}$[m]	35.51
$d_{\text{RIS-BS}}$ [m]	20.22
h_{U_1} [m]	10
h_{U_2} [m]	10
h_{RIS} [m]	4
h_{BS} [m]	1
W_0 [dBm]	-130

$M = N = 300$. Here, the optimization notices that U_2's performance is insufficient and identifies no purpose in arranging α to aid it and arranges α completely for U_1. This is why U_1's performance is very high. Once U_2's performance starts to reach an acceptable performance, the optimization switches on and arranges α for both users to enable NOMA. This is why there is a sharp spike in U_1's performance. Hence, U_1's performance degrades to a certain point. Then as the RIS size increases, both users' performance increase to very good values while NOMA continues to be executed by the RIS.

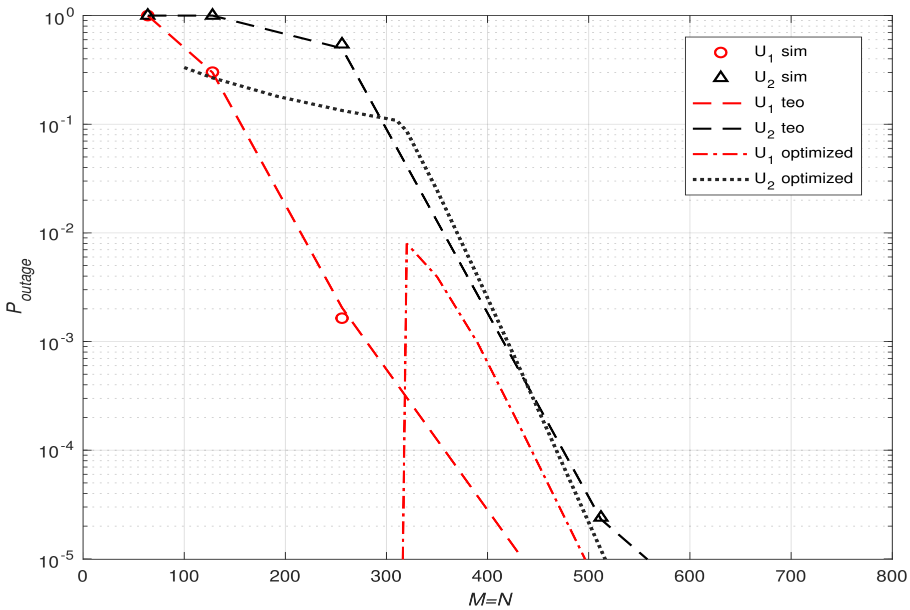

Figure 3.4: Outage probability performance with respect to varying RIS size.

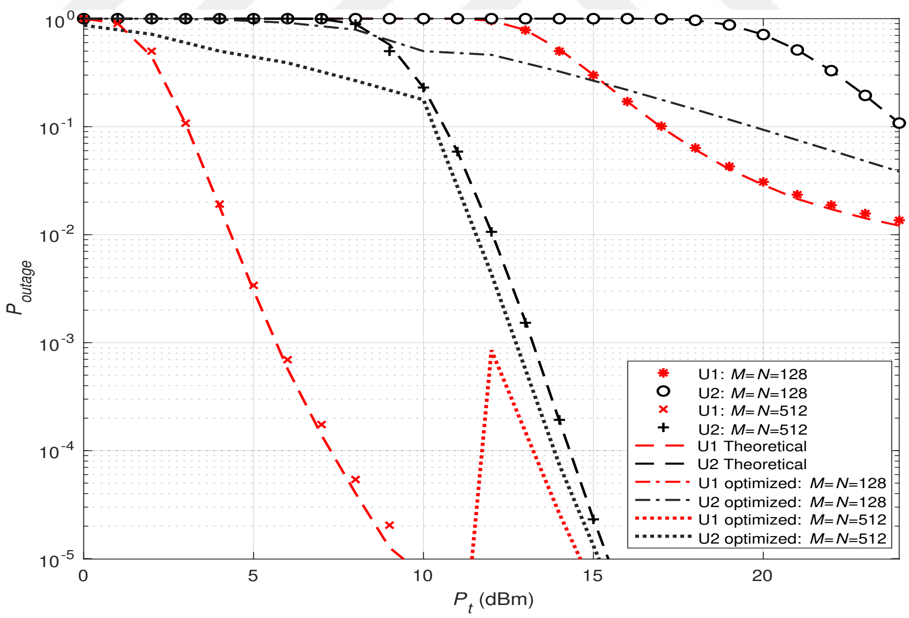

Figure 3.5: Outage probability performance as users transmit powers P_t vary.

Furthermore, Fig. 3.5 presents the outage probability of both users for a varying transmit power, P_t (dBm), of the users. It is observed that for both RIS sizes, an increase in P_t enhances the performance for both users. However, it should

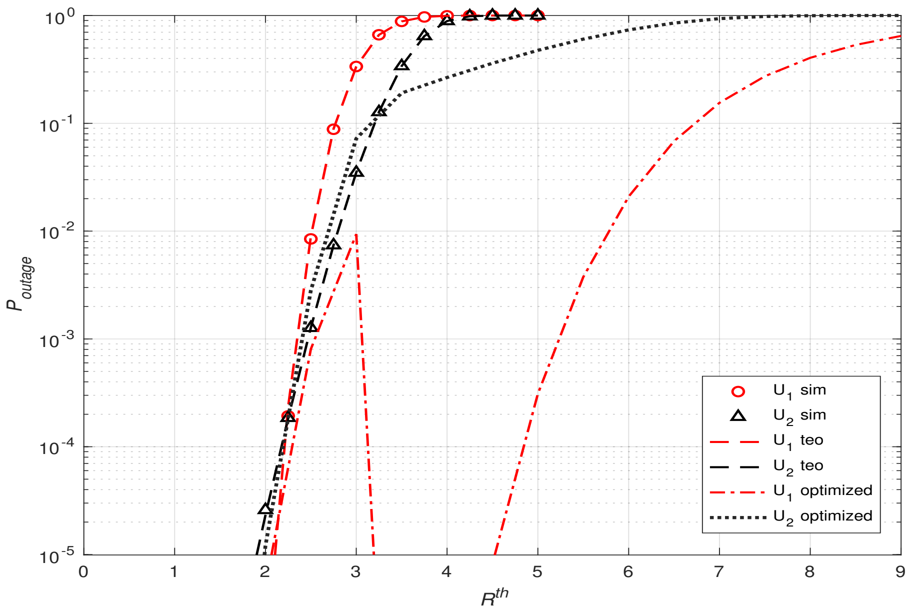

Figure 3.6: Outage probability performance of users as the QoS requirement is increased.

be noted that the maximum transmit power at the users for uplink is 23 (dBm) [Haider and Hwang, 2019]. It can be seen once more that as the RIS size increases, the performance drastically increases, especially for a high P_t. Additionally, for a smaller RIS size and high transmit powers, the performance reaches to a saturation and has an error floor. Hence, increasing the transmit power would not increase the performance after a certain point for a given RIS size. When comparing the fixed and optimized α scenarios, it is clear that the optimized case significantly outperforms the fixed α case. U_1 for $M = N = 128$ performance is very good below 10^{-5}, since U_2's performance is not great for a low RIS size and since uplink transmit power below 23 (dBm) is not enough to boost U_2. However for $M = N = 512$ we see that U_2 is in outage until around 9 dBm and hence, α is optimized only for U_1 enhancing its performance and reducing the outage probability. Once U_2 reaches 10^{-1}, α starts optimizing itself for both users and it can be seen from the spike of degradation in U_1's performance. However, as P_t increases to 14 dBm, both users provide excellent outage probability performance.

As the QoS requirement for a user's communication performance gets higher, the outage probability increases since it is harder to sustain that quality. This can be seen in Fig. 3.6 for both users presenting the fixed and optimized case. For the fixed user case, it can be seen that for both users, QoS of $R^{th} = 2$ bps/Hz is easily sustained for the default parameters and as the quality requirement increases the outage probability increases and by 4 bps/Hz both users are at outage. It should be noted that this is for the default parameters and the performance can be arranged to meet certain requirements by changing these parameters. However, with the same default parameters and only difference of using an optimized alpha, the QoS is enhanced drastically. Both users easily sustain the quality requirement from $0-2$ bps/Hz and the performance degrades as the QoS is increased to 3 bps/Hz. Since U_2's outage performance get very low at 3 bps/Hz, the α optimization disregards U_2 and arranges itself for U_1 thus, once again providing it outstanding performance below 10^{-5} which is shown by the spike down at $R^{th} = 3$. As the R^{th} increases to 9 bps/Hz, U_1's performance slowly degrades once again. However, it is clearly seen that when α is optimized, U_2 reaches complete outage at 7 bps/Hz rather than 4 bps/Hz at fixed α and U_1 reaches complete outage at approximately 11 bps/Hz rather than 3.3 bps/Hz at the fixed α case. Fig. 3.7 and 3.8 present the cases of perfect and imperfect SIC when U_2 decodes U_1's signal to subtract it from its received signal. Since U_1 is not affected by errors in SIC decoding, it is not included in these figures. In Fig. 3.7, we can see the outage probabilities for U_2 at default parameters with different SIC performances (ϵ values) while the transmit power of the RIS P_t^{RIS} varies. It is shown that perfect SIC ($\epsilon = 0$) provides the best performance whereas cases of imperfect SIC results in lower performance. Here, P_t^{RIS} is very low even though an active RIS is used. It should be noted that as the P_t^{RIS} value increases even further, the outage probability would approach to 0. However, since α is limited to a practical value of 1000, as we increase the P_t^{RIS}, U_2's performance does not improve after getting worse. At low transmit power, U_2 experiences great performance since α value is low and U_2 is aligned coherently at the passive section which strengthens the performance from the passive part making

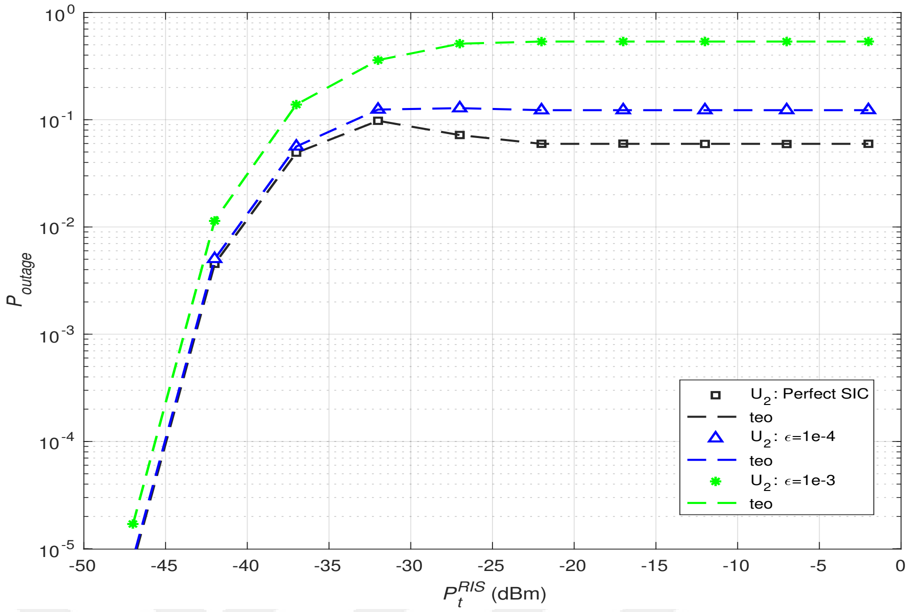

Figure 3.7: Affect of RIS transmit power with SIC imperfections to outage probability.

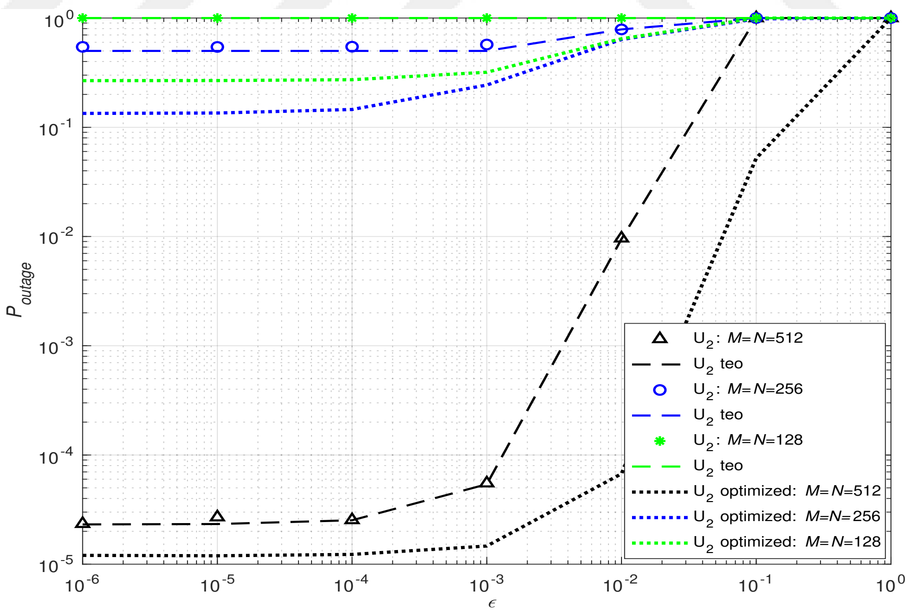

Figure 3.8: Effect of ϵ to outage probability

the active part of the hybrid RIS negligible. However, as P_t^{RIS} increases, the α value increases thus, the gap between the strength of the passive and active parts of the

RIS decreases. This decrease in difference of strength from both sides degrades the performance because as the active part of the RIS increases, the random phase alignment strength increases and corrupts the perfectly aligned coherent phase part of the passive part for U_2. As the P_t^{RIS} increases the active part will dominate the passive part and the outage probability performance will get better. However, since we limited α to a practical value, we see a saturation in the performance after -25 dbm. On the other hand, Fig. 3.8 presents the effect epsilon has to the outage probability performance of U_2 for fixed P_t^{RIS} and with different RIS sizes. As ϵ is closer to zero, the performance is the highest and get worse as ϵ approaches higher values meaning higher SIC errors. Once again, higher RIS sizes provides superior performance and the optimized alpha cases outperform the fixed α scenarios.

3.6.1 Bit-Error Rate

In order to decode the signals of U_1 and U_2, we employ the maximum-likelihood (ML) decision rule as follows:

$$\hat{x}_1 = \arg\min_{x \in \mathcal{C}} \|y - x\|^2,$$
$$\hat{x}_2 = \arg\min_{x \in \mathcal{C}} \|\tilde{y} - x\|^2, \tag{3.16}$$

where $\tilde{y} = \sqrt{P_t}(\sqrt{\alpha}\mathbf{h}_2^{\mathrm{T}}\bar{\boldsymbol{\theta}}\mathbf{h}_{BS} + \mathbf{g}_2^{\mathrm{T}}\bar{\boldsymbol{\beta}}\mathbf{g}_{BS})x_2 + \sqrt{\alpha}\mathbf{z}\bar{\boldsymbol{\theta}}\mathbf{h}_{BS} + w_0$, is the signal after perfect SIC and $\mathcal{C}$ is PSK/QAM constellation. While previous simulation results assume perfect CSI, Fig. 3.9 shows the BER performance of the proposed system taking into consideration imperfect CSI for $W_0 = -70$ dBm and $n_{amp} = -70$ dBm. The maximum-likelihood (ML) detection is performed by using $\hat{\mathbf{h}}_k$, $\hat{\mathbf{g}}_k$ and $\hat{\mathbf{h}}_{BS}$ instead of the actual channel coefficient vectors $\mathbf{h}_k$, $\mathbf{g}_k$ and $\mathbf{h}_{BS}$ in (3.2) to decode the transmitted signal similar to [Luong et al., 2018]. For example, we consider $\hat{\mathbf{h}}_k = \mathbf{h}_k - \mathbf{e}$, where $\mathbf{e}$ denotes the vector of channel estimation errors whose elements follow the distribution $\mathcal{CN}(0, \Delta)$ and Δ is the variance where $\Delta = [0, 1)$. The simulations in Fig. 3.9 are realized under $\Delta = 0.05$ and $\Delta = 0.1$. It can be observed for both users that as P_t increases, the BER improves and when CSI errors (Δ) exist the BER performance degrades. From the slope of the BER figures, the diversity

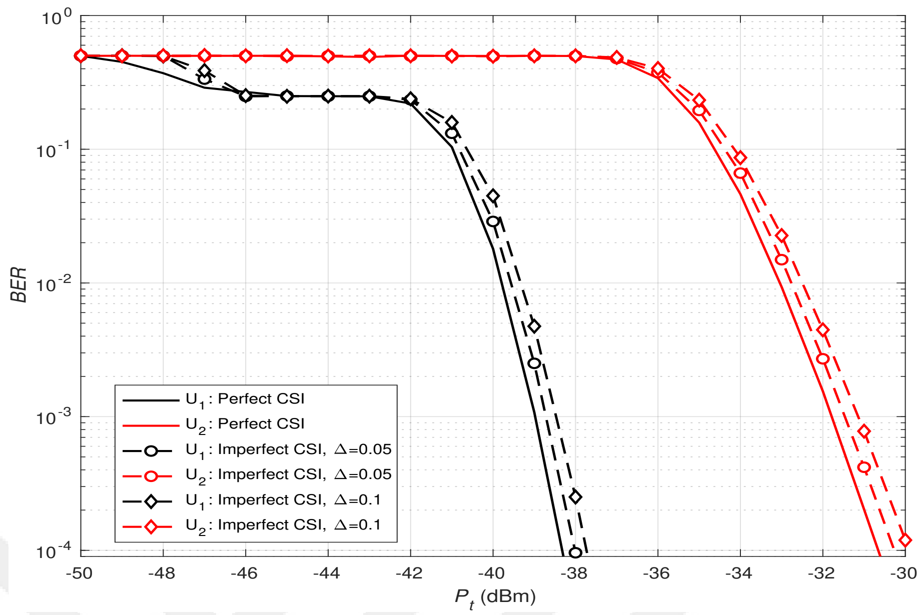

Figure 3.9: BER comparisons for perfect and imperfect CSI.

of both users can be observed. For the perfect CSI case, we can calculate that the diversity of U_1 and U_2 are 12 and 8, respectively. In addition the diversity order of U_1 and U_2 for the case of imperfect CSI where $\Delta = 0.05$ is 10 and 8, respectively.

3.6.2 Achievable Rate and Energy Efficiency

In Figs. 3.10 and 3.11, we compare the proposed NOMA hybrid RIS scheme's performance to conventional OMA where the RIS is fully active and fully passive. For the OMA fully passive RIS system, all of the RIS elements serve the user in their time-slot and no amplifiers exist. On the other hand, the OMA fully active RIS system has amplifiers at every elements of the RIS and all the elements serve the user at its time-slot. To ensure fairness, we keep P_t^{RIS} the same as when only half of the RIS is active, hence, the α factor halves but at every element of the RIS serving a single user at a time. In Fig. 3.10, the default parameters are considered and it can be seen that as P_t increases, so does the achievable rate of all scenarios. We can see the proposed hybrid RIS NOMA scheme falls in between the fully active OMA and fully passive OMA cases. Despite the proposed scheme using half of the

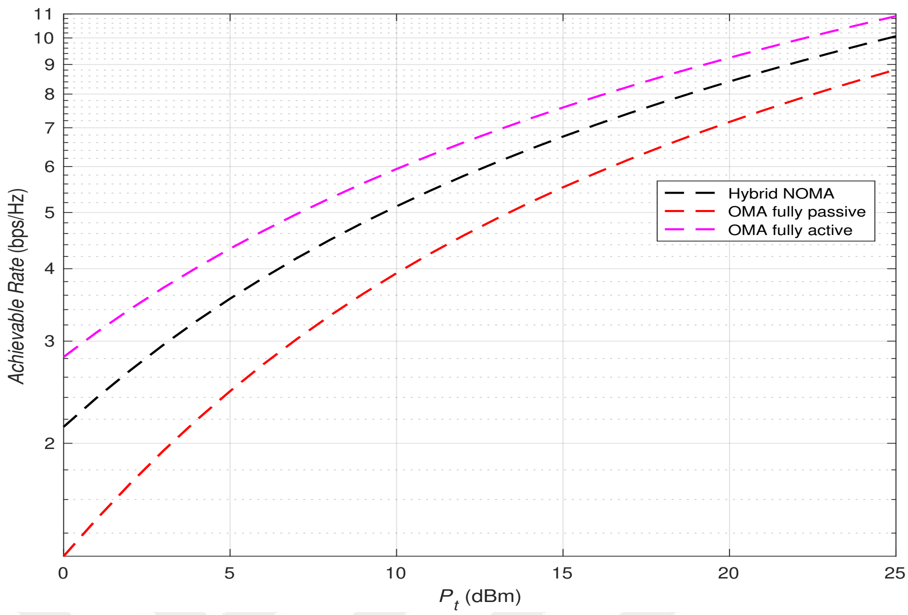

Figure 3.10: Achievable rate comparisons.

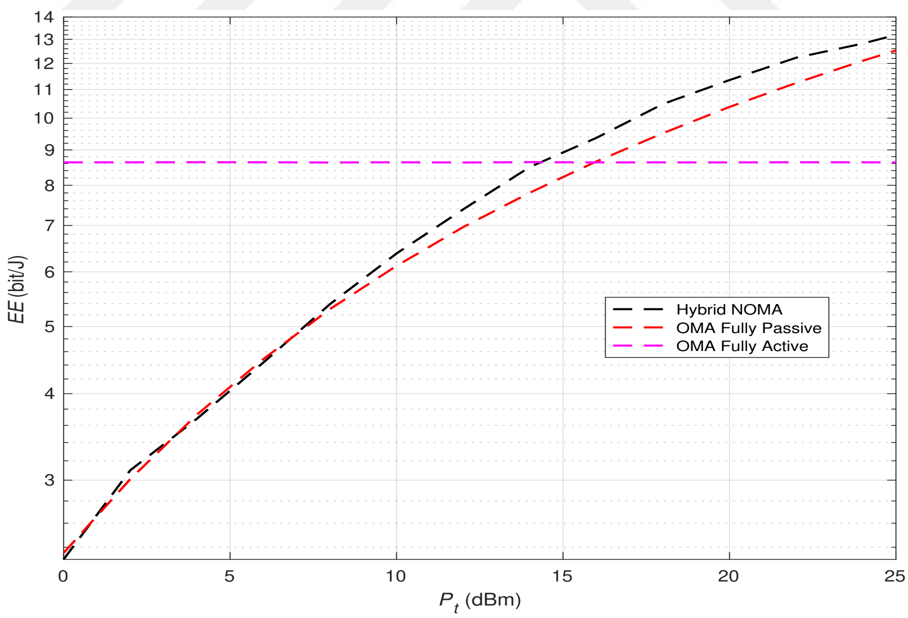

Figure 3.11: Energy efficiency comparisons.

elements compared to the fully active case, the achievable rate is closer to the fully active RIS OMA scenario rather than the fully passive RIS OMA scenario. It should be noted that sine we consider the BW equal to one, the figure also gives us insight of the spectral efficiency. Fig. 3.11 compares the EE of the three scenarios where we define the bit-per-joule EE as the total rate divided by the total power consumed at the RIS. Here we adjust $M = N = 256$, and the rest of the parameters are the default as previously stated. The total power consumption of the active and passive part of the RIS can be modeled as:

$$P_{RIS} = (P_t^{RIS} + M * P_m) + (N * P_n) \tag{3.17}$$

where P_m and P_n represent the power consumption a passive element of the RIS uses, which is considered as 1.5 mW [Huang et al., 2019c]. We optimally select α when calculating the EE in the proposed hybrid NOMA scenario. On the other hand in the OMA cases, to ensure a fair comparison, we use the average P_t^{RIS} from the optimized hybrid NOMA case which results in a non-optimized parameter of $P_t^{RIS} = -47.6$ dBm. The EE of the OMA fully active case remains constant because as P_t increases, the α value decreases hence, keeping the EE stable. OMA fully passive RIS EE increases as P_t increases. The OMA fully active case surpases the OMA fully passive case for $P_t \leq 16$ dBm because the rate is much higher for the fully active case when compared to the fully passive. However, after $P_t = 16$ dBm, the rate gained by the fully active case no longer exceeds the fully passive scenario. To elaborate, the additional power used at the fully active case after $P_t = 16$ dBm no longer provides a significant improvement in the rate of the system so the EE of the fully passive system exceeds the fully active case. In the proposed hybrid NOMA system, similar to the fully passive case, the fully active exceeds in EE due to numerous active elements boosting the rate however, after $P_t = 14$ dBm, the hybrid NOMA scenario exceeds the fully active case. Compared to the fully passive scenario, the proposed scheme is equivalent at lower P_t values but after $P_t = 8$ dBm, the proposed scheme begins to outperform the fully passive case.

3.7 Conclusion

The main motivation of this chapter is to propose a novel method to achieve power domain NOMA in the uplink, through the use of the hybrid RIS. Conventionally, while the power disparity of the users are implemented at either the users or the base-station, the power difference is performed over-the-air at the RIS. A thorough end-to-end system model along with theoretical calculations are provided and analyzed with various parameters. Future and open research areas include varying the size of the hybrid RIS partitions where they are not equal, further optimization of the alpha parameter, optimal placement of the RIS and other varying system parameters, and the possibility of considering other domains to enhance the NOMA performance.

Chapter 4

HYBRID RECONFIGURABLE INTELLIGENT SURFACE ENABLED OVER-THE-AIR INDEX-MODULATION

4.1 Preface

Users' desire for enhanced performance drive the inevitable technological progress on vertical applications in wireless communication systems. To meet these demands, researchers vigorously investigate potential 6G and beyond technologies and solutions. RISs have risen in popularity and attracted the attention of academia as well as industry and seem to be a promising candidate for 6G technology. RISs are reflective metamaterials with many configurable elements consisting of pin diodes that have the ability to manipulate the impinging signals' properties, hence, enabling some sort of virtual control over the wireless channel. In this chapter, we propose a novel over-the-air IM scheme through the use of a hybrid RIS with active and passive partitions to convey additional IM bits over-the-air. In addition we propose another modified scheme that allows the transmission for even more IM bits but at the expense of certain trade-offs. First, we present the system model for both of the proposed schemes. Furthermore, comprehensive computer simulation results are provided and discussed presenting the superior BER performance and additional benefits of the proposed systems compared to similar benchmarks.

4.2 Introduction

Wireless communication technologies are rapidly developing as researchers migrate from one generation (5G) to another (6G), striving to meet users' stringent demands as a consequence of imminent vertical applications. Numerous candidate solutions and novel technologies are proposed in the literature each manifesting high potential for future wireless communication systems. While some methods are adopted, most of these are dismissed and are not favored due to distinct drawbacks and critical issues which may be in terms of practicality, performance, complexity and more. However, as new hot topics arise, researchers must revert to previous solutions and consider them and their integration with recently developed and considered technologies which may provide new insights and together provide superior performance. Hence, previously dismissed technologies may be rekindled as once again significantly promising solutions.

IM is a simple, spectrum and energy efficient scheme to embed and transmit additional information bits through the indices of resource blocks in communication systems [Basar, 2016, Basar et al., 2017, Wen et al., 2017, Tugtekin et al., 2023]. These resource blocks on which information is embedded can be subcarriers, antennas, time-slots, constellation, activation orders and much more [Sugiura et al., 2017, Wen et al., 2017]. It is a very popular concept with a significant amount of research and studies conducted on it and has proven itself to be a worthy tool and is considered for future communication networks. IM shows benefits such as the ability to improve error performance, provide enhanced energy and spectral efficiency, and all while providing low complexity [Cheng et al., 2018]. One of the most important characteristic of IM is its flexibility and compatibility attribute since it can be employed and coexist in a wireless communication system in numerous methods [Sugiura et al., 2017, Mao et al., 2018]. One example is orthogonal frequency division multiplexing-IM (OFDM-IM) where IM is incorporated in the subcarriers of an OFDM waveform as an addition layer of modulation by activating certain subcarriers to transmit additional bits over OFDM subblock [Başar et al., 2013, Wen et al., 2015]. In [Arslan et al., 2020a] and [Şahin et al., 2021], IM has been integrated with non-orthogonal multiple access and joint radar and communication technologies introducing novel system designs for future technologies; proposing a flexible OFDM-IM subcarrier activation and power allocation method according to users' needs and a unique waveform to serve both communication and radar functionalities, respectively. Furthermore, additional interesting studies have been conducted such as [Mao et al., 2016] where a novel technique is proposed by dividing the subcarriers into two groups and modulating them with distinguishable mode constellations and [Arslan et al., 2020b] where bits are transmitted through the indexing of multiple codebooks to be used in sparse vector coding for ultra-reliable low-latency communication networks.

RISs have recently risen in popularity in the wireless communication community and exhibit high potential as a promising candidate for future 6G and beyond wireless communication systems. RISs are large reflective surfaces with numerous small and low-cost meta-material elements that have the ability to manipulate the characteristics of impinging signals. Hence, RISs are able to reflect, refract, absorb and even amplify impinging signals without the need for additional buffering or processing, providing some sort of virtual control over the wireless channel. Generally, RISs are envisioned to be employed for coverage enhancement, increased signal quality, elevated capacity and other system performance improvements [Subrt and Pechac, 2012, Huang et al., 2020a, Kilinc et al., 2021b, Su et al., 2020b, Perović et al., 2020, Yigit et al., 2022]. One significant advantage of the RIS technology is its flexibility in the integration with conventional technologies. There are many studies that present substantial benefits in the integration of RIS with previously considered technologies such as non-orthogonal multiple accessing [Arslan et al., 2022a], machine learning [Huang et al., 2019b], localization [Ma et al., 2020], OFDM [Pradhan et al., 2020], mutiple-input and multiple-output [Tang et al., 2020], and much more [Alayasra and Arslan, 2022, Arslan et al., 2023a, Arslan et al., 2022b].

Considering both the advantages and flexibility of RIS and IM, the integration of these technologies are being investigated to further improve wireless communication system performances. In [Dash et al., 2022], the authors present a greedy detector for an RIS space-shift keying system where the RIS phases are aligned to maximize the instantaneous SNR at the target receive antenna which is selected through IM bits. Furthermore, an intelligent RIS grouping-based IM (RGB-IM) is proposed to enhance the spectral efficiency and BER performance of conventional RIS systems

[Asmoro and Shin, 2022]. In this study the RIS is divided in to multiple groups each with the same number of elements, and according to the incoming IM bits a group of RIS elements are activated while the other RIS elements are inactive and introduce zero phase. However, completely inactivating remaining groups and elements are not optimal and could be used in a more efficient manner to improve the reliability and spectral efficiency of the system.

In this chapter, we propose a novel over-the-air RIS-IM (OTA-RIS-IM) technique exploiting the entire RIS enhancing the spectral efficiency and BER performance. We present a hybrid RIS that has multiple groups and each group can be active and passive according to the IM bits. Furthermore, we further expand this system design and propose an enhanced OTA-RIS-IM (E-OTA-RIS-IM) system by introducing an absorption mode at the RIS to send additional IM bits at the expense of slightly reduced BER performance improvement compared to our benchmark.

The rest of the chapter can be summarized as follows. In chapter 4.3, the system framework of the proposed OTA-RIS-IM and E-OTA-RIS-IM scheme is presented. In addition, chapter 4.4 consists of the computer simulation results and discussions while chapter 4.5 concludes the chapter.

4.3 System Model

In this subchapter, we provide the system model for both of the proposed schemes. First we will present the initial OTA-RIS-IM system design. Furthermore, we will build on top of it to propose the E-OTA-RIS-IM system. As seen from Fig. 4.1, RIS includes N elements and is partitioned into G groups, each including $\bar{N}$ elements, $N = G\bar{N}$. Here, the reflection coefficient of the ith element of the gth RIS group is $\theta_{gi} = e^{j\vartheta_{gi}}$ with unit amplitude, where $\vartheta_{gi} \in [0, 2\pi)$ is the phase shift adjusted by the RIS controller, $i = 1, 2, \cdots, \bar{N}$, and $g = 1, 2, \cdots, G$.

Assume that $L_h = \zeta_0 d_h^{-\varkappa_h}$ and $L_f = \zeta_0 d_f^{-\varkappa_f}$ represent the large scale path loss of the BS-to-RIS and RIS-to-UE, respectively, where ζ_0, is the path loss at the reference distance of 1 meter, and d_h, d_f and $\varkappa_h$, $\varkappa_f$ denote the distance from BS to RIS and RIS to UE, the path loss exponents at BS to RIS and RIS to UE paths,

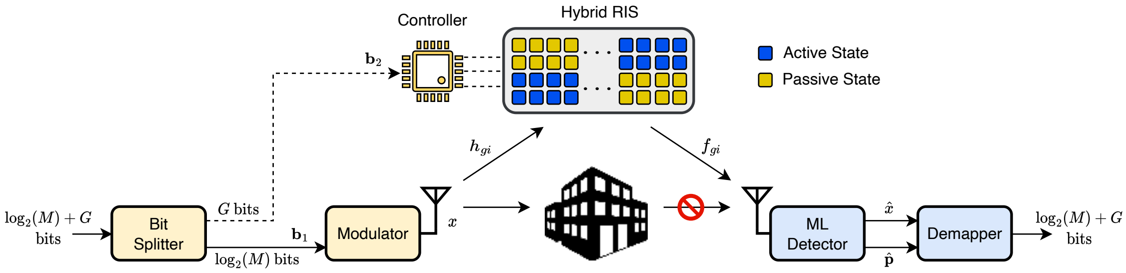

Figure 4.1: System model of OTA-RIS-IM.

respectively. Then, we define the channel coefficients from the BS to the (g,i)th RIS element and from the (g,i)th RIS element to the UE as $h_{gi} = |h_{gi}|\, e^{j\phi_{gi}} = \sqrt{L_h}\bar{h}_{gi}$ and $f_{gi} = |f_{gi}|\, e^{j\varphi_{gi}} = \sqrt{L_f}\bar{f}_{gi}$, respectively. Moreover, $\bar{h}_{gi}$ and $\bar{f}_{gi}$ are independent Rician fading channel coefficients as follows:

$$\bar{h}_{gi} = \sqrt{\frac{K_h}{K_h+1}}\bar{h}_{gi}^{\mathrm{LoS}} + \sqrt{\frac{1}{K_h+1}}\bar{h}_{gi}^{\mathrm{NLoS}}, \tag{4.1}$$

$$\bar{f}_{gi} = \sqrt{\frac{K_f}{K_f+1}}\bar{f}_{gi}^{\mathrm{LoS}} + \sqrt{\frac{1}{K_f+1}}\bar{f}_{gi}^{\mathrm{NLoS}}, \tag{4.2}$$

where $\bar{h}_{gi}^{\mathrm{LoS}}$ and $\bar{f}_{gi}^{\mathrm{LoS}}$ represent the line-of-sight (LoS) components and $\bar{h}_{gi}^{\mathrm{NLoS}}$ and $\bar{f}_{gi}^{\mathrm{NLoS}}$ represent the non-LoS (NLoS) components of $\bar{h}_{gi}$ and $\bar{f}_{gi}$, respectively, whereas K_h and K_f denote the Rician K factor of the paths between the BS-RIS and the RIS-UE, respectively. Here, $\bar{h}_{gi}^{\mathrm{LoS}}$, $\bar{f}_{gi}^{\mathrm{LoS}}$, $\bar{h}_{gi}^{\mathrm{NLoS}}$, and $\bar{f}_{gi}^{\mathrm{NLoS}}$ are independent and identically distributed complex Gaussian random variables with $\mathcal{CN}(0,1)$.

4.3.1 OTA-RIS-IM

The system model of OTA-RIS-IM is demonstrated in Fig. 4.1. In OTA-RIS-IM, information bits are transmitted both through the conventional M-ary PSK/QAM signal constellation and also the indices of the active/passive states of RIS groups. Firstly, $\mathbf{b}_1 = [b_{11}, b_{12}, \cdots, b_{1\kappa}]^{\mathrm{T}}$ bit vector is mapped into the modulated symbol x, $x \in \mathcal{M}$, where $\mathcal{M}$ is the M-ary PSK/QAM signal constellation and $\kappa = \log_2(M)$. Then, $\mathbf{b}_2 = [b_{21}, b_{22}, \cdots, b_{2G}]^{\mathrm{T}}$ bit vector determines the indices of active/passive states of RIS groups $\mathbf{p} = [p_1, p_2, \cdots, p_G]^{\mathrm{T}}$, $p_g \in \{0,1\}$, $g = 1, 2, \ldots, G$. Here, the

gth element of $\mathbf{p}$ is equal to the gth element of $\mathbf{b}_2$, i.e., $p_g = b_{2g}$. If p_g is equal to 0 ($\bar{p}_g = 1$), then the gth RIS group is in passive state, and if p_g is equal to 1 ($\bar{p}_g = 0$), then the gth RIS group is in active state, where $\bar{p}_g$ represents the logical NOT of p_g. Here, the number of ones and zeros in $\mathbf{p}$ is equal to the number of active (G_A) and passive (G_P) RIS groups, respectively, $G_A + G_P = G$. In Table 4.1, an example of bit mapping is given for $G = 2$. The spectral efficiency of OTA-RIS-IM in terms of bit per channel use (bpcu) can be given as:

$$\eta = \log_2(M) + G. \tag{4.3}$$

In OTA-RIS-IM, the (g,i)th RIS element (θ_{gi}) is selected in such a way that the phase terms in h_{gi} and f_{gi} are eliminated, i.e., $\vartheta_{gi} = -(\phi_{gi} + \varphi_{gi})$. Hence, the received signal at UE can be given as:

$$y = \sqrt{P_t}x\left(\sum_{g=1}^{G}\left[\mathcal{H}_g\left(\sqrt{\alpha}p_g + \bar{p}_g\right) + p_g w_g^a\right]\right) + w, \tag{4.4}$$

$$\mathcal{H}_g = \sum_{i=1}^{\bar{N}} h_{gi}\theta_{gi}f_{gi} = \sum_{i=1}^{\bar{N}} |h_{gi}|\,|f_{gi}|,$$

$$w_g^a = \sqrt{\alpha}\sum_{i=1}^{\bar{N}} \theta_{gi}f_{gi}v_{gi},$$

where P_t, α, w, and v_{gi} are the transmit power, amplification factor at the active RIS groups, additive white Gaussian noise (AWGN) sample with distribution $\mathcal{CN}(0, N_0)$, and amplifier noise term at the (g,i)th RIS element with distribution $\mathcal{CN}(0, V_0)$, respectively. Finally, at the UE, the maximum-likelihood (ML) detection rule can be exploited to decode the received signal as follows:

$$(\hat{x}, \hat{\mathbf{p}}) = \underset{x\in\mathcal{M},\mathbf{p}\in\mathcal{P}}{\arg\min}\left\|y - \sqrt{P_t}x\left[\sum_{g=1}^{G}\mathcal{H}_g\left(\sqrt{\alpha}p_g + \bar{p}_g\right)\right]\right\|^2, \tag{4.5}$$

where $\hat{x}$ and $\hat{\mathbf{p}}$ are the estimates of x and $\mathbf{p}$, respectively, and $\mathcal{P}$ is a set including all possible $\mathbf{p}$ vectors. Here, $M2^G$ number of iterations are performed in the search space to decode the received signal.

The signal-to-noise ratio (SNR) of the received signal can be given as:

$$\gamma = \frac{P_t\left|\sum_{g=1}^{G}\mathcal{H}_g\left(\sqrt{\alpha}p_g + \bar{p}_g\right)\right|^2}{\alpha V_0\sum_{g=1}^{G}p_g\sum_{i=1}^{\bar{N}}\left|\theta_{gi}f_{gi}\right|^2 + N_0}. \tag{4.6}$$

Table 4.1: OTA-RIS-IM Example of Bit Mapping For $G = 2$

$[b_{21}, b_{22}]$	G_A	G_P	$[p_1, p_2]$	$[\bar{p}_1, \bar{p}_2]$	**First RIS Group State**	**Second RIS Group State**
$[0, 0]$	0	2	$[0, 0]$	$[1, 1]$	Passive	Passive
$[0, 1]$	1	1	$[0, 1]$	$[1, 0]$	Passive	Active
$[1, 0]$	1	1	$[1, 0]$	$[0, 1]$	Active	Passive
$[1, 1]$	2	0	$[1, 1]$	$[1, 1]$	Active	Active

4.3.2 E-OTA-RIS-IM

In this subchapter, we present an enhanced OTA-RIS-IM scheme (E-OTA-RIS-IM) to further improve the number of bits transmitted in the system by introducing an absorption state at the hybrid RIS. The system model of E-OTA-RIS-IM is illustrated in Fig. 4.2. Here, according to the incoming bits from the backhaul link, the hybrid RIS will determine whether the partitions will behave in the passive, active or absorption state. As in OTA-RIS-IM, firstly, $\mathbf{b}_1 = [b_{11}, b_{12}, \cdots, b_{1\kappa}]^{\mathrm{T}}$ bit vector is used to obtain the M-ary modulated symbol x, $\kappa = \log_2(M)$. Let us define a codebook $\mathcal{S}$ which includes all permutations with repetition of active/passive/absorption states of RIS groups, $\mathcal{S} = \{\mathbf{s}_1, \mathbf{s}_2, \cdots, \mathbf{s}_{2^{\varpi}}\}$, $\varpi = \lfloor \log_2 \left(3^G\right) \rfloor$, where $\mathbf{s}_{\varrho} = [s_{\varrho 1}, s_{\varrho 2}, \cdots, s_{\varrho G}]^{\mathrm{T}}$ is the ϱth codeword of set $\mathcal{S}$ and $s_{\varrho\mu} \in \{\sqrt{\alpha}, 1, 0\}$, $\varrho = 1, 2, \cdots, 2^{\varpi}$, $\mu = 1, 2, \cdots, G$. Here, $s_{\varrho\mu}$ being α, 1, and 0 represent active, passive, and absorption states, respectively. Hence, $\mathbf{b}_2 = [b_{21}, b_{22}, \cdots, b_{2\varpi}]^{\mathrm{T}}$ bit vector is converted into its decimal value (ξ), and ξth codeword ($\mathbf{s}_{\xi}$) of $\mathcal{S}$ is selected. As seen in Table 4.2, an example of states of RIS groups selection is provided for $G = 2$. Here, a total number of 3^G permutations can be generated; however, only 2^{ϖ} can be used to transmit information. As can be seen in the table, for the same number of RIS partitions G, we can send an additional bit compared to the previous method. Hence, the spectral efficiency

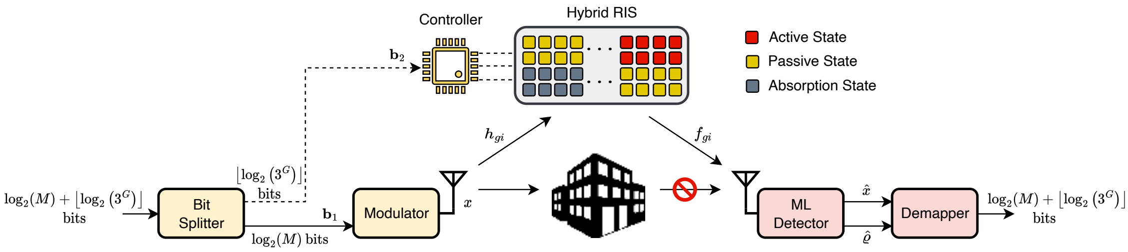

Figure 4.2: System model of E-OTA-RIS-IM.

of E-OTA-RIS-IM in terms of bpcu can be given as:

$$\eta = \log_2 (M) + \left\lfloor \log_2 \left(3^G\right) \right\rfloor . \tag{4.7}$$

As in OTA-RIS-IM, the (g, i)th element of RIS is coherently aligned with the corresponding channel coefficients h_{gi} and f_{gi}, i.e., $\vartheta_{gi} = -(\phi_{gi} + \varphi_{gi})$. Hence, the received signal at UE can be written as:

$$y = \sqrt{P_t} x \left(\sum_{g=1}^{G} \left[\mathcal{H}_g s_{\xi g} + \sigma \left(s_{\xi g}\right) w_g^a \right] \right) + w, \tag{4.8}$$

where $\sigma(\beta)$ is a function which provides output as 1 if β equals to $\sqrt{\alpha}$, and 0 otherwise.

In order to decode the received signal, the ML detector can be used as follows:

$$(\hat{x}, \hat{\varrho}) = \underset{x \in \mathcal{M}, \varrho = 1, \cdots, 2^{\varpi}}{\arg\min} \left\| y - \sqrt{P_t} x \left[\sum_{g=1}^{G} \mathcal{H}_g s_{\varrho g} \right] \right\|^2 . \tag{4.9}$$

Moreover, the SNR of the received signal can be obtained as:

$$\gamma = \frac{P_t \left| \sum_{g=1}^{G} \mathcal{H}_g s_{\xi g} \right|^2}{\alpha V_0 \sum_{g=1}^{G} \sigma\left(s_{\xi g}\right) \sum_{i=1}^{\bar{N}} \left|\theta_{gi} f_{gi}\right|^2 + N_0}. \tag{4.10}$$

4.4 Simulation Results and Comparisons

In this subchapter, we will discuss the simulation results of the proposed OTA-RIS-IM and E-OTA-RIS-IM schemes in terms of BER performance compared to the RGB-IM benchmark [Asmoro and Shin, 2022] which only activates one group of the

Table 4.2: E-OTA-RIS-IM Example of Bit Mapping For $G = 2$

Index Bits $[b_{21}, b_{22}, b_{23}]$	(ξ)	**Codeword**	**First RIS Group State**	**Second RIS Group State**
$[0, 0, 0]$	0	$\mathbf{s}_1 = [\sqrt{\alpha}, \sqrt{\alpha}]^{\mathrm{T}}$	Active	Active
$[0, 0, 1]$	1	$\mathbf{s}_2 = [\sqrt{\alpha}, 1]^{\mathrm{T}}$	Active	Passive
$[0, 1, 0]$	2	$\mathbf{s}_3 = [\sqrt{\alpha}, 0]^{\mathrm{T}}$	Active	Absorption
$[0, 1, 1]$	3	$\mathbf{s}_4 = [1, \sqrt{\alpha}]^{\mathrm{T}}$	Passive	Active
$[1, 0, 0]$	4	$\mathbf{s}_5 = [1, 1]^{\mathrm{T}}$	Passive	Passive
$[1, 0, 1]$	5	$\mathbf{s}_6 = [1, 0]^{\mathrm{T}}$	Passive	Absorption
$[1, 1, 0]$	6	$\mathbf{s}_7 = [0, 1]^{\mathrm{T}}$	Absorption	Active
$[1, 1, 1]$	7	$\mathbf{s}_8 = [0, 1]^{\mathrm{T}}$	Absorption	Passive
NaN	NaN	NaN	Absorption	Absorption

RIS. For a different number of RIS groups G, various M, N and other parameters, we show the superior performance of the proposed scheme over the RGB-IM. Unless otherwise indicated, the following system parameters are assumed in all simulations: the distances $d_h = 20$ and $d_f = 50$ meters, the path loss exponents $\varkappa_h = 2.2$ and $\varkappa_f = 2.8$, the Rician shape parameters $K_h = K_f = 0$, the noise variances and the reference path loss value of $\zeta_0 = -30$ dB. For the BER analyses, the noise power N_0 and V_0 are fixed to -130 dBm and the transmit power P_t is varied.

Fig. 4.3 presents the error performance for all schemes with $G = 2$, $N = 256$, and 4 bpcu for varying α. It is observed that E-OTA-RIS-IM requires the least modulation order of $M = 2$ since it can transmit additional bits through IM and is the most spectral efficient. On the other hand, OTA-RIS-IM needs $M = 4$ and RGB-IM benchmark operates at $M = 8$ modulation orders to keep the same bpcu

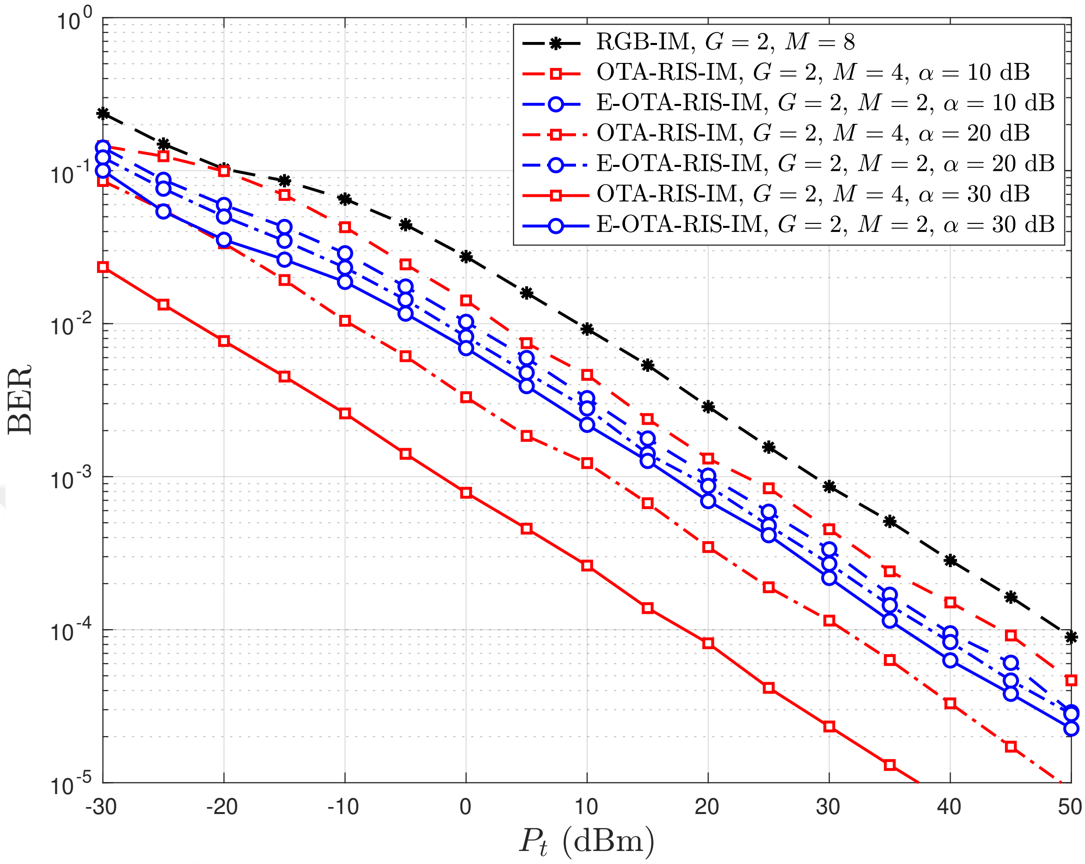

Figure 4.3: Error performance comparison of OTA-RIS-IM, E-OTA-RIS-IM, and RGB-IM for varying α, $N = 256$, and 4 bpcu.

of 4. It is seen that both proposed schemes outperform the benchmark and OTA-RIS-IM provides the best performance of all schemes since it uses the entire RIS at all times due to not having absorption state as in E-OTA-RIS-IM and RGB-IM. Furthermore, the error performance of all schemes improves with respect to α.

In Fig. 4.4, we can see the BER performance of the proposed schemes compared to the benchmark with $G = 2$ for varying N. To obtain same bpcu values in each scheme, the modulation order varies. It is observed that while E-OTA-RIS-IM needs only $M = 2$, OTA-RIS-IM needs to operate at $M = 4$ modulation order. Despite a higher modulation order, OTA-RIS-IM outperforms E-OTA-RIS-IM in terms of error performance since it has all RIS elements on at all combinations. On the other hand, RGB-IM requires $M = 8$ modulation order to keep up the same data rate. It

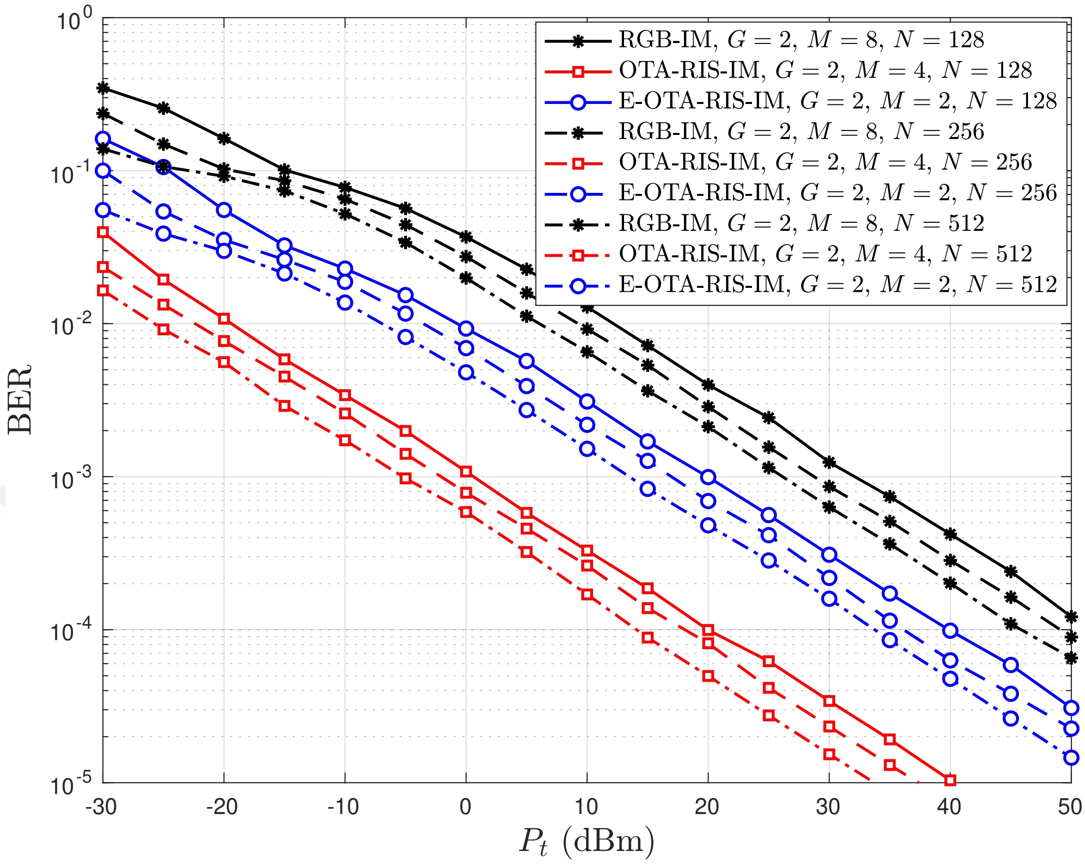

Figure 4.4: Error performance comparison of OTA-RIS-IM, E-OTA-RIS-IM, and RGB-IM for varying N, $\alpha = 30$ dB, and 4 bpcu.

is shown that the RGB-IM at the same bpcu performs significantly worse compared to both of the proposed schemes.

Fig. 4.5 presents the BER performance of the proposed systems compared to the benchmark when all of the systems are at the same bpcu and $M = 2$. As we can see, to reach the same bpcu RGB-IM requires a large amount of grouping G to send additional bits through IM. On the other hand, OTA-RIS-IM needs only $G = 4$ RIS groups to reach the same bpcu and E-OTA-IM needs even a fewer number $G = 3$ since it has an additional state the hybrid RIS can take. It can also be observed that since there is no absorption state, even though the bpcu is less compared to E-OTA-RIS-IM, the BER performance is significantly superior because all RIS elements are exploited at all times.

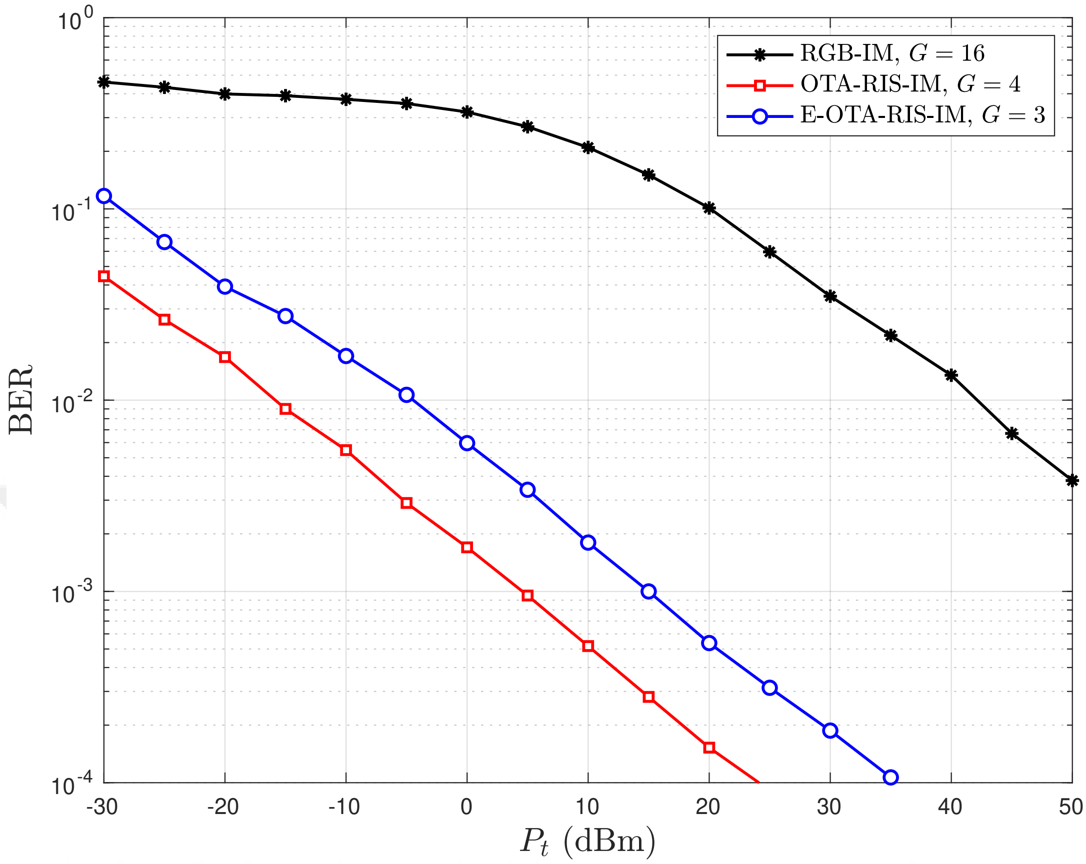

Figure 4.5: Error performance comparison of OTA-RIS-IM, E-OTA-RIS-IM, and RGB-IM varying G, $M = 2$, $\alpha = 30$ dB, $N = 480$, and 5 bpcu.

Fig. 4.6 shows the increase in bpcu as the number of groups G increases for each scheme. It can be observed, that as the number of groups increases the benchmark's bpcu does not increase much since only one group is activated according to the $\lfloor \log_2(G) \rfloor$ IM bits each time and the rest of the RIS is inactive. On the other hand, OTA-RIS-IM uses the entire hybrid-RIS where each group may take an active and passive state according to G IM bits and provides a significantly higher bpcu compared to the benchmark. Furthermore, E-OTA-RIS-IM introduces an absorption state at the RIS to further enhance the bpcu for a trade-off from reliability as we have seen from the previous BER figures. However, we can observe that the bpcu increases drastically for the E-OTA-RIS-IM scheme since the IM bits are increased to $\lfloor \log_2(3^G) \rfloor$.

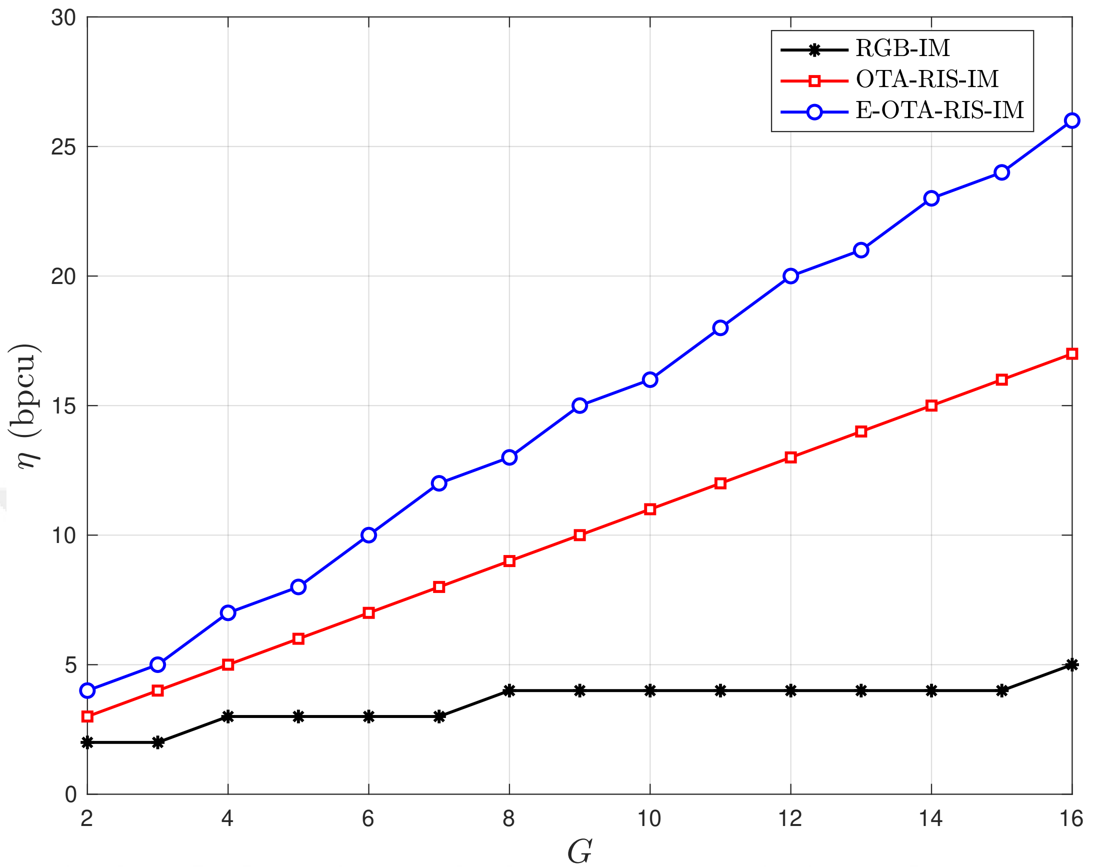

Figure 4.6: Spectrall efficiency comparison of all schemes for varying G and $M = 2$.

4.5 Conclusion

In this chapter, a novel OTA-RIS-IM and E-OTA-RIS-IM scheme has been proposed, exploiting the benefits of IM and RIS technology efficiently to enhance the spectral efficiency and BER performance of RIS-aided wireless communication systems. Through partitioning and varying the states of the groups at the hybrid-RIS, additional IM bits are conveyed over-the-air. Furthermore, extensive computer simulation results demonstrate and discuss the performance benefits of the proposed system. Future directions may include applications of machine learning, various methods to improve the transmission of IM bits, considering a multiple antenna system design, and other methods to further improve the performance and complexity of the proposed system design.

Chapter 5

NETWORK-INDEPENDENT AND USER-CONTROLLED RIS: AN EXPERIMENTAL PERSPECTIVE

5.1 Preface

The march towards 6G is accelerating and future wireless network architectures require enhanced performance along with significant coverage especially, to combat impairments on account of the wireless channel. RIS technology is a promising solution, that has recently been considered as a research topic in standards, to help manipulate the channel in favor of users' needs. Generally, in experimental RIS systems, the RIS is either connected to the transmitter (Tx) or receiver (Rx) through a physical backhaul link and it is controlled by the network and requires significant computation at the RIS for codebook (CB) designs. In this chapter, we propose a practical user-controlled RIS system that is isolated from the network to enhance communication performance and provide coverage to the user based on its location and preference. Furthermore, a low-complexity algorithm is proposed to aid in CB selection for the user, which is performed through the wireless cloud to enable a passive and energy efficient RIS. Extensive experimental test-bed measurements demonstrate the enhanced performance of the proposed system while both results match and validate each other.

5.2 Introduction

Driven by the strict requirements and various applications for future 6G and beyond wireless communication systems, researchers from academia as well as industry have shown significant interest to the fairly new and developing but exceptionally promising RIS technology. RISs are comprised of a large number of small, low-cost, passive meta-material elements that acquire the ability to manipulate impinging signals such as reflect, absorb, and refract, hence allowing some sort of control over the wireless channel. RIS technology is seen as an alternative to beamforming techniques that require a large number of antennas to direct signals, without the need for additional buffering or processing. RISs may introduce phase shifts that can be controlled by software to impinging signals in an intelligent manner to enhance coverage, improve signal quality, boost capacity, and much more [Subrt and Pechac, 2012, Huang et al., 2020a, Kilinc et al., 2021b, Su et al., 2020b, Perović et al., 2020].

RISs have been utilized in novel ways and integrated with existing technologies to incorporate the flexibility and advantages of multiple technologies. While equalization is conventionally performed at the Tx or Rx in frequency selective channels, the RIS is exploited to virtually equalize the channel over-the-air in [Arslan et al., 2022b]. In [Arslan et al., 2022a], non-orthogonal multiple access (NOMA) in the uplink is enabled over-the-air using an hybrid RIS where the RIS is partitioned to active and passive sections. Furthermore, coverage extension is investigated in [Zeng et al., 2020] and [Tapio et al., 2021b] while [Tasci et al., 2022c, Huang et al., 2019d, Hua et al., 2021b] provides solutions for energy efficiency for RIS systems without the use of additional RF chains. Generally, RISs function in the most ideal manner for cases where a direct line-of-sight does not exist or is weak [Zhang et al., 2022b, Yang et al., 2020c]. Another issue that must be taken into consideration for RIS systems is the multiplicative path loss of the Tx-RIS-Rx link, hence, making significant gains difficult especially in outdoor scenarios [Zhang et al., 2022b, Wu et al., 2021c].

The issues mentioned above are more prevalent in practical and experimental studies with limitations. RIS literature is becoming saturated from a theoretical and simulative perspective however, it is lacking and in need of practical and experimental studies especially since it is a study item envisioned to be in use commercially for future communication systems. There are currently ongoing pre-standardization efforts on ETSI to push the RIS technology into 6G standards [ETS, 2023a, ETS, 2023b]. Some experimental studies include [Araghi et al., 2022] where the authors investigate the received power performance using horn antennas for an L-shaped indoor scenario and aim to enhance performance for blind spots. In [Rains et al., 2022], similarly, a multi-bit RIS is deployed for coverage enhancement in an L-shaped indoor scenario with non line-of-sight (NLOS) with horn antennas. Additionally, a 1-bit RISs with 1100 elements for self- adaptive reflection is tested for indoor/outdoor environments in [Pei et al., 2021a].

The authors in [Kayraklık et al., 2022] aim to enhance indoor coverage using a physical RIS and also propose a codebook (CB) design without feedback channels. A few major points in this work that deteriorates the practicality of the system is that both the Tx and Rx use horn antennas and that they only consider a discrete number of training points where if you fall in between those exact points you suffer a significant reduction in received signal power. Furthermore, the system needs to train the RIS at each point through extensive measurements based on the Rx signal power where the Rx and RIS are connected to each other via a wire. The CB selection applied is based on trial and error of each individual RIS elements or a group of RIS elements turning on and off and observing the received signal power; which is impractical when it comes to daily use of customers requiring time and power.

Based on the works mentioned previously, generally RIS systems are designed in impractical ways to acquire significant gains and show improvement in communication. The use of horn antennas at both ends, extensive offline training before use of the RIS, physical back-haul links connecting the RIS to the Tx or Rx, unrealistic channel state information (CSI) requirements, exhaustive CB algorithms, and the RIS being dependent and connected to the network during online and offline use are just a few important factors that reduce the practicality of an RIS system.

In this chapter, we introduce a unique user-based perspective and aim to significantly improve the practicality of the RIS and isolate it from the network when in use. The user at the receiving end is equipped with an omni-directional antenna hence reflections from walls and obstacles around it will also be considered, which is typically not the case in most studies. There is no CSI required and no physical link between the receiving user and RIS, instead, feedback is provided through Wi-Fi which is available in most indoor locations. The RIS is completely independent from the Tx at all times and also when serving the receiving user. The only time the RIS is wirelessly connected to the Rx through Wi-Fi is when the indoor user requests to quickly update or add new CBs in an efficient manner. At any other case, the user sends short commands to the RIS only to change the RIS CB configuration to the users preference via online application/remote control. Additionally, we take into consideration the time for CB generation when requested by the user and propose an efficient and enhanced CB selection algorithm to quickly serve and boost user performance based on received signal power.

The major contributions of this chapter can be summarized as follows:

- A unique perspective to an end-to-end user-controlled RIS scenario is considered.
- A practical user-controlled RIS system isolated from the network is proposed.
- A novel CB selection algorithm is proposed to favor a passive RIS with efficiency, low complexity, and enhanced performance.
- Extensive experimental results with a test-bed are provided to compliment and validate the effectiveness of the proposed CB algorithm and RIS scenario.

The rest of the chapter can be summarized as follows. In chapter 5.3, the system framework of the proposed RIS scheme is presented. In chapter 5.4 the proposed CB selection algorithm is explained. Chapter 5.5 presents the test-bed set up subsequently, the experimental analysis discussed in chapter 5.6. Finally, chapter 5.7 concludes the chapter.

5.3 System Framework

This subchapter provides the technical details of the proposed RIS assisted wireless communication system setup. First, the system and signal model is presented followed by the setup of the experimental test-bed.

5.3.1 System Model

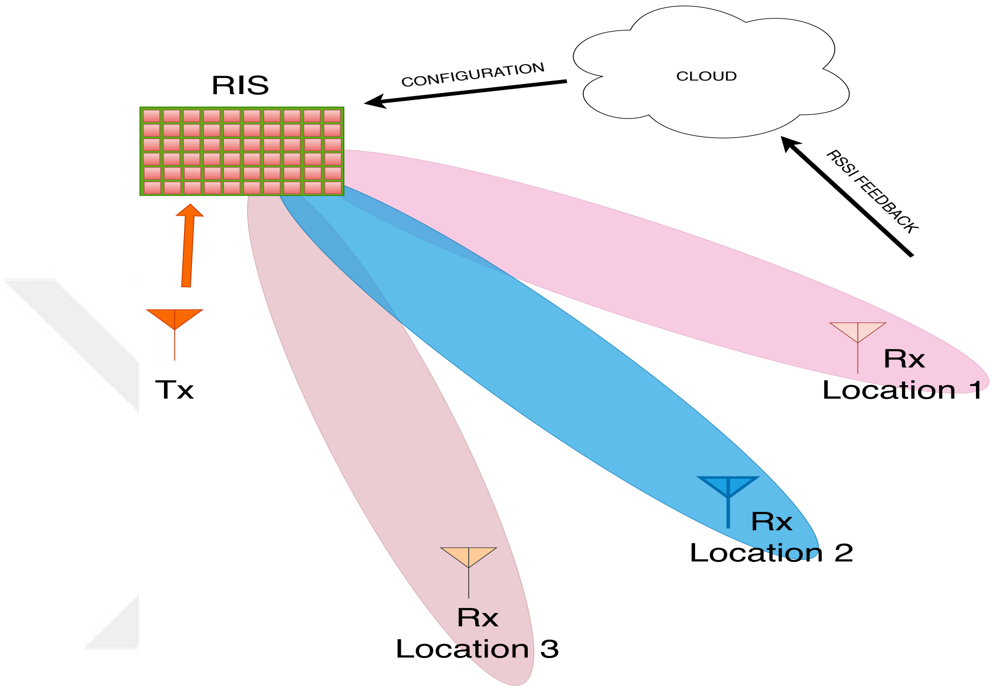

Figure 5.1: System design of the considered scenario.

In this study, communication occurs between a single-antenna Tx and Rx under the aid of a passive RIS with $N = C \times R$ electromagnetic elements, where C and R denotes the number of columns and rows of the RIS, respectively. Each individual element of the RIS has the ability to introduce $0°$ or $180°$ phase shifts in both horizontal and vertical polarizations, corresponding to off and on states, to the incident signal from the Tx. Since an RIS is employed generally in weak LOS or NLOS systems, we also consider a NLOS system where the channel from the Tx to the RIS is defined as $\mathbf{h} \in \mathbb{C}^{N \times 1}$ and the channel from the RIS to the Rx is defined as $\mathbf{g} \in \mathbb{C}^{N \times 1}$. As illustrated in Fig. 5.1, the RIS serves the receiving user from multiple locations depending on the users preference and selection from his/her application or remote control. The k^{th} complex baseband signal transmitted by the Tx is defined as $x[k]$ hence, and the received signal $r[k]$ can be expressed as follows:

$$r[k] = (\mathbf{g}^{\mathrm{T}}\mathbf{\Phi}_{\mathrm{RIS}}\mathbf{h})x[k] + n[k] \tag{5.1}$$

where $\mathbf{\Phi}_{\mathrm{RIS}} = \mathrm{diag}(\alpha_1 e^{j\phi_1}, \cdots, \alpha_N e^{j\phi_N})$ denotes the phase matrix at the RIS and $n[k]$ represents the additive white Gaussian noise (AWGN) component at the receiver caused by hardware components, which follows the distribution $\mathcal{CN}(0, \sigma_n^2)$. In the RIS phase matrix or in other words the CB, α_n, is the magnitude of the reflection coefficient of the n^{th} RIS element and is constant for a passive RIS, whereas the phase introduced by the n^{th} RIS element is ϕ_n and can take the values 0° and 180°, for $n \in \{1, \cdots, N\}$.

RISs are typically used to significantly improve coverage and the signal-to-noise ratio at the Rx by either eliminating interference, coherently aligning phases, or other novel methods by manipulating the channel. By adjusting the RIS CB $\mathbf{\Phi}_{\mathrm{RIS}}$, we can increase the end-to-end gain $|\mathbf{g}^{\mathrm{T}}\mathbf{\Phi}_{\mathrm{RIS}}\mathbf{h}|^2$ thus proportionally increasing the SNR of the received signal. The optimal CB that maximizes the gain is expressed as follows:

$$\begin{aligned} {\mathbf{\Phi}_{\mathrm{RIS}}}^* =_{\phi_n, \forall_n} \quad & |\mathbf{g}^{\mathrm{T}}\mathbf{\Phi}_{\mathrm{RIS}}\mathbf{h}|^2 \\ \text{s.t.} \quad & \phi_n \in \{0, 180\}, \forall_n. \end{aligned} \tag{5.2}$$

To solve this optimization problem, most studies conduct statistical channel estimation methods, however, we avoid complex techniques to obtain CSI and aim for low complexity for practicality. Another approach is to perform a heuristic search for the optimum CB that maximizes the gain. Since each individual element can be configured on and off in both polarizations resulting in four possible states, the search space is 4^N. Since N is a large number or RIS elements, 4^N is a very large search space and searching it iteratively would increase the complexity of the system, we need an algorithm do search this space as fast and efficient as possible without degrading performance significantly. Hence, in the next subchapter, we will propose a novel CB algorithm to search this space efficiently and even enhance the performance.

In the proposed system, we focus on maximizing the received power at the end user based on the maximization problem as provided in (2). Optimization of the CB that directs the incident signal from the Tx to the Rx and provides maximum received signal power in a fast, efficient and practical way is prioritized.

5.4 Proposed Codebook Algorithm

In this subchapter, the proposed CB algorithm is introduced and discussed in detail. Generally, CB search algorithms or methods in existing RIS literature depend on offline training, iterative and complex solutions. The focus of the proposed CB design is to provide a low-complex, fast and practical CB construction based on RSSI feedback from the user-end device. In [Kayraklık et al., 2022], the authors turn the RIS elements on and off one by one and decide to keep the RIS element on or off based on the RSSI feedback. Although this method provides decent performance, it needs to be done iteratively at each location in an offline manner and if a user falls in between these trained points, performance will degrade significantly when in online use. On the other hand, the authors from [Pei et al., 2021b] propose a low complexity algorithm doing a horizontal search first then on that trained CB, perform a vertical search on top of it. Though this is reduced in complexity, it is significantly degraded in performance and can be further enhanced without a drastic trade-off in the system performance. To introduce a more practical and efficient approach we consider the algorithm design presented in Algorithm 1.

In Algorithm 1, we first initialize CB instances $\mathbf{\Phi}_{\text{RIS}}$, $\mathbf{\Phi}_h$, $\mathbf{\Phi}_v$, and $\mathbf{\Phi}_{\text{temp}}$ by setting all elements to the off state and these RIS matrices denote the CBs for overall, horizontal, vertical and temporary configurations, respectively. The variables ${P_r}^0$, ${P_r}^{\max}$, and ${P_r}^{\text{c}}$ correspond to the initial, maximum and current RSSI values. First, we take RIS elements row by row and based on the RSSI feedback we decide whether the elements of that row should be on or off in between the Lines 6-17. The first for loop iterates over the elements in the same row, by applying $S = 4$ different states in Lines 6 and 7. $\mathbf{\Phi}_{\text{temp}}$ is updated such the sth state is applied to all elements on the rth row in Line 9. ${P_r}^{\text{c}}$ is updated based on the temporary CB, then if ${P_r}^{\text{c}}$

Algorithm 1 : Influential Element based Iterative Algorithm

Input: C, R, RSSI

$\mathbf{\Phi}_{\text{RIS}}, \mathbf{\Phi}_h, \mathbf{\Phi}_v, \mathbf{\Phi}_{\text{temp}} \leftarrow [0, \cdots, 0]$ *// Set all RIS elements to OFF state*

RSSI $\leftarrow {P_r}^0$ *// Measuring initial received power*

${P_r}^{\max} \leftarrow {P_r}^0$ *// Setting maximum power to initial power*

// Horizontal Search

for $r = 1 : R$ **do** *// Iterative Row Search*

    for $s = 1 : S$ **do**

        $\mathbf{\Phi}_{\text{temp}}[\phi_{r,1}, \cdots, \phi_{r,C}] \leftarrow S[s]$

        ${P_r}^{\text{c}} \leftarrow \text{RSSI}(\mathbf{\Phi}_{\text{temp}})$ *// RSSI feedback*

        if ${P_r}^{\text{c}} > {P_r}^{\max}$ **then**

            $\mathbf{\Phi}_{\text{h}} \leftarrow \mathbf{\Phi}_{\text{temp}}$

            ${P_r}^{\max} \leftarrow {P_r}^{\text{c}}$

        end if

    end for

    $\mathbf{\Phi}_{\text{temp}} \leftarrow \mathbf{\Phi}_{\text{h}}$

end for

return $\mathbf{\Phi}_{\text{h}}$

${P_r}^{\max} \leftarrow {P_r}^0$ *// Setting maximum power back to initial power*

$\mathbf{\Phi}_{\text{temp}} \leftarrow [0, \cdots, 0]$ *// Setting all RIS elements back to OFF state*

// Vertical Search

for $c = 1 : C$ **do** *// Iterative Column Search*

    for $s = 1 : S$ **do**

        $\mathbf{\Phi}_{\text{temp}}[\phi_{1,c}, \cdots, \phi_{R,c}] \leftarrow S[s]$

        ${P_r}^{\text{c}} \leftarrow \text{RSSI}(\mathbf{\Phi}_{\text{temp}})$ *// RSSI feedback*

        if ${P_r}^{\text{c}} > {P_r}^{\max}$ **then**

            $\mathbf{\Phi}_{\text{v}} \leftarrow \mathbf{\Phi}_{\text{temp}}$

            ${P_r}^{\max} \leftarrow {P_r}^{\text{c}}$

        end if

    end for

    $\mathbf{\Phi}_{\text{temp}} \leftarrow \mathbf{\Phi}_{\text{v}}$

end for

return $\mathbf{\Phi}_{\text{v}}$

$\mathbf{\Phi}_{\text{RIS}} \leftarrow \mathbf{\Phi}_{\text{h}} \bigcap \mathbf{\Phi}_{\text{v}}$ *// Set influential elements*

procedure ITERATION OVER REMAINING ELEMENTS

    ${P_r}^{\max} \leftarrow \text{RSSI}(\mathbf{\Phi}_{\text{RIS}})$ *// RSSI feedback*

    $\mathbf{\Phi}_{\text{temp}} \leftarrow \mathbf{\Phi}_{\text{RIS}}$

    for $j \in \mathbf{\Phi}_{\text{RIS}} \wedge j \notin (\mathbf{\Phi}_{\text{h}} \bigcap \mathbf{\Phi}_{\text{v}})$ **do**

        for $s = 1 : S$ **do**

            $\mathbf{\Phi}_{\text{temp}}[j] \leftarrow S[s]$

            ${P_r}^{\text{c}} \leftarrow \text{RSSI}(\mathbf{\Phi}_{\text{temp}})$ *// RSSI feedback*

            if ${P_r}^{\text{c}} > {P_r}^{\max}$ **then**

                $\mathbf{\Phi}_{\text{RIS}} \leftarrow \mathbf{\Phi}_{\text{temp}}$

                ${P_r}^{\max} \leftarrow {P_r}^{\text{c}}$

            end if

        end for

        $\mathbf{\Phi}_{\text{temp}} \leftarrow \mathbf{\Phi}_{\text{RIS}}$

    end for

    return $\mathbf{\Phi}_{\text{RIS}}$

end procedure

exceeds ${P_r}^{\max}$, it means that the applied states contribute to the overall system gain. Therefore, we update $\mathbf{\Phi}_h$ if a temporary CB is beneficial and update ${P_r}^{\max}$ accordingly in Lines 26-27. Finally, the best horizontal configuration is obtained and returned in Line 31. After resetting ${P_r}^{\max}$ to ${P_r}^0$ and $\mathbf{\Phi}_{\text{temp}}$ to fully off state, the vertical search is conducted by following the similar steps in between the Lines 21-32.

Then we look at both horizontal and vertical cases and select the elements that have the same state and identify the most influential elements, i.e., on/off in both horizontal and vertical cases. The most influential elements are decided by finding the intersecting elements with same states between $\mathbf{\Phi}_h$ and $\mathbf{\Phi}_v$ in Line 33. It should be noted that a significant amount of RIS elements overlap and are identified as influential elements and with the increase of these elements, the complexity decreases. In addition, as the RIS size increases the iterative method becomes more complex exponentially. However, in the proposed algorithm, as the RIS size increases or when polarization decreases and reduces the number of states possible, the number of influential elements will increase because more element states in the horizontal and vertical search will be the same. Hence, reducing complexity of the proposed algorithm even further. After deciding the most influential elements and setting their states for $\mathbf{\Phi}_{\text{RIS}}$, we start to build the states of the remaining elements in the procedure defined as in [Kayraklık et al., 2022] in Line 34. Since we are building the CB on top of the influential elements, ${P_r}^{\max}$ is set to RSSI value based on $\mathbf{\Phi}_{\text{RIS}}$. The loops in Line 37 and 38 iterates over the remaining elements one by one, by applying $S = 4$ different states. The search for the states of remaining elements is conducted by following the similar steps as explain in horizontal search, however this time the iteration goes over the remaining elements one by one in Line 37, by applying $S = 4$ different states in Line 38 rather than horizontal group of elements. Consequently, the final CB $\mathbf{\Phi}_{\text{RIS}}$ that maximizes the RSSI is returned.

While the benchmarks from [Kayraklık et al., 2022] and [Pei et al., 2021b] have a complexity of $\mathcal{O}(4 \times C \times R)$ and $\mathcal{O}(C + R)$, the proposed scheme has a complexity of $\mathcal{O}(C + R + 4 \times (C \times R - I))$ where $I = |\mathbf{\Phi}_h \cap \mathbf{\Phi}_v|$ is equal to number of influential elements. We propose a reduced complexity algorithm compared to the iterative method in [Kayraklık et al., 2022] while providing superior performance unlike [Pei et al., 2021b]. It should be noted that the proposed algorithm is less complex in cases where $I >> C + R$, which occurs most of the time. Furthermore, when the RIS size increases and a single polarization is considered, the likelihood of a lower complexity is guaranteed.

When the receiving user wants to set up a new CB, they can go to the desired location and quickly run this algorithm and save it on the RIS while online. Once a CB is saved, the user can just select that saved CB whenever they are at that location. There is no need for extensive offline training. Furthermore, the proposed CB takes into consideration of the impact of neighboring elements since we use a horizontal and vertical approach. Since we find the most significant elements and then do an iterative approach to the remainder of elements, the proposed CB algorithm not only provides low-complexity but also provides enhanced signal power hence, improved communication performance.

5.5 Test-Bed Set-Up

In this subchapter, we will discuss the set up of our system and details of the equipment used. Furthermore, the control mechanisim and end-to-end user experience process will be discussed.

Fig. 5.2 presents the general model of our set up for the experimental analysis. As seen in Fig. 5.2, the TX is a horn antenna with a half beamwidth of 40°, on the other hand for a practical approach, the receiver is equipped with an omni-directional antenna. While most literature consider specific geometric set-up cases such as L-shaped hallways [Kayraklık et al., 2022], we consider an indoor office environment where the RIS is mounted on a wall or the edge of the room and the end-user equipped with an omni-directional antenna is located at different desks which are positioned at various ends in the office considering numerous geometric and reflective scenarios. Through the aid of two ADALM-PLUTO software-defined radio (SDR) modules, the signal $x[k]$ is modulated with M-PSK and transmission

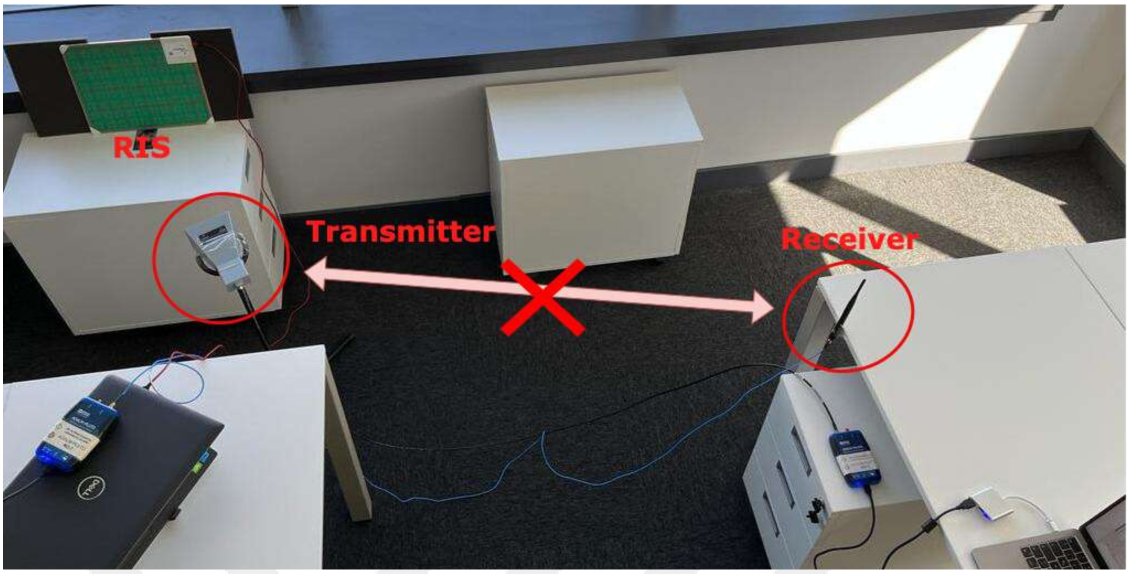

Figure 5.2: Test-bed set-up for the experimental analysis.

occurs at 5.2 GHz with −10 dBm power with a horn antenna directed towards the RIS to ensure no line-of-sight between the Tx and Rx, on the other hand, reception takes place in different locations of the office with an omni-directional antenna measuring the received signal power at 5.2 GHz. A 10×8 uniform planar array RIS prototype designed by Greenerwave [GW,] is exploited to redirect impinging signals towards the desired area via software-controlled phase shifts. Operating at a center frequency of 5.2 GHz and working bandwidth of 1 GHz, this RIS has 76 controllable elements via pin diodes, that have the ability to introduce 0° or 180° phase shifts in both the horizontal and vertical polarizations. Hence, the RIS consists of 4^{76} possible configurations resulting in a significantly inefficient exhaustive search algorithm [Popov, 2021].

In our system, the RIS is independent from the Tx and Rx and initially has all elements set to 0°. When the receiving user goes to a desired location and wants to run the proposed algorithm through the use of an app or remote control, the user selects a new configuration and requests to run the CB algorithm. When the CB algorithm is initiated, the RIS and receiver connects to the cloud/server. As the states of the RIS elements change and search for a new configuration, the server requests RSSI feedback from the receiver. Based on the request, the receiving device captures 50 frames and with 10^6 samples per frame and feedbacks the average RSSI value. Hence, the proposed algorithm quickly produces a sub-optimal CB for that location through the cloud and saves it at the RIS. The RIS then disconnects from the network and passively serves the user. This can be done for numerous locations which will be denoted as Loc A, Loc B, Loc C, and the CB for each location will be stored at the RIS. The user can delete or add new CBs as desired and through the use of the remote select whichever CB to apply at the RIS. Hence, the RIS is passive and isolated from the network and only connects to the cloud momentarily to run the practical and high performance CB generation algorithm when desired.

5.6 Experimental Analysis

In this subchapter, we present the experimental results and compare the performance of the proposed system with both benchmark 1 from [Kayraklık et al., 2022] and benchmark 2 from [Pei et al., 2021b] as mentioned in subchapter 5.4.

Fig. 5.3 displays the performance and complexity of the proposed system and benchmarks through the received signal power and number of iterations, respectively. As it can be deducted, the proposed CB algorithm presents a desirable outcome providing superior performance than both benchmarks. When compared to benchmark 1, the proposed algorithm exceeds in both complexity and performance. On the other hand, when compared to benchmark 2, the proposed system has higher complexity but is admirable in its superior performance. It should be noted that the proposed scheme doesn't start from a low received power due to the horizontal and vertical parts of the algorithm being run first, and increasing the received signal power by selection of the influential elements. Hence, an additional $(C+R)$ number of iterations are added to the complexity, however, it is still significantly less that benchmark 1.

Fig. 5.4 shows the CBs generated on the cloud and applied at the RIS. The black color indicates the controller part of the RIS which doesn't consist of reflecting RIS elements. In the configuration instances for each of the RIS elements, the dark

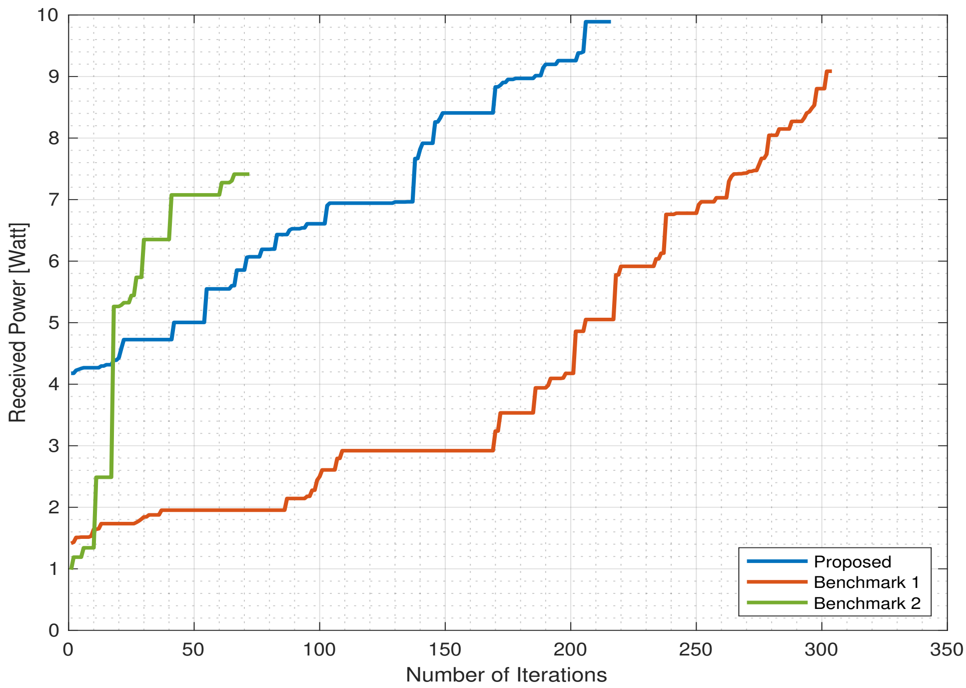

Figure 5.3: Performance comparison between the proposed CB algorithm and benchmarks.

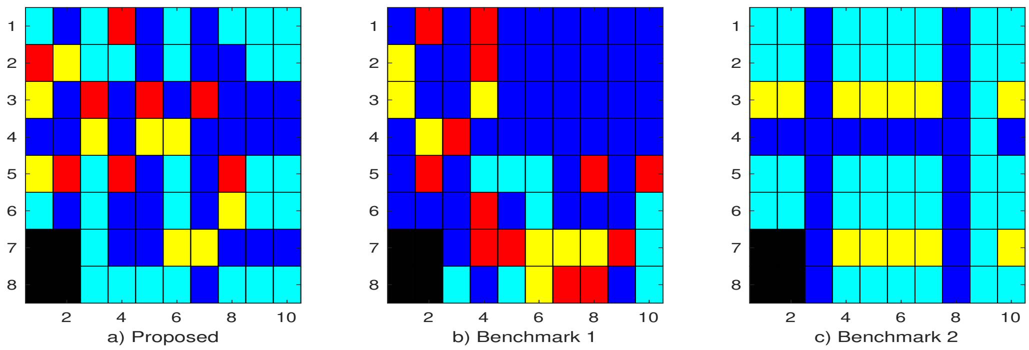

Figure 5.4: CBs generated from the proposed algorithm and benchmark algorithms.

blue color represents 0° state and the red color stands for the 180° state in both polarizations. The light blue color represents the 0° state for the horizontal and 180° state for the vertical polarizations. On the other hand, the yellow color represents the 180° state and 0° state for the horizontal and vertical polarizations, respectively.

In Fig. 5.5, we place the receiving user at three different locations and generate

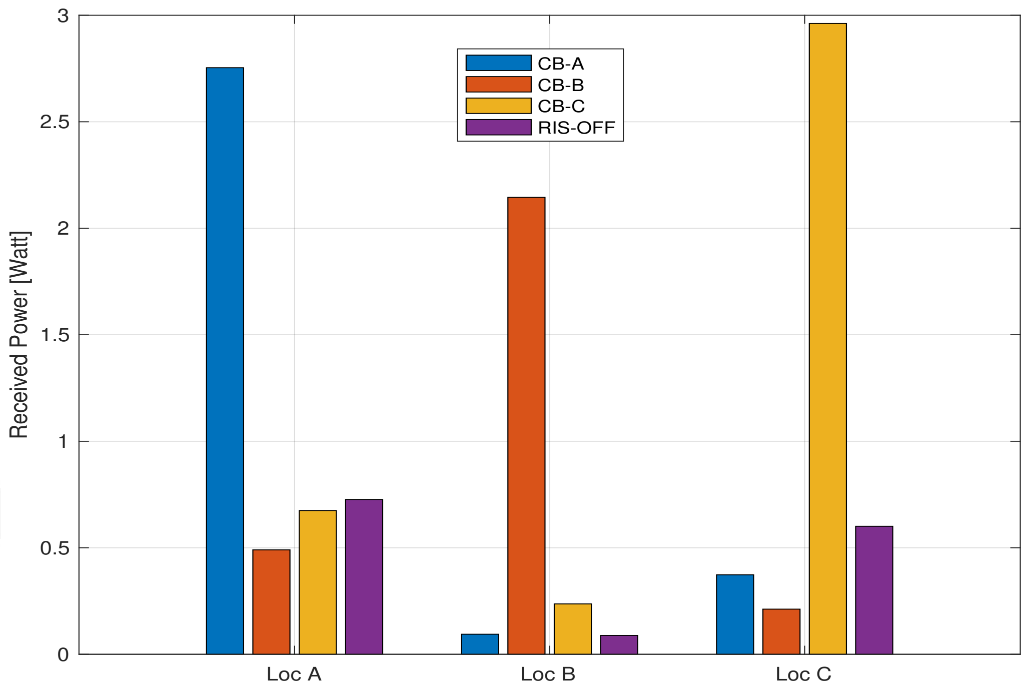

Figure 5.5: CB performances at varying locations.

a CB for each. These three locations are denoted by Loc A, Loc B and Loc C, and the configured and stored CBs for these locations are denoted by CB-A, CB-B and CB-C, respectively. Then the user moves to each location and all generated CBs are applied in succession and the performance in received signal power is measured. It can be observed that the CB generated for the corresponding location has a significant impact on the user performance while the other CBs generated at other locations in the office do not provide similar gains. This behaviour shows that the proposed CB algorithm works accurately and stored CBs perform based on the user selected location.

5.7 Chapter Summary

In this chapter, a unique and practical user-controlled RIS system has been considered. In addition, we have proposed a novel, practical and efficient CB algorithm while reducing the complexity and also enhancing the performance of the RIS aided system. Extensive experimental results have been demonstrated, discussed and confirm the performance enhancement along with the practicality of the system design. Future directions may include applications of machine learning the further improve performance and complexity of the proposed system design.

Chapter 6

RECONFIGURABLE INTELLIGENT SURFACE IDENTIFICATION IN MOBILE NETWORKS: OPPORTUNITIES AND CHALLENGES

6.1 Preface

The advent of the sixth generation (6G) wireless networks heralds a transformative era for mobile communication, where the integration of cutting-edge technologies like Reconfigurable Intelligent Surfaces (RISs) is paramount in addressing the burgeoning demands for energy efficiency, high data rates, reliable connectivity, and enhanced coverage in densely populated areas. RISs have attracted the attention of academia as well as the industry and emerged as a beacon of innovation, offering a novel paradigm to reconfigure the wireless propagation environment beneficially, thereby enhancing the overall network performance. It is envisioned that the deployment of numerous RISs in a mobile network will serve user equipments (UEs) to boost various key performance indicators (KPIs), with lower energy consumption compared to alternative solutions (e.g., relays, and network-controlled repeaters). However, the knowledge of whether or not a UE is being served through an RIS and if so, which RIS it is being served by is crucial and beneficial for various network planning and operational reasons. In this chapter, we address the importance and the benefits of RIS identification in a mobile network. Additionally, we guide the readers and researchers by introducing alternative methods to enable RIS identification. Through the lens of this research, we unveil and shed light to various benefits, the challenges, and future opportunities in the identification of RISs serving mobile users in complex network environments, highlighting the necessity for advanced identification strategies to fully harness the potential of RIS technology in next-generation wireless systems.

6.2 Introduction

Advancing into the future, sixth-generation (6G) wireless networks are poised to revolutionize communication technologies with their promise of terabit-per-second speeds, enhanced privacy, virtually zero latency and ultra-reliability even in densely populated areas. Numerous unique technologies and their coexistence such as novel waveform designs, multiple access techniques, reflective metasurfaces, machine learning (ML), and more are investigated and developed to realize these 6G goals. One critical technology for future wireless networks is the integration and deployment of reconfigurable intelligent surfaces (RISs) [Wu and Zhang, 2020]. Gaining popularity for their ability to control and optimize the wireless propagation environment, RISs consist of programmable elements that can dynamically alter the phase, amplitude, and polarization of the incoming electromagnetic waves [Basharat et al., 2021]. RIS technology offers substantial benefits in terms of network coverage, signal strength, and data secrecy, improving the overall user experience, as well as system capacity and energy efficiency. On the other hand, there are many practical concerns awaiting solutions regarding the installation, integration, and management of RIS equipment [Arslan et al., 2023b]. Among these, the main challenges might be listed as

- Clarifying practical deployment benefits and drawbacks compared to previous network equipment like network controlled repeaters (NCRs) and radio frequency (RF) repeaters,[Ayoubi et al., 2023],
- Ensuring effective coordination during operation (control by base stations (BS), RIS itself, or user equipment (UE)),
- Developing optimization algorithms for RIS configuration with or without cascaded channel state information (CSI).

Despite these hurdles, RIS stands as a cornerstone technology for 6G, promising to transform wireless communications by enabling smarter and more efficient network behaviors [ETSI, 2023, Basar et al., 2023].

RIS is envisioned for deployment by operators in various environments, from urban centers to rural areas, enabling networks to overcome physical obstructions and distance limitations. RIS will be useful in many indoor/outdoor applications, such as optimizing signal distribution in large public venues and enhancing communication reliability in emergency response scenarios. This strategic deployment enhances 6G network capacity and efficiency, paving the way for innovative services leveraging robust connectivity [Ren et al., 2023]. Additionally, RIS serves as an anchor for integrated sensing and communication (ISAC) applications [Yu et al., 2024], enhancing their diversity and accuracy, making RIS a versatile asset for 6G technology.

With the deployment of RIS, identifying which RIS a UE interacts with is critical [Khaleel et al., 2024]. RIS identification, determining which RIS is affecting a user's signal, is vital for optimizing real-time communication, enhancing signal quality, network coverage, capacity, security, and localization accuracy. It also plays a crucial role in network planning, interference management, handover, and roaming. Accurate RIS identification can significantly improve key performance indicators (KPIs) such as throughput, security, reliability, energy efficiency, and localization in 6G networks. However, this requires sophisticated detection and communication protocols to ensure accurate RIS recognition, especially in environments with multiple RISs.

Despite its importance, the domain of RIS identification remains mainly underexplored. Most existing research focuses predominantly on the design and optimization of RISs without adequately addressing the challenges associated with their discovery and (mis)identification in an operational network. Identifying an RIS involves determining not just its presence but also its specific influence on the signal path, a task complicated by the passive nature of most RIS implementations and the subtle variations in the signal characteristics they induce. As of now, the identification of RISs in wireless networks remains largely underdeveloped, primarily due to their passive nature. Unlike active network components such as BSs and repeaters, which identify themselves through broadcasts like service set identifiers (SSIDs), RISs do not inherently transmit any identification signals. Current approaches proposed for active network components might leverage signal strength measurements, timing advances, or complex CSI, which can be cumbersome and imprecise, particularly in dynamic and cluttered environments. This challenge introduced by the passive nature of RIS necessitates innovative approaches to it's identification, borrowing concepts from technologies like RF identification (RFID) and near-field communication (NFC), which rely on distinct signals to recognize tags or devices.

Inspired by the potential and popularity of RIS-empowered systems resonated in academia and industry to realize smart wireless environments, this chapter provides a unified RIS identification framework and a thorough exploration of the identification process, presenting its fundamental principles and explaining the substantial advantages it offers to wireless communication networks. Our comprehensive discussion aims to clarify the operational impact and strategic importance of accurate RIS identification. We introduce three promising research directions and preliminary techniques for realizing RIS identification in wireless networks in different domains each with various issues and considerations. Our discussion is extended with a critical examination of the prevailing issues and challenges inherent in RIS identification. Furthermore, we propose potential strategies and future research avenues, which are crucial for providing a deeper and insightful perspective on the practical evaluation of RIS-assisted wireless networks.

The remainder of this article is organized as follows. Chapter 6.3 discusses RIS identification in a mobile network and the benefits it brings. Chapter 6.4 then introduces some preliminary RIS identification techniques considering different domains to provide insight and trigger future alternative solutions. Chapter 6.5 highlights and outlines some of the research challenges which may need to also be considered when performing RIS identification. Finally, the article is concluded in chapter 6.6.

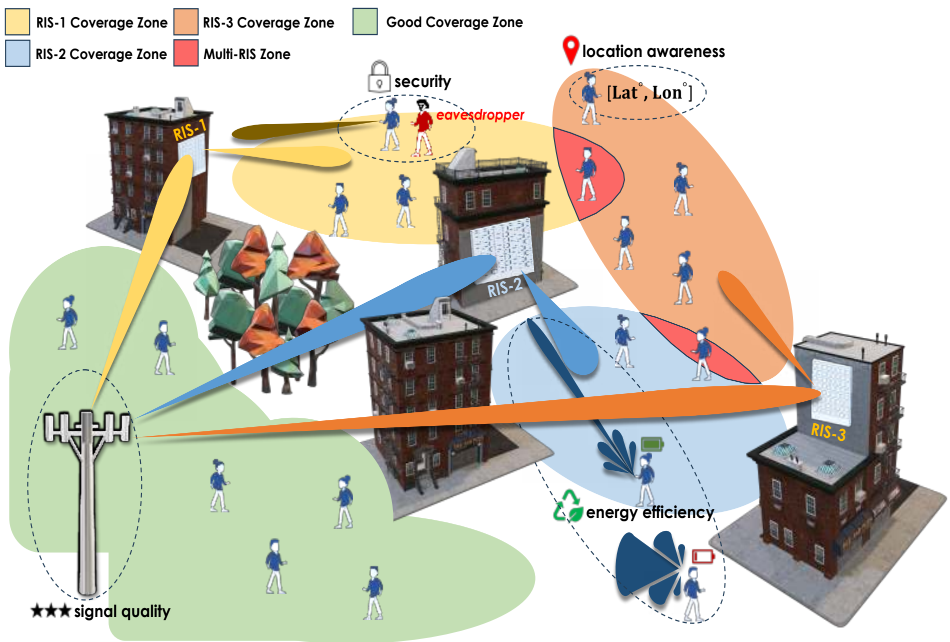

Figure 6.1: Representative sketch for a densely populated cellular environment utilizing multiple RISs

6.3 RIS Identification

In the intricate urban tapestry where skyscrapers and concrete establishments disrupt direct communication pathways, RIS-empowered communication emerges as an enabling technology for enhanced connectivity. The urban scenario depicted in the Fig. 6.1 is representative of modern cities where dead zones with poor signal quality are commonplace. In such zones, the direct line-of-sight (LoS) to the BS is often obstructed, leading to deteriorated communication performance, especially for higher frequency bands established by 5G and beyond. Deploying RISs within these areas is a strategic move to mitigate such connectivity challenges, with each RIS assigned a unique identification code, enabling not just signal reflection and refraction but also intelligent environment-aware signal enhancement.

RIS identification becomes paramount when a user's device enters such a zone and should first detect if it is being served by an RIS or not. Beyond mere detection, the device must ascertain the specific RIS from which it is receiving the signal. This identification process is crucial as it provides many benefits with the identification information and determines the quality of service the UEs experiences, which will be discussed in the following subchapters. However, there could be scenarios where the UE is in the coverage of multiple RISs so called multi-RIS zones. These are regions where the coverage zones of multiple RISs overlap. In these areas, the signals from different RISs might intermingle, similar to inter-cell interference, leading to a scenario where the UE device may struggle to discern which RIS it is interacting with. This confusion may cause the device to either oscillate between RISs or, worse, connect to an RIS with a weaker signal or poorer performance relative to its position. Hence, RIS identification can aid in detecting whether a UE is served by a RIS and also in distinguishing which RIS it is served by when in a multi-RIS zone.

RIS identification thus entails an approach where the UE must employ algorithms capable of distinguishing signals and RIS IDs based on their unique BS or RIS-induced modifications. This may involve detecting subtle differences in signal phase, power, polarization, or timing introduced by the BS or RIS's reflective properties which are detectable by receiving devices to identify the specific RIS. On the BS side, techniques may focus on marking signals transmitted over the RIS prior to transmission to indicate which surface is in use, offering centralized control that simplifies system management. Conversely, RIS-based identification methods rely on receivers recognizing specific signal alterations, such as changes in phase or amplitude, to identify RIS engagement. This allows for distributed processing, enhancing scalability in dense networks but increasing demands on receiver sensitivity and complexity. Both strategies strive to optimize identification precision and overall network performance, presenting unique benefits and considerations for varying environments.

For beyond-5G era, the integration of RISs is anticipated to adhere to stringent standards that ensure seamless operability, optimally-mitigated interference, and maximal efficacy within the network. The RIS identification process is thereby not only a question of signal discernment but also one of compliance with the protocols and their requirements set forth by these advanced communication standards, requiring solutions that integrate effectively with the dynamic nature of 6G networks while maintaining scalability and efficiency.

RIS identification techniques may assist in detecting multiple RISs and in such a scenario choosing the RIS that provides optimal performance. In the context of 5G networks, by identifying the correct RIS, a UE can optimize its connection to exploit a wider range of 5G's capabilities, such as high data rates, higher efficiency, improved reliability, and reduced latency by directing its beam towards the dedicated RIS.

In dense urban environments, RIS technology enables networks to proactively address the diverse demands of modern wireless communication. The convergence of RIS with 5G standards represents the future, where devices actively participate in a coordinated flow of data, guided by RISs. Detailed information on beneficial use cases for RIS identification in beyond 5G wireless communications is provided in the following subchapters.

6.3.1 Signal Quality Enhancement

RIS identification directly enhances signal quality by optimizing the communication path between the UE and BS. When the UE identifies the connected RIS, it can improve uplink communication by targeting transmissions toward the RIS, boosting connection quality and bandwidth efficiency. This approach reduces signal degradation, essential for high-demand applications. Additionally, UEs can adjust settings like transmission power and beam direction based on the identified RIS, addressing signal strength and interference. Moreover, RIS identification may aid in congested network environments, through dynamically redistributing network load or enhancing signal fidelity for users in high-density areas, leading to a more balanced and effective network performance.

6.3.2 Optimized Security and Secrecy

In wireless communications, RISs have revolutionized not only signal optimization but also security and secrecy [Yang et al., 2020a]. Identifying the specific RIS serving a UE can enhance security by enabling dynamic adaptation to threats and securing sensitive services like e-commerce and data exchange. For instance, in a military base or government facility, where highly confidential communications are transmitted, RIS identification allows the network to activate advanced encryption protocols and authentication based on the specific RIS connection. This ensures that only authorized devices within a particular coverage zone can access the network, reducing the risk of unauthorized access or eavesdropping. Moreover, adapting spatial domain characteristics of the UE such as Tx and Rx beams in the direction of the identified RIS, may help in isolating the communication path which minimizes the chance of interception safeguarding the legitimate data transmission. The ability of RIS to manipulate signal phases and amplitudes adds another layer of physical-layer security, making it difficult for eavesdroppers to decode the signal, providing a proactive and robust security mechanism for critical communications.

Moreover, the unique ability of RIS to manipulate signal phases and amplitudes adds a layer of physical layer security, concealing communications from eavesdroppers and representing a significant step toward proactive security measures in wireless networks [Zhang et al., 2021c, Yang et al., 2020b].

6.3.3 Energy Efficiency

The integration of RIS in mobile networks can significantly enhance energy efficiency through precise RIS identification and interaction. As illustrated in Fig. 1, when the UE identifies the serving RIS, it can perform directed beamforming, focusing energy on efficient paths rather than relying on less effective non-line-of-sight (NLOS) or omnidirectional transmissions, reducing power wastage. Devices can adjust power output based on RIS coverage, conserving battery life and maintaining service quality, especially critical in mobile environments. For example, in dense environments with numerous UEs in a RIS aided zone, this is especially important when considering the overall energy savings. RIS identification also facilitates network-wide energy management, allowing operators to track frequently used RISs, allocate resources more effectively, and activate RIS panels only when needed, leading to overall enhanced network efficiency and contributing to sustainability goals.

6.3.4 Localization and Sensing

One major benefit of RIS identification complementary to the 6G vision is the enhancement of localization in wireless networks by enabling UEs to determine their location based on the specific RIS connected to. This process allows for a granular level of location awareness, beneficial in environments where traditional GPS struggles, such as densely built-up urban areas or large and complex indoor spaces like malls and airports. In conventional systems, three anchor points are needed for localization methods like time difference of arrival and time of arrival. With RISs serving as additional anchor points, a single gNB can localize UEs by creating extra paths. UEs must identify the paths and signals from RISs for triangulation, but since RISs are passive, UEs need to detect and be aware of their role in the process. Once a UE identifies the RIS and obtains its location, it can calculate its own position based on signals from the RIS. Even identifying a single RIS can offer granular location awareness.

For example, by identifying the RIS that assists the nearby region, a UE can ascertain that it is within a particular zone of a shopping center, enabling tailored navigation services and location-specific information such as store promotions or directory assistance. This identification can also streamline emergency responses; when a user can pinpoint and communicate their location via the connected RIS, emergency services can rapidly locate and reach the individual, reducing response times and potentially saving lives in case of disasters and possible casualties. As illustrated in Fig. 6.1, when the user served by RIS 3 identifies the RIS, it can obtain rough information that it is in the orange coverage area and have location awareness. This personalization improves user engagement and creates opportunities for innovative services across various sectors, positioning RIS identification as a key element in next-generation wireless systems.

6.3.5 Smarter Interference Management

Intelligent interference management, enabled by accurate RIS identification, allows users to actively participate in optimizing network performance. By recognizing the

Table 6.1: Comparison of Proposed Identification Techniques

Method	Domain	Complexity	Precision/Robustness	Waveform
Amplitude Modulation Sequence	Time	Low	Low	Single-/Multi-carrier
Spectral Fingerprinting	Frequency	Moderate	Moderate	Multi-carrier
BS Side Watermarking	Code and Spatial	High	High	Single-/Multi-carrier

serving RIS, devices can dynamically adjust their transmission and reception parameters, such as power levels and beam directions, to minimize inter-cell interference observed in legacy time-division duplexing (TDD) and user-to-user cross-link interference observed in dynamic TDD and next generation sub-band full duplex technologies [3GP, 2024]. Spatial domain techniques play a pivotal role in mitigating interference, as discussed in RAN1 and 3GPP meetings [3GP, 2024]. This real-time adaptation is crucial in environments with multiple RISs, where the potential for signal conflict is high in multi-RIS zones. However, targeted communication towards the identified RIS reduces unnecessary signal spread, avoiding interference with other users in the vicinity. This approach not only improves the individual user experience by ensuring more reliable connections but also enhances the overall network efficiency by reducing cross-interference among users connected to adjacent RISs.

6.4 RIS Identification Techniques

This subchapter briefly introduces preliminary and pioneering identification approaches for RISs in wireless networks in successive subchapters. The following proposed identification methods are briefly summarized in Table I.

6.4.1 Amplitude Modulation Sequence

The principle behind this technique involves the alteration of the impinging signal's amplitude by the RIS to embed a recognizable pattern. Specifically, the RIS can selectively boost or attenuate the signal's strength by either coherently and destructively manipulating the phases of its elements or switching off a subset of its elements at predetermined intervals, thereby reducing the signal reflection or redirection during those periods. This creates a signature in the signal's amplitude that can be detected and decoded by the receiver. This can be applied to both single-carrier and multi-carrier systems.

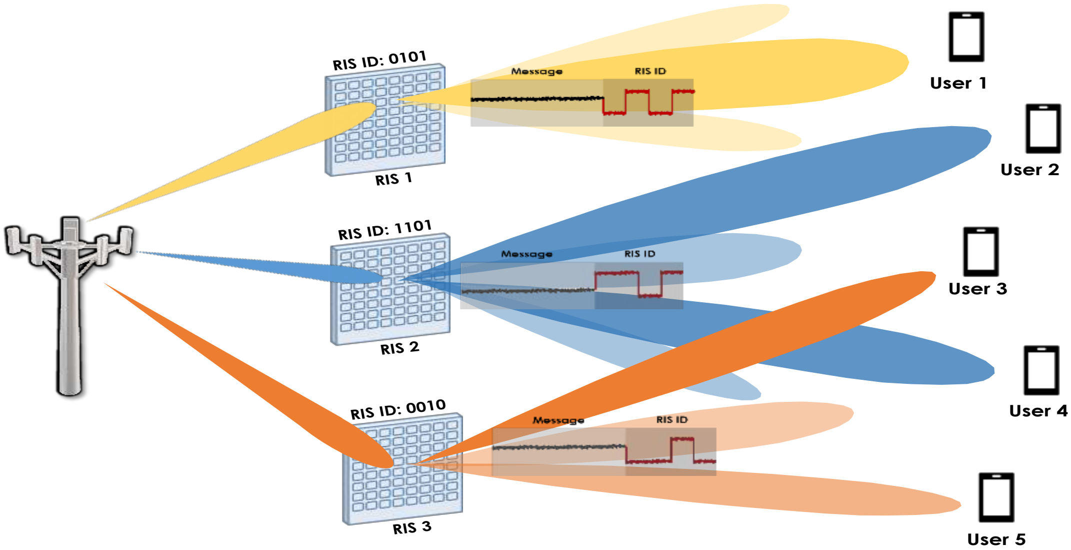

Figure 6.2: Illustration of amplitude modulation sequence technique for RIS identification.

Fig. 6.2 illustrates this concept by depicting multiple RIS units, each modulating the signal's amplitude in a distinct manner, creating identifiable power variations at UEs' receivers. These variations are encoded into the signal as unique identifiers, enabling each UE to discern and authenticate the RIS in communication, thereby ensuring a secure and efficient network operation.

6.4.2 Spectral Fingerprinting

The spectral fingerprinting method leverages the frequency domain characteristics of a multi-carrier signal. The RISs can strategically adjust themselves according to the channels of certain subcarriers and boost them. Doing so, each RIS imprints a distinct spectral signature on the signal that can be easily distinguished

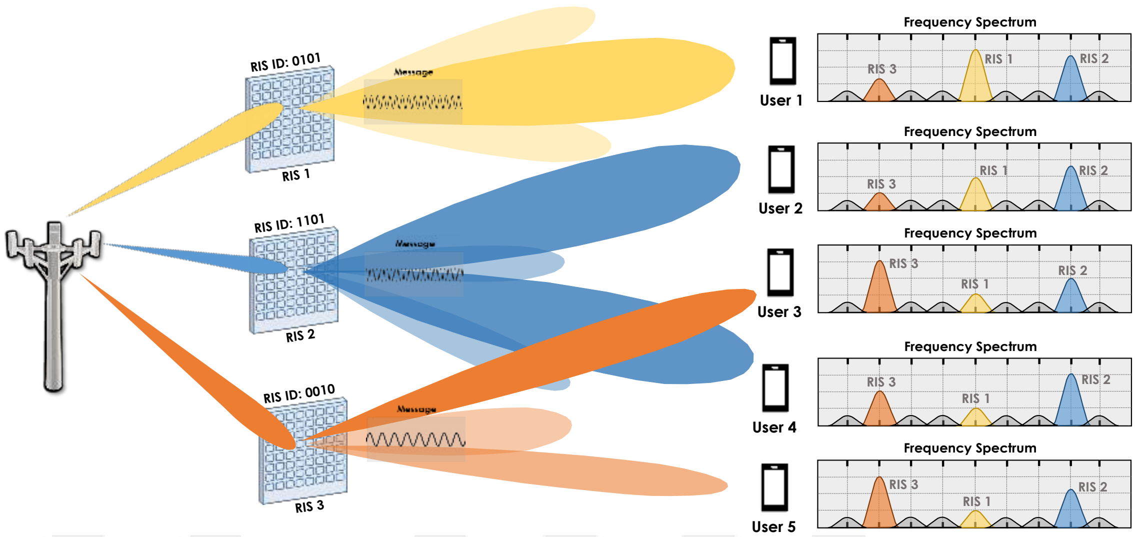

Figure 6.3: Illustration of spectral fingerprinting technique for RIS identification

at the receiver with subcarriers' orthogonality. Fig. 6.3, shows the power distribution across subcarriers is noticeably altered at each UE after the reception of all existing RIS-assisted signals. Based on the the instant location of the UEs and the existing RISs, the frequency spectrum given for each UE includes information about the existing RISs' dominance. The peaks corresponding to the intensity of RIS signatures help determine and manage the supporting RISs for each UE. The presence of distinct peaks correlates to the respective RISs active during transmission. Through careful analysis of these power distributions, the UE can discern which RISs have been engaged and infer their relative efficacy and proximity. This approach might momentarily face misidentifications due to spectral notches that can occur in frequency-selective propagation environments, hence parameters such as number of symbols to consider for the identification process, bandwidth and size of subcarrier grouping for spectral fingerprinting may be considered to increase robustness of the system.

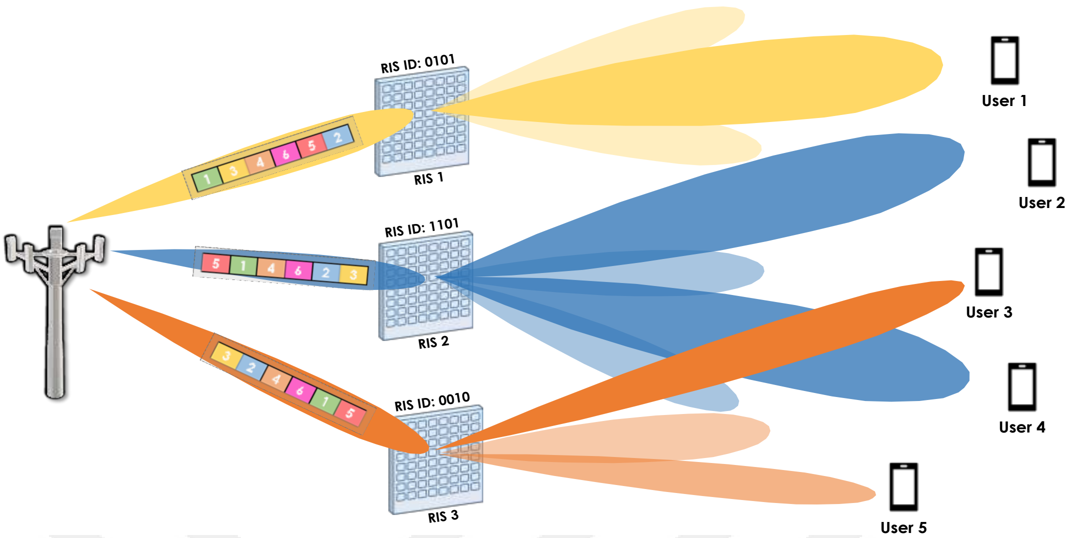

Figure 6.4: Illustration of BS watermarking technique for RIS identification.

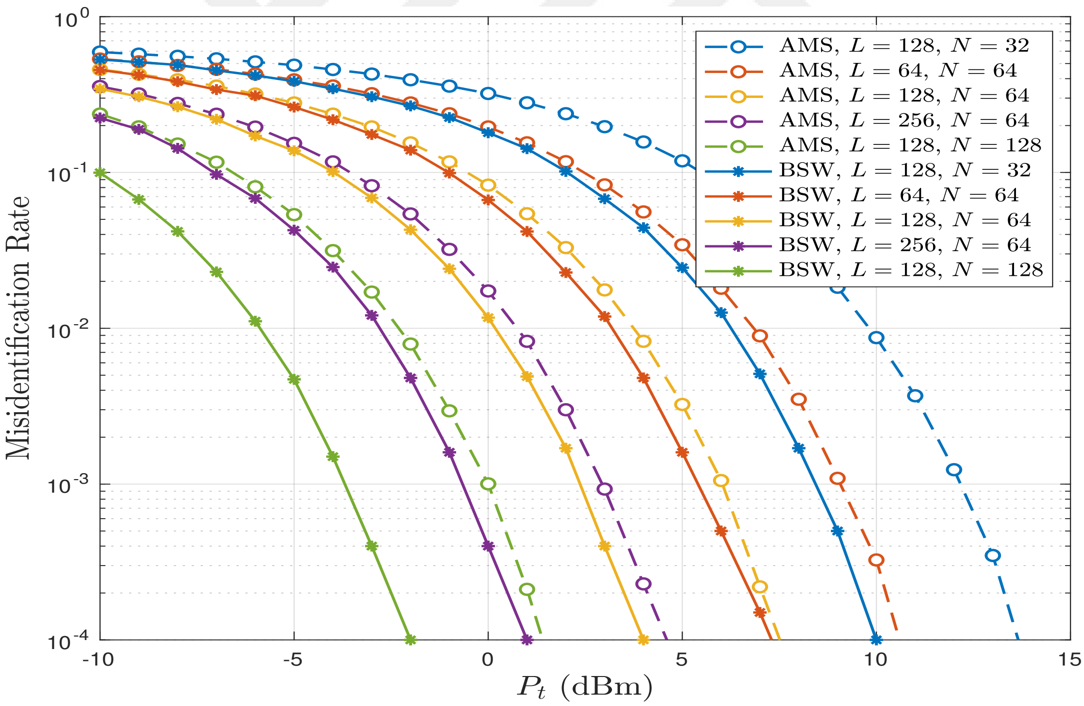

Figure 6.5: Identification Performance of BS watermarking technique (BSW) and amplitude modulation sequence (AMS) for varying codelength (L) and RIS size (N).

6.4.3 BS Watermarking

This core concept revolves around the BS embedding a unique identification sequence within the single or multi-carrier signals directed towards the various RISs, as depicted in the Fig. 6.4. The BS crafts these signals, x_1, x_2, and x_3, with distinct characteristics, akin to a digital watermark. This could be a set of orthogonal codes, cyclic shifts, or specific phase shifts, each serving as a beacon for the UE to recognize the signal's origin and path. Such distinct modifications are not merely arbitrary; they are meticulously designed sequences with exceptional auto-correlation and poor cross-correlation properties, ensuring minimal interference and optimal path discernment by the UE. When the BS broadcasts these signals, the UE's task is to correlate the received sequences and pinpoint the exact RIS through which the signal was reflected. This is similar to a detective matching fingerprints at a crime scene, each unique sequence leads back to a specific RIS, allowing the UE to 'localize' its communication pathway.

Fig. 6.4 illustrates this concept where the BS is the signal origin, with each RIS reflecting these signals to the UE. The unique identification sequences encoded within the signals are the critical factor enabling each UE to discern and trace the signal path back to its RIS of origin. The type and length of the sequences are important when designing such a system.

6.4.4 Performance Considerations

In this subchapter, performance insights are provided for the proposed techniques and discuss the various factors and parameters that can affect the system performance, as each operates in distinct domains and scenarios.

The misidentification rate for all methods can be assessed through computer simulations by adjusting transmit power. Increasing the RIS size (N) generally improves identification accuracy across methods. However, for the amplitude modulation sequence method, longer sequences within a fixed identification period degrade performance due to shorter power level changes. This requires finer detection and increases sensitivity to errors and environmental fluctuations. Additionally, increasing the difference between high and low power levels improves reliability, though environmental factors including selective fading and mobility still play a critical role.

In the spectral fingerprinting method, performance is influenced by the subblock size. Smaller subblocks require higher receiver sensitivity, and in frequency-flat channels, increased correlation between subcarriers can degrade identification accuracy. Boosting specific subblocks may unintentionally enhance correlated subblocks, complicating RIS alignment, especially in low-slectivity channels where resolving taps in the power delay profile is difficult. For a fixed spectrum size, as the number of RISs increases, the subblock size decreases, leading to higher misidentification rates.

Among the three, the BS watermarking method offers the greatest scalability. It efficiently manages numerous RIS deployments by assigning unique codes to each RIS, eliminating the need for extensive time resources or larger spectrum allocations. This approach closely mirrors the BS identification process currently used in 5G NR standards [Dwivedi et al., 2021]. Fig. 6.5 presents simulation results showing the impact of system parameters on BS watermarking identification and amplitude modulation sequence performance. The simulation involves three RISs with varying element counts (N), where the BS communicates with the UE via RISs in a single carrier system. The BS, RISs, and UE are positioned on a coordinate plane, with Gold sequences and QPSK modulation used in a Rayleigh fading channel. The UE receives signals from all RISs, with RIS 2 as the primary. The results show the BS watermarking method outperforms the amplitude modulation sequence method due to better cross-correlation properties. Furthermore, it can be concluded that increasing code length (L) and N improves identification performance by reducing the misidentification rate. It should be noted that these are initial simulations results to show a general behaviour; the optimization and enhancement of the system is an important research problem.

6.5 Future Directions and Open Challenges

As wireless networks evolve, the expected density and scalability of RIS deployment are expected to significantly increase [202, 2023]. Managing and identifying a large number of RIS panels, especially in dense urban environments or large indoor spaces, poses a substantial challenge. Ensuring that each RIS can be uniquely identified without creating an overly complex or resource-intensive process is crucial. It is imperative to address the mechanics of the identification process, its timing, and the strategic implementation to ensure seamless network integration and optimal performance. The following subchapters introduce some prominent future directions and open challenges regarding the identification of RISs.

6.5.1 Identification Period

Determining the optimal identification period, or time allocated for a device to identify the RIS, is crucial for supporting various operational requirements and balancing identification reliability with overhead. The decision to implement a distinct identification period requires careful consideration of its benefits and drawbacks, as well as exploring alternatives for seamless integration without sacrificing performance. RIS identification can be done with a dedicated period or simultaneously with data transmission. A dedicated period allows for focused assessment of signal characteristics and the RIS's impact, leading to better decisions on beamforming, power allocation, and adaptive mechanisms. However, it consumes valuable time that could be used for data transmission, especially during high-demand scenarios, potentially increasing latency and reducing throughput. The dynamic nature of mobile environments means the optimal identification period may vary, requiring adaptive strategies that complicate network management.

6.5.2 Misidentification

When a device erroneously identifies a non-serving RIS as its source of signal enhancement, the primary concern is the potential for reduced user and network performance. This is particularly problematic in border areas between RIS zones called multi-RIS zones, where signals from adjacent RISs might overlap. In such cases, a device might receive conflicting signal enhancements, leading to a degradation in signal quality and overall communication reliability. Moreover, false RIS detection can result in suboptimal resource allocation, where network resources are wasted on attempting to optimize a connection with an incorrect RIS, thereby reducing the network's overall efficiency. Some strategies such as enhanced signal processing techniques to distinguish reflected signals, strategically planning the deployment of RISs in a network to mitigate the risk of false detection and/or misidentification, ML-based solutions, and user feedback mechanisms may aid and are future directions in the misidentification problem.

6.5.3 Optimal Identification Domain and Technique

The choice of domain for RIS identification significantly influences the system's efficiency and reliability. Time-domain identification may occur simultaneously with data transmission; however, this may compromise the reliability of the transmitted data. Specific time slots could be considered to transmit RIS IDs, requiring a dedicated identification period, but in this case communication and RIS identification cannot be done simultaneously potentially impacting data throughput due to the allocation of resources for identification purposes. Altering the signal power in time domain could vary the power levels to encode RIS IDs, posing challenges in dynamic environments where signal strength can fluctuate due to mobility or obstacles. This method can be considered in single and multicarrier systems; however, the time variability in multicarrier systems may be a disadvantage making the distinguishability of the signal power variation performed by the RIS an issue, whereas single carrier is more deterministic in time resulting in a more robust option. While the receiver detector is simple, focusing on time and power, its effectiveness decreases in dynamic environments. This method is sensitive to fast fading and is best suited for stationary environments.

Spectral-fingerprinting identification offers the advantage of embedding IDs within certain frequency bands, though this requires careful spectrum management to avoid interference with data transmission. For this method, the receiver is more complex as it analyzes the spectrum and each subcarrier's power requiring additional signal processing, fast-Fourier transform (FFT) operation and thresholding in the frequency domain. Whether the environment is LOS or NLOS, direct RIS visibility is not necessary; instead, power variation across subcarriers is key. To resolve power delay profile taps, a frequency-selective environment with a large delay spread is required, and short packet transmission can be used. As the number of RISs increases, subblock sizes must decrease for a fixed spectrum. Data and identification can be transmitted simultaneously, though distinguishing taps becomes challenging in low-frequency selective environments, where the RIS may boost the entire spectrum instead of specific subcarriers. This method is suited for multicarrier and frequency-selective scenarios, offering more complexity than amplitude-based methods but less than BS-side methods. It can be applied in both dynamic and static environments, with no strict need for a dedicated identification period, though one may improve reliability.

Code domain identification leverages the unique codewords for RISs impart on signals, offering a less intrusive method but requiring sophisticated signal processing. The BS watermarking method is robust and applicable in all scenarios, though it is the most complex, requiring correlation with multiple codewords at the UE. As the number of RISs increases, the coding rate must be extended for better identification, with each RIS needing a longer unique code. This method requires a dedicated identification period, and UEs need access to a RIS code table. It works well in both outdoor and indoor environments, whether LOS or NLOS, and is ideal for high-density deployments due to the scalable number of codes that can be generated. In contrast, spectral fingerprinting and amplitude modulation are limited by available spectrum and time, restricting the number of RISs that can be assigned.

As we advance, the exploration of multi-domain strategies that combine time, power, frequency, and spatial characteristics for RIS identification appears promising. Such an approach could leverage the strengths of each domain while mitigating their individual limitations. It should also be noted that the optimal identification domain and technique may vary in single and multi-RIS zones. Hence, to combat the weaknesses of each strategy, it is crucial to combat these challenges by choosing the most applicable use case and set up for the technique and whether to use single or multicarrier.

6.6 Conclusion

In this article, we have provided comprehensive discussions and a framework for RIS identification for the first time in the literature. Fundamental principles and advantages in wireless networks and the operational impact and strategic importance of RIS identification have been discussed. In addition, we have discussed the issues and challenges inherent in RIS identification and propose potential strategies and future research avenues for realizing RIS identification in different domains, each with various issues and considerations.

Chapter 7

RIS-AIDED POWER-DIFFERENTIATED DUAL-CODE INDEX MODULATION

7.1 Preface

RIS technology has gained significant attention owing to its ability to enhance the performance of wireless communication systems by manipulating the propagation characteristics of reflected electromagnetic waves. In this chapter, we propose a novel RIS-aided power-differentiated dual-code index modulation (RIS-PD-DCIM) scheme in which information bits are transmitted through an M-pulse amplitude modulation (PAM) modulated symbol, the spreading code indices, and the RIS partitioning mechanism. In the RIS-PD-DCIM scheme, the RIS operates at a rate faster than the symbol period to enable spreading and is split into two unequal partitions. Two spreading codes are selected based on IM bits for each RIS partition to spread the incoming signal. Based on an additional bit information, one of the RIS partitions is selected to introduce an additional phase shift of $\pi/2$. Due to unequal partitioning, a power difference is enabled between the in-phase and quadrature components, allowing information transmission via RIS partitioning. To address computational challenges, a low-complexity (LC) detector significantly reducing the decoding burden compared to traditional maximum likelihood (ML) detection methods has also been proposed. Through extensive evaluations, it is demonstrated that RIS-PD-DCIM achieves superior spectral efficiency and error performance compared to its benchmark across various system configurations.

7.2 Introduction

Modern wireless communication systems are advancing significantly hence, there are strict demands for higher data rates, efficient use of available resources, novel and innovative solutions to enable the envisioned vertical applications and communication use-cases such as autonomous vehicles, virtual/augmented reality, smart homes and cities, precise localization and much more. To enable these, many techniques and technologies are investigated and developed, aiming to meet these stringent requirements. Some of these techniques and technologies include IM and RISs.

IM is a promising technique that introduces flexibility in communication designs by transmitting information bits through not only modulated symbols but also through the indices of transmit entities [Basar et al., 2017]. Through embeding information bits to the indices of subcarriers [Arslan et al., 2020a], transmit and receive antennas [Basar et al., 2017], RIS partitions [Arslan et al., 2024], and spreading codes [Kaddoum et al., 2015], additional bits can be transmitted in various domains such as frequency, time, code, and space. Due to the flexible structure of IM-aided systems, significant performance gains can be obtained from the activated pattern of the indexed entities, which results in significant performance gains.

On the other hand, RIS technology has recently emerged and gained significant popularity in academia and industry due to its unique capability to intelligently manipulate the wireless channel, introducing a degree of flexibility where we once had no control [Liu et al., 2021, Arslan et al., 2022b]. An RIS is a large array with many cost-effective elements that can reflect, manipulate, absorb and even amplify impinging signals with an adjustable reflecting coefficient. By doing so, RISs may artificially enhance existing wireless communication as seen in numerous studies where they expliot a RIS to enhance communication performance [Pan et al., 2021, Gevez et al., 2024]. RIS-aided wireless communication systems may improve communication performance aiding in localization and sensing [Wymeersch et al., 2020, Alamzadeh et al., 2021], enhancing the physical layer security [Khalid et al., 2023] and even practical studies have been applied to aid in real-world deployment of

RIS technology[Araghi et al., 2022, Arslan et al., 2023a, Arslan et al., 2025]. Hence, the RIS technology is a promising tool to exploit in wireless communication systems. However, RISs do come with problems of their own and leveraging the benefits of RIS with other technologies present significant potential in system designs.

Both RIS and IM technologies introduce great flexibility to a wireless communication system and researchers exploit the benefits of each to propose further enhanced system designs. Some of these fundamental studies are as follows where in [Basar, 2020a], an RIS is leveraged to implement receive spatial modulation (RSM) and receive space shift keying (RSSK) by selecting receive antenna indices based on IM bits. Additionally, [Zhang et al., 2022a] presents a generalized space shift keying (SSK) scheme in which multiple receive antennas at the receiver are specified via an RIS, thereby increasing the total number of information bits conveyed through IM. In [Yuan et al., 2021], to allow two receive antennas to be chosen, an RIS is split into two segments, with the first and second segments creating the in-phase and quadrature components of signals at the designated antennas, respectively. The number of targeted receive antennas is strategically varied to both boost data rate and improve error performance in [Dogukan et al., 2024]. Furthermore, [Asmoro and Shin, 2022] introduces a method called RIS grouping-based IM (RGB-IM), where indices of RIS sub-groups serve as carriers of information bits and the authors in [Arslan et al., 2024] extend this concept to a hybrid RIS framework, using all RIS elements to further enhance the received instantaneous SNR while still enabling IM.

Leveraging IM-oriented studies into RIS-assisted wireless systems, code IM (CIM) has been integrated with RISs to exploit the advantages of both IM and spreading codes. Some fundamental studies include [Cogen et al., 2024], where an RIS-CIM approach is introduced for a single-input single-output (SISO) scenario, with CIM performed at the transmitter and the communication link established via an RIS. Furthermore, [Li et al., 2023] proposes RIS-CIM, which applies CIM directly on the RIS by configuring it at a rate exceeding the symbol duration to facilitate spreading. Two low-complexity detectors, which execute dispreading and demodulation separately for the RIS-CIM signal, are designed in [Jin et al., 2023]. To further expand the IM bit capacity, [Ozden et al., 2024] presents RIS-CIM-RSM for a single-input multiple-output (SIMO) configuration, merging RIS-CIM and receive spatial modulation (RSM). Additionally, [Jin et al., 2024] employs an active RIS framework to carry out both CIM and space shift keying (SSK). While these works have combined RIS and CIM effectively, there remains considerable scope for advancing RIS-CIM-based methods, especially in enhancing error performance, developing low-complexity detection strategies, and achieving greater spectral and energy efficiency.

In this chapter, we introduce a novel RIS-aided power-differentiated dual CIM (RIS-PD-DCIM) scheme designed to improve the spectral efficiency and error performance of wireless communication systems. The proposed scheme achieves information transmission by utilizing a combination of M-pulse amplitude modulation (PAM) symbols, spreading code indices, and an RIS partitioning mechanism. In RIS-PD-DCIM scheme, the RIS operates at a rate faster than the symbol period. This fast operation allows the RIS to adapt its configuration to enable signal spreading within the transmission period. The RIS is divided into two unequal partitions, introducing a deliberate power difference between the reflected signal from two partitions. This unequal partitioning is critical as it facilitates additional information transmission through the differentiation of power levels. For each RIS partition, two spreading codes are selected based on the IM bits, enabling the incoming signal to be effectively spread across selected codes. Furthermore, an additional information bit is used to determine which RIS partition will introduce a $\pi/2$ phase shift to its reflected signal. This phase shift, combined with the unequal partitioning, results in distinct in-phase and quadrature components of the received signal. By encoding information into both the phase and power differences between these components, the RIS-PD-DCIM scheme maximizes the utilization of available resources for information transmission. To address the computational challenges associated with decoding multiple entities, we also propose a low-complexity (LC) detector tailored to the RIS-PD-DCIM framework. The LC detector offers a significant reduction in computational burden compared to traditional maximum likelihood (ML) detection methods, making the scheme practical for real-time implementation and also for

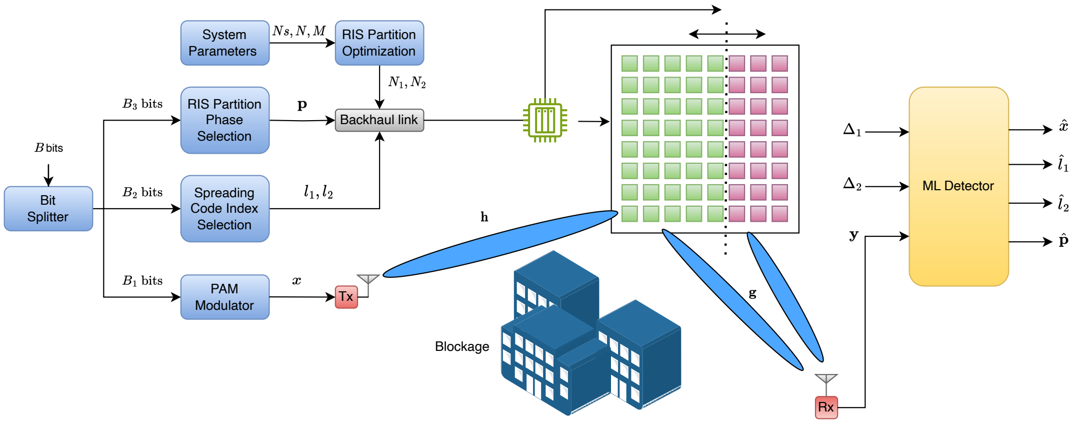

Figure 7.1: System model of the proposed RIS-PD-DCIM scheme.

larger system parameters. Despite its simplicity, the LC detector maintains robust performance in terms of BER, ensuring the scheme's reliability under various system configurations. Through extensive numerical simulations, we demonstrate the superior performance of the RIS-PD-DCIM scheme compared to the existing benchmark method. Our results highlight the scheme's ability to achieve higher spectral efficiency and lower error rates across diverse conditions and RIS configurations. In summary, the RIS-PD-DCIM scheme leverages a unique combination of unequal RIS partitioning, phase shifts, spreading codes, and M-PAM symbols to enable highly efficient and reliable wireless communication. The proposed design not only advances the current state of RIS-aided IM but also paves the way for future innovations in next-generation wireless communication systems.

The remainder of the chapter is organized as follows: chapter 7.3 presents the system model of the proposed RIS-PD-DCIM scheme, and ML and LC detectors are introduced. In chapter 7.4, we analyze the performance of the proposed system considering the computational complexity, spectral, and energy efficiency. Chapter 7.5 provides extensive simulation results that demonstrate the superior error performance of RIS-PD-DCIM across various scenarios. Finally, the study is concluded in chapter 7.6.

7.3 System Model

An RIS-assisted single-input single-output (SISO) communication system is considered for the proposed RIS-PD-DCIM scheme. The direct communication link between the transmitter and the receiver is assumed to be blocked thus, communication is enabled exclusively through an RIS-assisted path where the RIS has N reflective elements. The system model of RIS-PD-DCIM is illustrated in Fig. 7.1, which demonstrates the key components of the proposed scheme. As illustrated in Fig. 7.1, the RIS is separated into two unequal partitions where the first and second RIS parts include N_1 and N_2 number of elements, respectively, i.e., $N = N_1 + N_2$ and $N_1 > N_2$. The Rayleigh channel vector between the transmitter and the RIS can be given as $\mathbf{h} = [h_1, h_2, \cdots, h_N]^{\mathrm{T}}$, where the ith element $h_i = \alpha_i e^{j\phi_i}$ represents the channel coefficient between the transmit antenna and the ith RIS element. Similarly, the Rayleigh channel vector between the RIS and the receiver is denoted as $\mathbf{g} = [g_1, g_2, \cdots, g_N]^{\mathrm{T}}$, where $g_i = \beta_i e^{j\varphi_i}$ corresponds to the channel coefficient between ith RIS element and the receive antenna. Each h_i and g_i follows a complex Gaussian distribution with $\mathcal{CN}(0, 1)$.

Since the RIS operates U times faster than the symbol period T_s, its configuration changes during T_s, where U is the number of chips and chip duration is equal to $T_c = T_s/U$. Therefore, at the uth chip duration, the reflection coefficient of the ith RIS element can be represented as $\vartheta_i^u = e^{j\theta_i^u}$, $i = 1, 2, \cdots, N$, $u = 1, 2, \cdots, U$. The channel vectors $\mathbf{h}$ and $\mathbf{g}$ are assumed to be constant during T_s.

In the proposed RIS-PD-DCIM scheme, the total B number of transmitted bits is partitioned into three parts, B_1, B_2, and B_3. The first part, $B_1 = \log_2(M)$ bits, is mapped to an M-PAM modulated symbol $x \in \mathcal{M}$, where M denotes the modulation order and $\mathcal{M}$ represents the M-ary PAM constellation set. Then, $B_2 = 2\log_2(N_S)$ bits determine two spreading code indices l_1 and l_2, which are used in the first and second RIS parts in an OTA manner, respectively, $l_1, l_2 = 1, \cdots, N_S$, where N_S is the number of spreading codes. Orthogonal Walsh-Hadamard codes are utilized as spreading codes to ensure orthogonality among the signals reflected via different parts of the RIS. The set that includes Walsh-Hadamard codes can be given as $\mathcal{C} = \{\mathbf{c}_1, \mathbf{c}_2, \cdots, \mathbf{c}_{N_S}\}$, $\mathbf{c}_\mu = [c_\mu^1, c_\mu^2, \cdots, c_\mu^U]$, $c_\mu^u = \{-1, +1\}$, $\mu = 1, 2, \cdots, N_S$, $u = 1, 2, \cdots, U$, where U is the length of the μth spreading code $\mathbf{c}_\mu$ and the number of chips. The selected spreading codes according to B_2 are $\mathbf{c}_{l_1}$ and $\mathbf{c}_{l_2}$. Finally, the $B_3 = 1$ bit determines which of the two RIS partitions applies an additional $\pi/2$ phase shift. A phase rotation vector, $\mathbf{p} = [p_1, p_2]^{\mathrm{T}}$, is defined, where $\mathbf{p}$ can be either $[0, \pi/2]^{\mathrm{T}}$ or $[\pi/2, 0]^{\mathrm{T}}$, depending on the incoming $B_3 = 1$ bit. Note that a $\pi/2$ rotation is applied to a single RIS part within one symbol duration. As a result, the spectral efficiency of RIS-PD-DCIM can be given in terms of bps/Hz, as follows:

$$\eta = \frac{B_1 + B_2 + B_3}{U} = \frac{\log_2(M) + 2\log_2(N_S) + 1}{U}. \tag{7.1}$$

Assuming $\vartheta_i^u = e^{j\psi_i^u}$ is the reflection coefficient of ith RIS element at uth chip and x is transmitted, the received signal can be obtained for the uth chip as:

$$y_u = \frac{x}{\sqrt{U}} \sum_{i=1}^{N} h_i \vartheta_i^u g_i + w_u, \tag{7.2}$$

where w_u is an AWGN sample at the uth chip with distribution $\mathcal{CN}(0, N_0)$ and N_0 is the noise variance.

By exploiting the selected parameters $\mathbf{c}_{l_1}$, $\mathbf{c}_{l_2}$, $\mathbf{p}$ and channel vectors $\mathbf{h}$ and $\mathbf{g}$, the phase configuration of the ith RIS element for the uth chip signal can be given as:

$$\psi_i^u = \begin{cases} -\phi_i - \varphi_i + \angle c_{l_1}^u + p_1, & \text{if } i \le N_1, \\ -\phi_i - \varphi_i + \angle c_{l_2}^u + p_2, & \text{otherwise}, \end{cases} \tag{7.3}$$

where $\angle c_m^u \in \{0, \pi\}$ is the angle of c_m^u, $m \in \{l_1, l_2\}$. As seen in (7.3), the RIS elements are coherently aligned with channel coefficients, and the spreading codes and rotation are implemented OTA depending on the RIS part. Therefore, by substituting (7.3) into (7.2), the received signal can be rewritten as:

$$y_u = \frac{x}{\sqrt{U}} \left(c_{l_1}^u e^{jp_1} \sum_{i=1}^{N_1} \alpha_i \beta_i + c_{l_2}^u e^{jp_2} \sum_{i=N_1+1}^{N} \alpha_i \beta_i \right) + w_u, \tag{7.4}$$

The channel vectors corresponding to the first and second parts of the RIS can be represented as $\mathbf{h}_1$, $\mathbf{g}_1$ and $\mathbf{h}_2$, $\mathbf{g}_2$, respectively, i.e. $\mathbf{h} = [\mathbf{h}_1^{\mathrm{T}}, \mathbf{h}_2^{\mathrm{T}}]^{\mathrm{T}}$, $\mathbf{g} = [\mathbf{g}_1^{\mathrm{T}}, \mathbf{g}_2^{\mathrm{T}}]^{\mathrm{T}}$. Hence, the received signal for a symbol duration in vector form can be written as:

$$\mathbf{y} = \frac{x}{\sqrt{U}} \left[(|\mathbf{h}_1^{\mathrm{T}}||\mathbf{g}_1|)\mathbf{c}_{l_1} e^{jp_1} + (|\mathbf{h}_2^{\mathrm{T}}||\mathbf{g}_2|)\mathbf{c}_{l_2} e^{jp_2}\right] + \mathbf{w}, \tag{7.5}$$

where $\mathbf{w} = [w_1, w_2, \cdots, w_U]$. Therefore, the signal-to-noise ratio (SNR) can be given as follows:

$$\begin{aligned}\gamma =& \frac{\left(|\mathbf{h}_1^{\mathrm{T}}||\mathbf{g}_1|\right)^2 + \left(|\mathbf{h}_2^{\mathrm{T}}||\mathbf{g}_2|\right)^2}{N_0}, \\ =& \frac{\left[\sum\limits_{i=1}^{N_1} \alpha_i \beta_i\right]^2 + \left[\sum\limits_{i=N_1+1}^{N} \alpha_i \beta_i\right]^2}{N_0}.\end{aligned} \tag{7.6}$$

7.3.1 Detection

In this subchapter we first introduce the ML detector, which offers optimal decoding performance. However, its decoding complexity becomes significantly high, especially for large values of M, N_S, and N, as it jointly decodes all transmit entities. To address this issue, we propose an LC detector, which reduces the decoding complexity by decoding the transmit entities sequentially, one at a time.

ML Detector

On the receiver side, after obtaining $\mathbf{y}$, the ML detector considers all possible combinations for joint detection of the modulated symbol, spreading code indices, and phase rotation vectors, achieving optimal performance. Therefore, the ML detection rule for RIS-PD-DCIM is given as:

$$\hat{x}, \hat{l}_1, \hat{l}_2, \hat{\mathbf{p}} = \arg \min_{x, l_1, l_2, \mathbf{p}} \left\| \mathbf{y} - \frac{x}{\sqrt{U}} \left(\Delta_1 \mathbf{c}_{l_1} e^{jp_1} + \Delta_2 \mathbf{c}_{l_2} e^{jp_2}\right) \right\|^2, \tag{7.7}$$

where $\Delta_1 = |\mathbf{h}_1^{\mathrm{T}}||\mathbf{g}_1|$ and $\Delta_2 = |\mathbf{h}_2^{\mathrm{T}}||\mathbf{g}_2|$. The decoded entities $\hat{x}$, $\hat{l}_1$, $\hat{l}_2$, $\hat{\mathbf{p}}$ are exploited to obtain the decoded bits.

Since the ML detector jointly detects modulated symbols, spreading code indices, and the RIS partition rotation vector, its decoding complexity is substantially high and increases further with higher values of M, N_S, and N. To reduce the computational burden of decoding the RIS-PD-DCIM signal, we propose an LC detector that decodes the transmit entities sequentially, one at a time.

Low Complexity Detector

In contrast to the joint detection performed by the ML detector, the LC detector decodes the transmitted entities one-by-one in order to reduce the decoding complexity. In the LC detector, firstly, the real and imaginary parts of the received signal are obtained and can be expressed as:

$$\mathbf{y}^{\mathfrak{R}} = \begin{bmatrix} y_1^{\mathfrak{R}} & y_2^{\mathfrak{R}} & \cdots & y_U^{\mathfrak{R}} \end{bmatrix}, \tag{7.8}$$

$$\mathbf{y}^{\mathfrak{I}} = \begin{bmatrix} y_1^{\mathfrak{I}} & y_2^{\mathfrak{I}} & \cdots & y_U^{\mathfrak{I}} \end{bmatrix}, \tag{7.9}$$

where $y_u^{\mathfrak{R}} = \mathfrak{Re}\{y_u\}$ and $y_u^{\mathfrak{I}} = \mathfrak{Im}\{y_u\}$, $u = 1, \cdots, U$.

Then, the spreading code indices for the real and imaginary parts of the received signal are obtained by despreading all possible spreading codes, as follows:

$$\hat{m}_1 = \arg \max_{m_1 \in \{1, \cdots, N_S\}} \left\{ \left| \mathbf{y}^{\mathfrak{R}} \mathbf{c}_{m_1}^{\mathrm{T}} \right|^2 \right\}, \tag{7.10}$$

$$\hat{m}_2 = \arg \max_{m_2 \in \{1, \cdots, N_S\}} \left\{ \left| \mathbf{y}^{\mathfrak{I}} \mathbf{c}_{m_2}^{\mathrm{T}} \right|^2 \right\}, \tag{7.11}$$

After obtaining the spreading code indices, $\mathbf{y}^{\mathfrak{R}}$ and $\mathbf{y}^{\mathfrak{I}}$ are despreaded by using $\mathbf{c}_{\hat{m}_1}$ and $\mathbf{c}_{\hat{m}_2}$, respectively, as follows:

$$\Omega^{\mathfrak{R}} = \left| \mathbf{y}^{\mathfrak{R}} \mathbf{c}_{\hat{m}_1}^{\mathrm{T}} \right|^2, \tag{7.12}$$

$$\Omega^{\mathfrak{I}} = \left| \mathbf{y}^{\mathfrak{I}} \mathbf{c}_{\hat{m}_2}^{\mathrm{T}} \right|^2. \tag{7.13}$$

To determine the indices l_1 and l_2, Algorithm 1 is employed. The detected spreading code indices m_1 and m_2 act as preliminary indices to map to l_1 and l_2. However, to assign these values accurately, the parameters $\Omega^{\mathfrak{R}}$ and $\Omega^{\mathfrak{I}}$ derived

Algorithm 2 Detection and Decoding Algorithm

Require: $\Omega^{\Re}$, $\Omega^{\Im}$, Δ_1, Δ_2, $\hat{m}_1$, $\hat{m}_2$

Ensure: $\hat{\mathbf{p}}$, Δ, $\hat{l}_1$, $\hat{l}_2$

1: **Compare despread signals:**

2: **if** $\Omega^{\Re} > \Omega^{\Im}$ **then**

3: Assign the decoded rotation vector: $\hat{\mathbf{p}} \leftarrow [0, \pi/2]^{\mathrm{T}}$

4: Compute Δ:

$$\Delta \leftarrow \Delta_1 \mathbf{c}_{\hat{m}_1} + j\Delta_2 \mathbf{c}_{\hat{m}_2}$$

5: Set decoding indices:

$$\hat{l}_1 \leftarrow \hat{m}_1, \quad \hat{l}_2 \leftarrow \hat{m}_2$$

6: **else if** $\Omega^{\Re} < \Omega^{\Im}$ **then**

7: Assign the decoded rotation vector: $\hat{\mathbf{p}} \leftarrow [\pi/2, 0]^{\mathrm{T}}$

8: Compute Δ:

$$\Delta \leftarrow \Delta_2 \mathbf{c}_{\hat{m}_1} + j\Delta_1 \mathbf{c}_{\hat{m}_2}$$

9: Set decoding indices:

$$\hat{l}_1 \leftarrow \hat{m}_2, \quad \hat{l}_2 \leftarrow \hat{m}_1$$

10: **end if**

from the despreading process are compared as seen in lines 2 and 6 of Algorithm 1. This comparison ensures that the correct index association for l_1 and l_2 is made, reflecting the distribution of the power of the received signal between its in-phase and quadrature components. Since l_1 and l_2 are initially unknown, Algorithm 1 evaluates m_1 and m_2 in conjunction with the observed power levels to finalize the index assignments.

After determining the indices l_1 and l_2, as well as the associated parameters, the final step involves decoding the modulated symbol. By leveraging the derived indices and computed parameters, the following detection rule is applied to reconstruct the transmitted symbol:

$$\hat{x} = \arg\min_{x} \|\mathbf{y} - \Delta x\|^2 . \tag{7.14}$$

Since each entity is decoded separately, the LC detector reduces the decoding complexity dramatically compared to the ML detector. The decoding complexity of the ML and LC detectors are compared and analyzed in the subsequent subchapter in detail.

7.4 Performance Analyses

In this subchapter, the performance of the proposed RIS-PD-DCIM is analyzed and compared to that of its benchmark in terms of spectral efficiency, detection complexity, and energy efficiency. Note that the following analysis has been performed by assuming that the number of spreading codes is equal to the number of chips, i.e., $N_S = U$.

7.4.1 Spectral Efficiency Analysis

In this subchapter, the spectral efficiency values of RIS-CIM and RIS-PD-DCIM are compared. The spectral efficiencies of RIS-CIM and RIS-PD-DCIM, in terms of bps/Hz, can be given as:

$$\eta_{\text{RIS-CIM}} = \frac{\log_2(M) + \log_2(N_S)}{N_S}, \tag{7.15}$$

$$\eta_{\text{RIS-PD-DCIM}} = \frac{\log_2(M) + 2\log_2(N_S) + 1}{N_S}, \tag{7.16}$$

respectively.

Fig. 7.2 illustrates the spectral efficiency comparison of the RIS-CIM and RIS-PD-DCIM schemes for varying parameters M and N_S. It can clearly be seen that as η increases with respect to M. On the other hand, as N_S increases, the spectral efficiency decreases since in (7.15) and (7.16), η is divided by N_S. In each case,

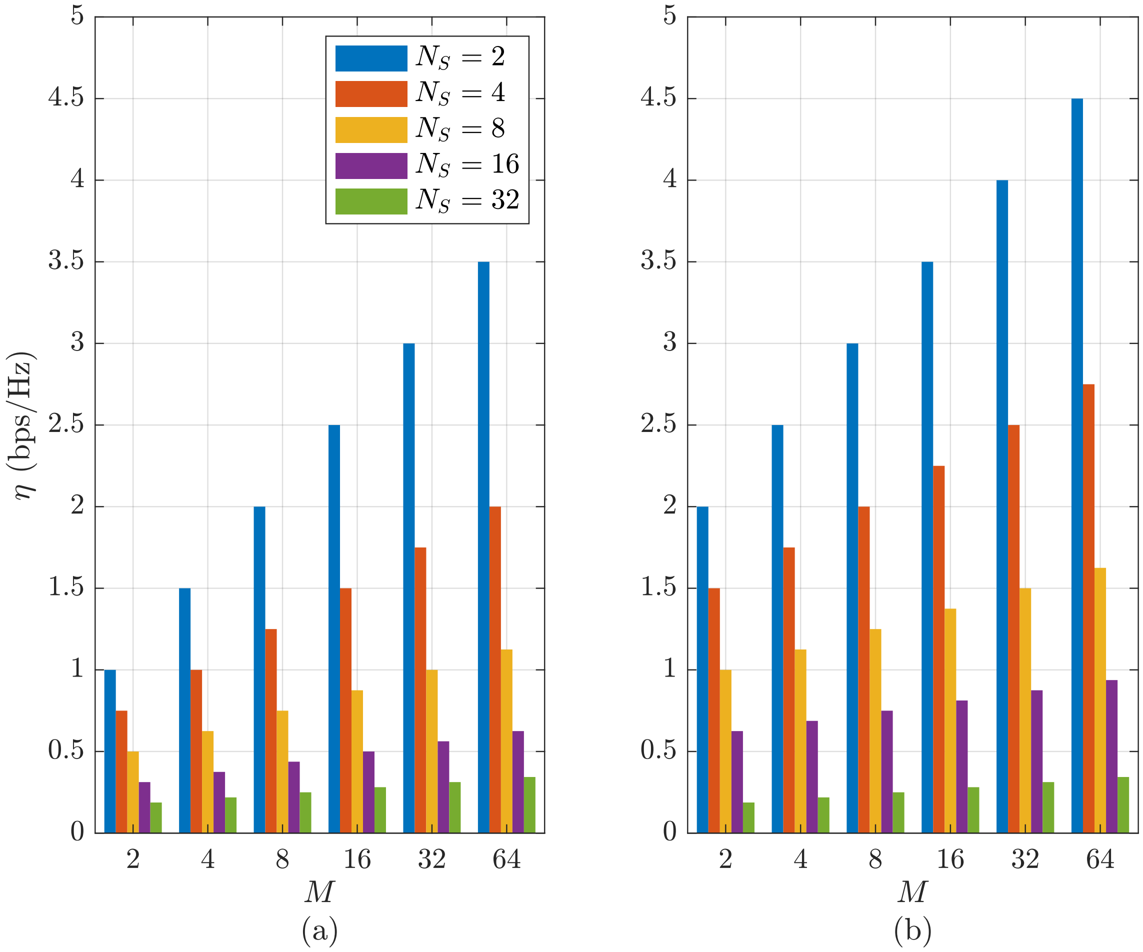

Figure 7.2: Spectral efficiency comparison of (a) RIS-CIM and (b) RIS-PD-DCIM for varying M and N_S values.

RIS-PD-DCIM achieves higher spectral efficiency compared to RIS-CIM due to its ability to encode additional information bits through both code indices and RIS partitions, leveraging a higher number of IM bits.

7.4.2 Detection Complexity Analysis

In this subchapter, we analyze and compare the computational complexities of the ML and LC detectors in terms of real multiplications. The ML detector relies on an exhaustive search, resulting in a computational complexity given by:

$$\mathfrak{C}^{\text{ML}}_{\text{RIS-PD-DCIM}} = 5N + 32MN_S^3. \tag{7.17}$$

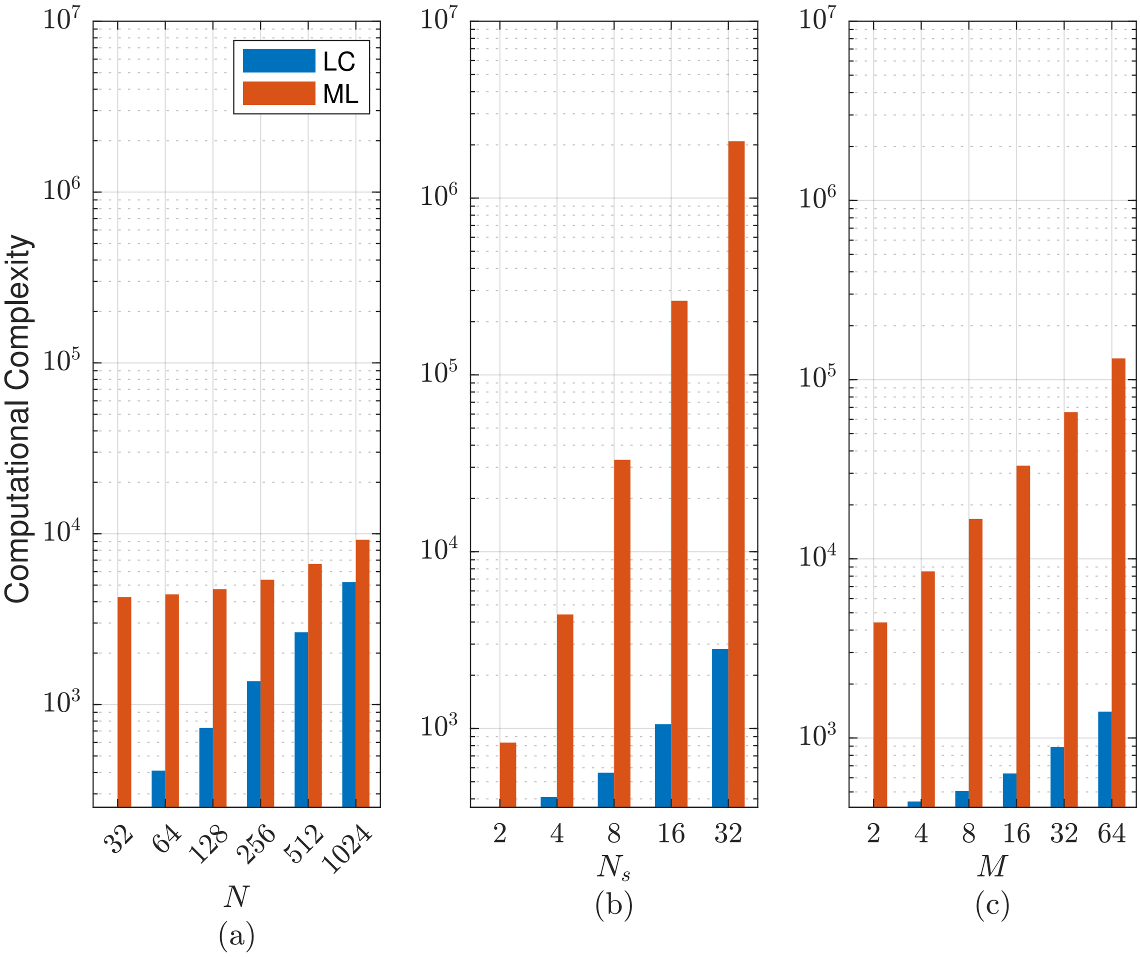

Figure 7.3: Computational complexity comparison of ML and LC detector for the RIS-PD-DCIM scheme for (a) varying the number of RIS elements (N), (b) varying the number of spreading codes (N_S), (c) varying the modulation order (M).

This complexity is proportional to the modulation order M and the cube of the number of spreading codes N_S. Consequently, decoding the RIS-PD-DCIM signal with the ML detector can become computationally exhaustive, particularly in scenarios with large values of M and N_S.

To address this limitation, we propose an LC detector which offers significantly lower computational complexity compared to the ML detector. By counting the real multiplications required for the LC detector, its computational complexity can be obtained as

$$\mathfrak{C}^{\text{LC}}_{\text{RIS-PD-DCIM}} = 2(N_S + 1)^2 + 2N_S + 5N + 4MN_S, \tag{7.18}$$

which is considerably more efficient than the ML detector, especially as M and N_S increase.

In Fig. 7.3, the computational complexity of the ML and LC detectors is compared in terms of real multiplications for various system parameters: number of RIS elements (N), modulation order (M), and the number of spreading codes (N_S). In Fig. 7.3(a), N is varied while $N_S = 4$ and $M = 2$ and it can be seen that the decoding complexity increases as N increases. Furthermore, in Fig. 7.3(b), N_S is varied while $N = 64$ and $M = 2$, and it can be observed that as N_S increases, the decoding complexity increases dramatically for the ML detector. On the other hand, in Fig. 7.3(c) M is varied while $N_S = 4$ and $N = 64$, and it is shown that as M increases, the decoding complexity increases for both detectors. Even for low values of parameters, the decoding complexity is significantly high in the ML detector and experiences a steeper rise across all cases compared to the LC detector, making it computationally prohibitive for large values of N, M, and N_S. In contrast, the LC detector consistently provides a much lower computational burden, making it more efficient and practical for real-world applications.

In Figs. 7.4(a) and (b), the computational complexities of the LC detectors for the RIS-CIM benchmark and RIS-PD-DCIM schemes are compared across various cases with SE of $\eta = 1.5$ and SE of $\eta = 2$ for all schemes and cases, respectively. The computational complexities of the LC detectors for the RIS-CIM and RIS-PD-DCIM schemes, in terms of real multiplications, can be expressed as follows, respectively:

$$\mathfrak{C}^{\text{LC}}_{\text{RIS-CIM}} = 2N_S^2 + 4N_S + MN + 4M, \tag{7.19}$$

$$\mathfrak{C}^{\text{LC}}_{\text{RIS-PD-DCIM}} = 2(N_S + 1)^2 + 2N_S + 5N + 4MN_S. \tag{7.20}$$

For Figs. 7.4(a) and (b), the specific parameters for each scheme in each case are summarized in Tables 7.1 and 7.2, respectively. As seen in Fig. 7.4, the LC detector for the proposed RIS-PD-DCIM scheme provides less computational complexity in

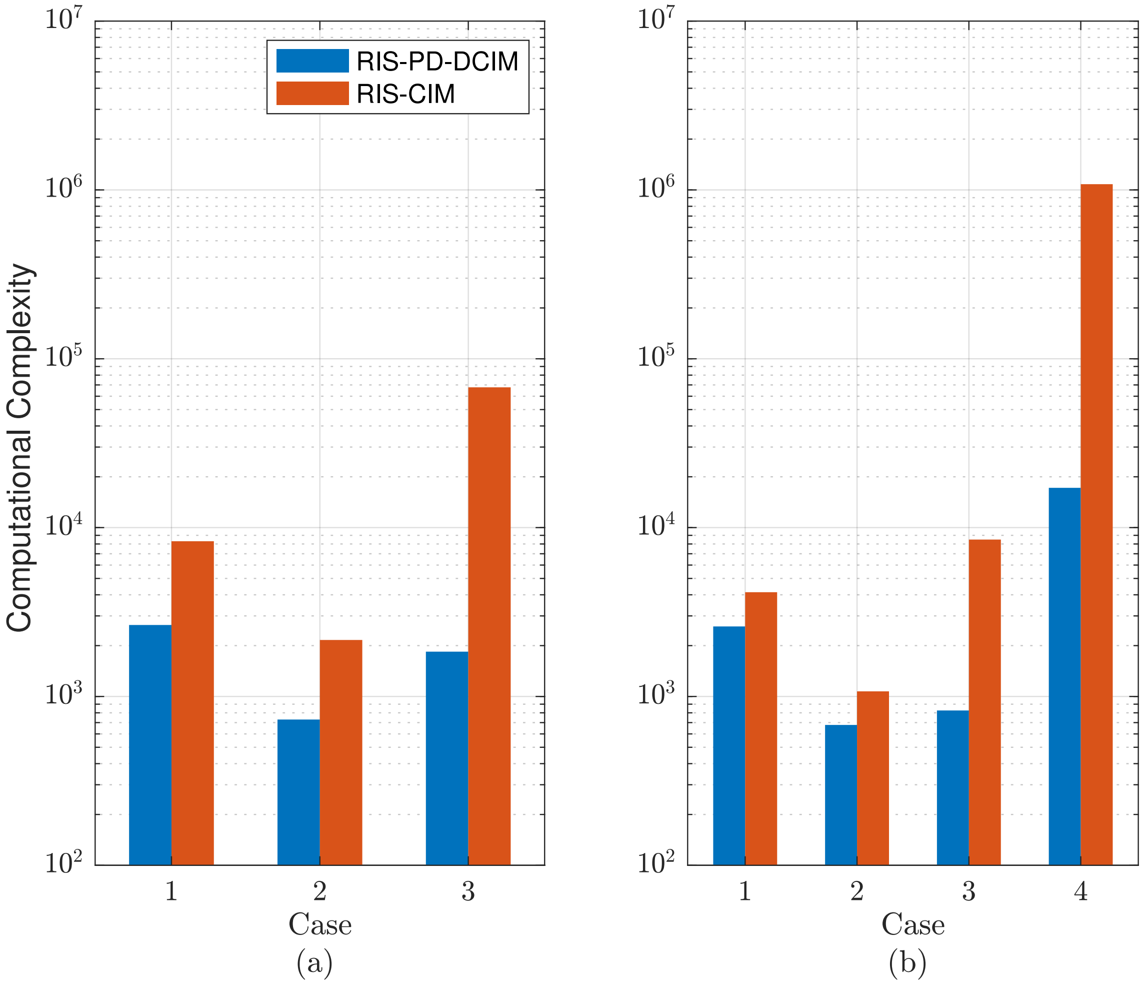

Figure 7.4: Computational complexity comparison of LC detectors for RIS-CIM and RIS-PD-DCIM schemes across varying cases.

terms of real multiplications across all cases and scenarios compared to the LC detector of RIS-CIM. This is primarily due to the high modulation order used in RIS-CIM to achieve the same bpcu as RIS-PD-DCIM, since RIS-CIM transmits fewer information bits via IM.

The computational complexity of the LC detectors for the RIS-CIM and proposed RIS-PD-DCIM schemes is analyzed across varying cases, as illustrated in Figs. 7.4(a) and (b). A comparison between Cases 1 and 2 highlights the influence of the RIS size on the detector complexity. Specifically, as the RIS size decreases from $N = 512$ in Case 1 to $N = 128$ in Case 2, the complexity in both schemes reduces proportionally,

Table 7.1: Case and parameters (N, N_S, M) for RIS-CIM and RIS-PD-DCIM schemes for $\eta = 1.5$.

Case	**RIS-CIM**	**RIS-PD-DCIM**
1	$(512, 4, 16)$	$(512, 4, 2)$
2	$(128, 4, 16)$	$(128, 4, 2)$
3	$(128, 8, 512)$	$(128, 8, 32)$

Table 7.2: Case and parameters (N, N_S, M) for RIS-CIM and RIS-PD-DCIM schemes for $\eta = 2$.

Case	**RIS-CIM**	**RIS-PD-DCIM**
1	$(512, 2, 8)$	$(512, 2, 2)$
2	$(128, 2, 8)$	$(128, 2, 2)$
3	$(128, 4, 64)$	$(128, 4, 8)$
4	$(128, 8, 8192)$	$(128, 8, 512)$

irrespective of η. This reduction is attributed to the smaller RIS size. On the other hand, in Cases 2 and 3, the combined effect of increasing N_S and M for a fixed η leads to a noticeable rise in complexity for both schemes. However, the RIS-CIM scheme exhibits a significantly steeper increase in complexity compared to the proposed RIS-PD-DCIM scheme. This disparity underscores the computational efficiency of the latter. The comparison of Cases 3 and 4 in Fig. 7.4(b) further emphasizes the impact of increasing N_S and M. The RIS-CIM scheme experiences a substantial surge in complexity, necessitating extremely high modulation orders, as detailed in Tables 7.1 and 7.2, to achieve performance comparable to RIS-PD-DCIM. In contrast, the LC detector of RIS-PD-DCIM consistently maintains the lowest computational complexity across all scenarios, establishing it as the most efficient and scalable solution.

7.4.3 Energy Efficiency Analysis

Energy efficiency has emerged as a critical concern due to the rapid development and widespread adoption of wireless communication technologies. The need for energy-efficient designs in wireless networks has become more pressing over time. In this subchapter, we examine the energy efficiency of the proposed RIS-PD-DCIM scheme and compare its performance with that of existing benchmark schemes. By encoding a larger number of IM bits than RIS-CIM, the RIS-PD-DCIM scheme achieves higher energy efficiency. The percentage of energy savings of the proposed RIS-PD-DCIM scheme relative to the reference RIS-CIM scheme can be expressed as follows:

$$EE_{saving} = \left(1 - \frac{\eta_{\text{RIS-CIM}}}{\eta_{\text{RIS-PD-DCIM}}}\right) E_b\% \tag{7.21}$$

where, $E_b = 1/\log_2(M)$ represents the bit energy. The energy-saving performance of the RIS-PD-DCIM scheme is compared with that of RIS-CIM across various cases, as outlined in Table 7.3. As illustrated in Fig. 7.5, the proposed scheme outperforms RIS-CIM in terms of energy efficiency. This improvement becomes more significant when the modulation order M is smaller, as the share of IM bits in the overall transmitted bits increases.

7.4.4 Optimum RIS Partitioning

In this subchapter, we briefly discuss the selection of N_1 and N_2 for optimal RIS partitioning. We need to determine N_1 and N_2 to create an adequate power difference to enable detection of the distinguishable RIS partitions and spreading codes at the receiver. If the RIS partitions are not partitioned in the optimal manner, detection performance significantly deteriorates. It should be noted that when searching for the optimum N_1 and N_2 values, it should be performed at high SNR values with reliable error performance. If N_2 is determined then $N_1 = N - N_2$ is also known. It

Table 7.3: Case and Parameters for Energy Efficiency

Case	M	N_S
1	2	2
2	2	4
3	4	2
4	4	4
5	8	2
6	8	4
7	16	2
8	16	4
9	32	2
10	32	4

can be seen from Fig. 7.6 that the optimum N_2 can be obtained as 18 at an SNR value of 8 dB for a certain system configuration considering the average BER. In Fig. 7.6 and the simulations in the subsequent subchapter, we find the N_2 values providing a BER of at least 10^{-4} for reliable performance.

7.5 Simulation Results

In this subchapter, the error performance of the proposed RIS-PD-DCIM scheme is evaluated through extensive computer simulations for varying system parameters and spectral efficiencies and compared with benchmark scheme RIS-CIM.

In Fig. 7.7, the error performance of the ML and LC detectors is compared for $M = 2$, $N_S = 4$, and varying N values where $N_2 = 18, 40, 82$ are selected for $N = 64, 128, 256$, respectively. It can be seen that as N increases, both detectors show improved error performance due to enhanced SNR at the receive antenna

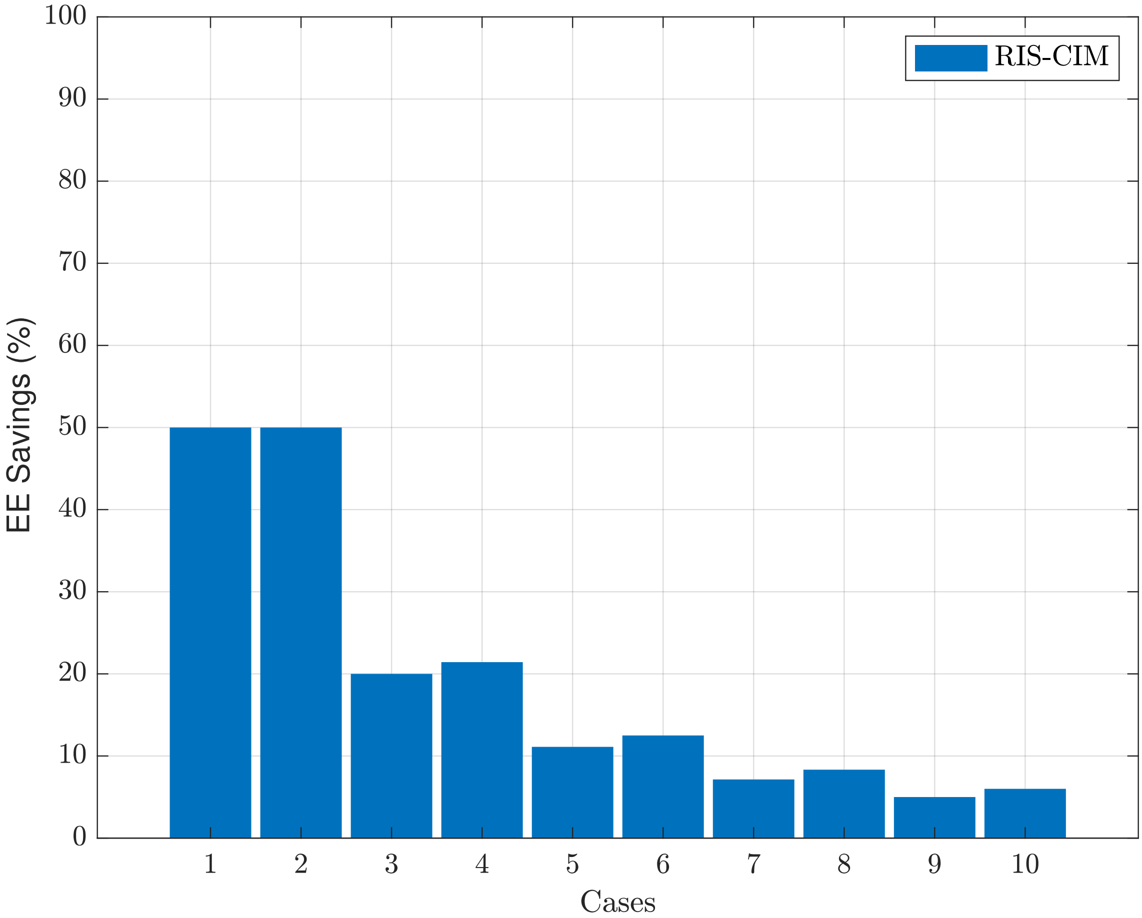

Figure 7.5: Comparison of energy-saving percentages for RIS-CIM and RIS-PD-DCIM across different cases.

since a larger RIS reflects a stronger signal with more elements. The ML detector achieves optimal performance by jointly detecting modulated symbol and spreading code indices, whereas the performance of the LC detector is suboptimal. In terms of computational complexity, the ML detector requires a much higher number of real multiplications compared to the LC detector. Although the ML detector outperforms the LC detector, its computational cost becomes detrimental for larger values of M and N_S, making the LC detector a practical alternative in such scenarios. Even though the LC detector provides slightly worse BER performance than the ML detector, it provides a significant reduction in detection complexity.

In Fig. 7.8, the error performance of the RIS-PD-DCIM scheme is demonstrated

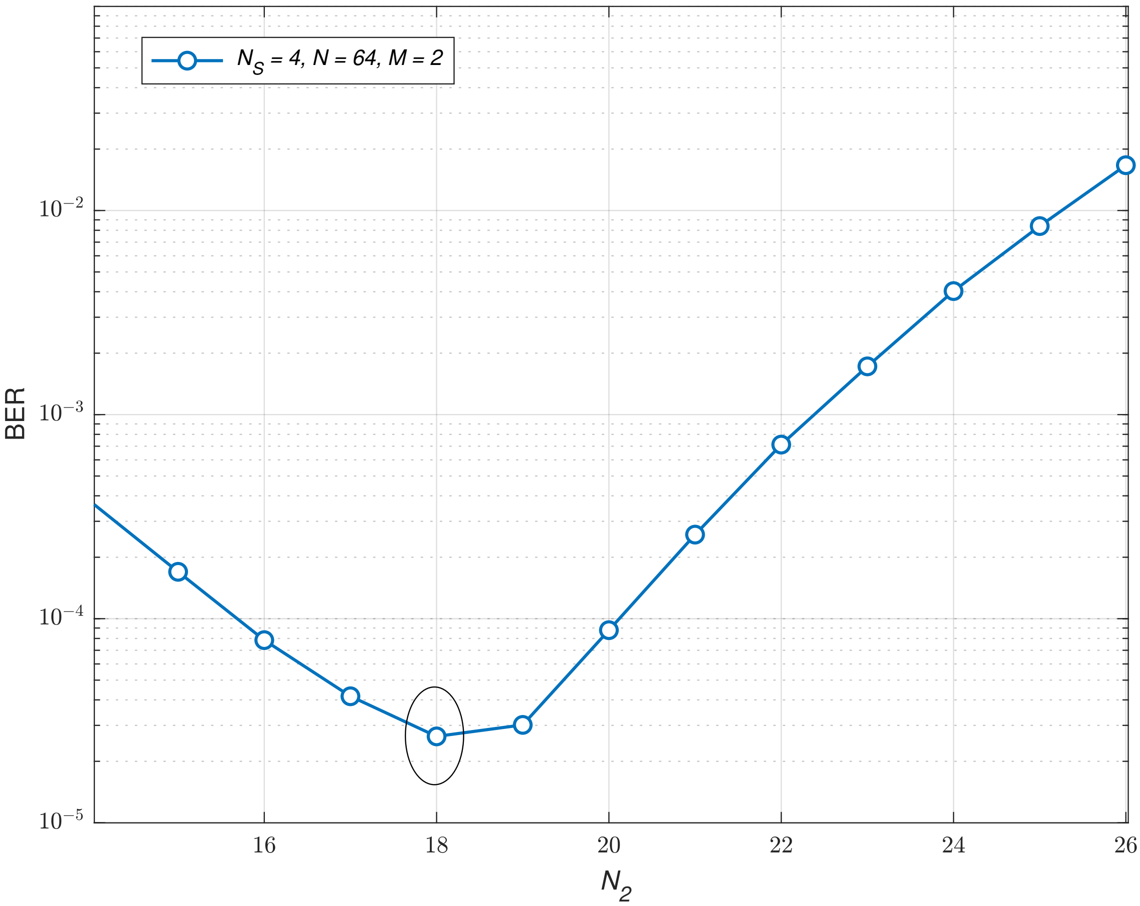

Figure 7.6: Determining optimum N_2 based on average BER for specified parameters.

for varying M and N with $N_S = 4$. As it can be seen in Fig. 7.8, as N increases, the error performance improves due to higher SNR obtained at the receiver. For all values of N, increasing M results in degradation in error performance, and this presents a trade-off between error performance and spectral efficiency.

In Fig. 7.9, the error performance of the proposed RIS-PD-DCIM scheme is compared with the benchmark scheme for 10 bpcu and varying N values. The parameters for each scheme are as follows: for RIS-CIM, $N_S = 16$ and 64-QAM, and for RIS-PD-DCIM, $N_S = 16$, and 2-PAM. As seen in Fig. 7.9, RIS-PD-DCIM outperforms RIS-CIM for $N = 128, 256$ in terms of BER. This performance gain is attributed to the lower modulation order used in RIS-PD-DCIM, compared to

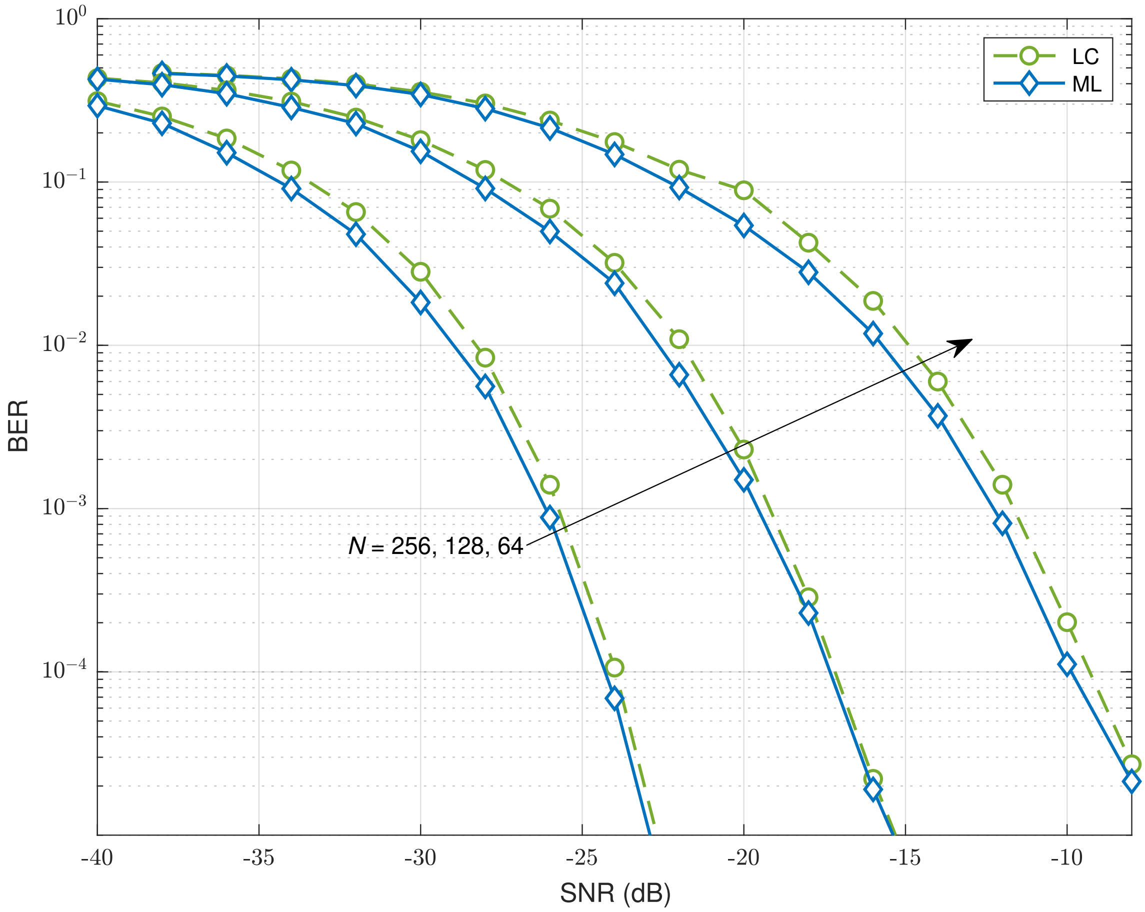

Figure 7.7: Error performance comparison of the ML and LC detectors for $M = 2$, $N_S = 4$ and varying N values.

benchmark schemes, while still achieving the same bpcu value. The lower modulation order allows RIS-PD-DCIM to maintain a greater minimum Euclidean distance between constellation points, thereby reducing the probability of symbol errors. For $N = 64$, since N is small, the number of RIS elements in the of RIS part with less elements assigned to the spreading code becomes inadequate; hence, the reliability of spreading code introduced from the small RIS part reduces, affecting the overall BER even though a lower modulation order is used. The performance improvement of RIS-PD-DCIM is particularly noticeable as N increases, showing a larger performance gap at higher N values.

In Fig. 7.10, the error performance of the RIS-PD-DCIM scheme is compared

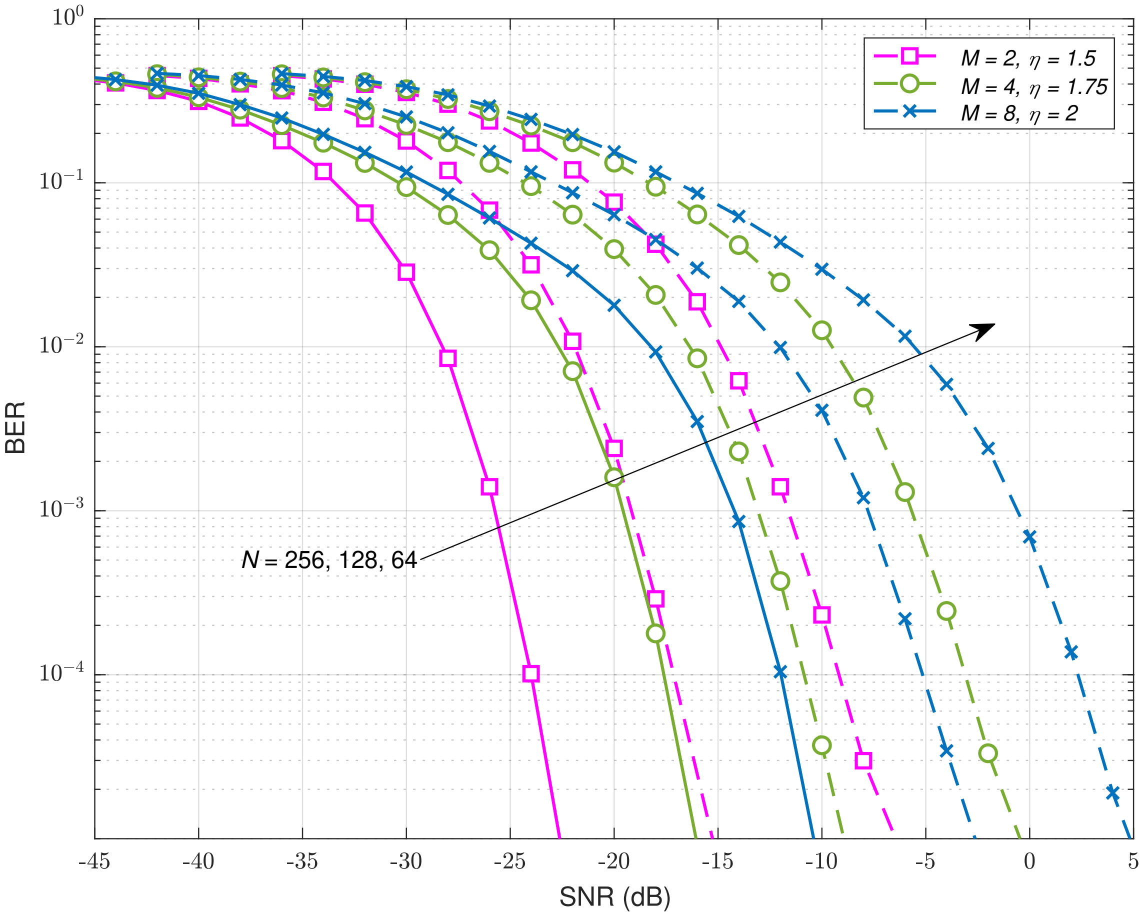

Figure 7.8: Error performance comparison of RIS-PD-DCIM for varying N and M.

with RIS-CIM for 12 bpcu and varying N values. The parameters for each scheme are as follows: for RIS-CIM, $N_S = 32$ and 128-QAM, and for RIS-PD-DCIM, $N_S = 32$, and 2-PAM. As shown in 7.10, RIS-PD-DCIM consistently achieves better error performance compared to RIS-CIM across all values of N. This improvement is primarily due to the lower modulation order $M = 2$ used in RIS-PD-DCIM, which allows for a greater minimum Euclidean distance between constellation points, reducing the probability of symbol errors. In contrast, RIS-CIM uses a much higher modulation order $M = 128$, which leads to a higher likelihood of error at comparable SNR levels. The performance gap between RIS-PD-DCIM and the benchmark scheme becomes even more pronounced as N increases.

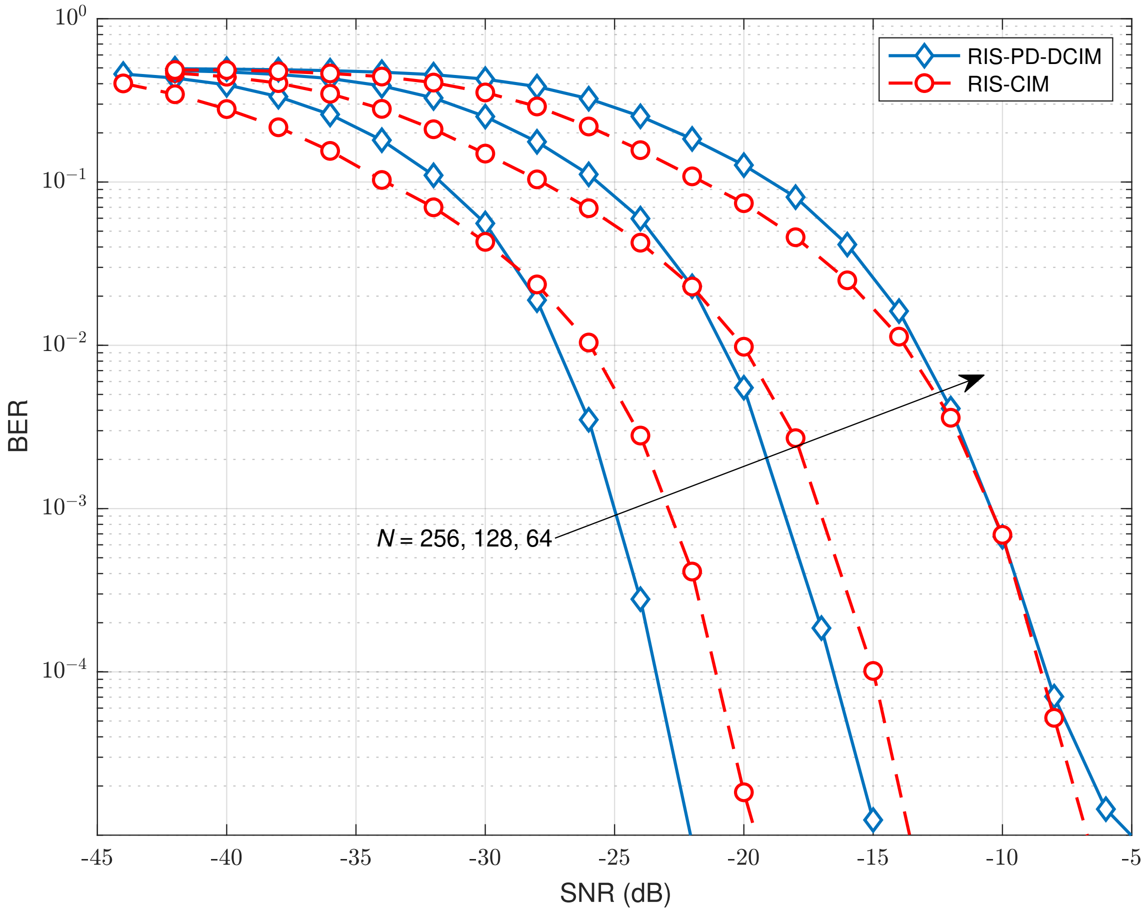

Figure 7.9: Error performance comparison of RIS-PD-DCIM with RIS-CIM for 10 bpcu varying N values.

7.6 Conclusion

In conclusion, this chapter has introduced the RIS-PD-DCIM scheme, a novel approach to enhancing spectral efficiency and error performance in wireless communication systems by leveraging the capabilities of RIS. By combining M-PAM modulation, spreading code indices, and an innovative RIS partitioning mechanism, the proposed scheme effectively exploits multiple dimensions of the transmission process. The unequal partitioning of the RIS, coupled with an additional phase shift, enables the encoding of information into the phase and power differences of the received signal components, significantly improving the system's information-carrying capacity.

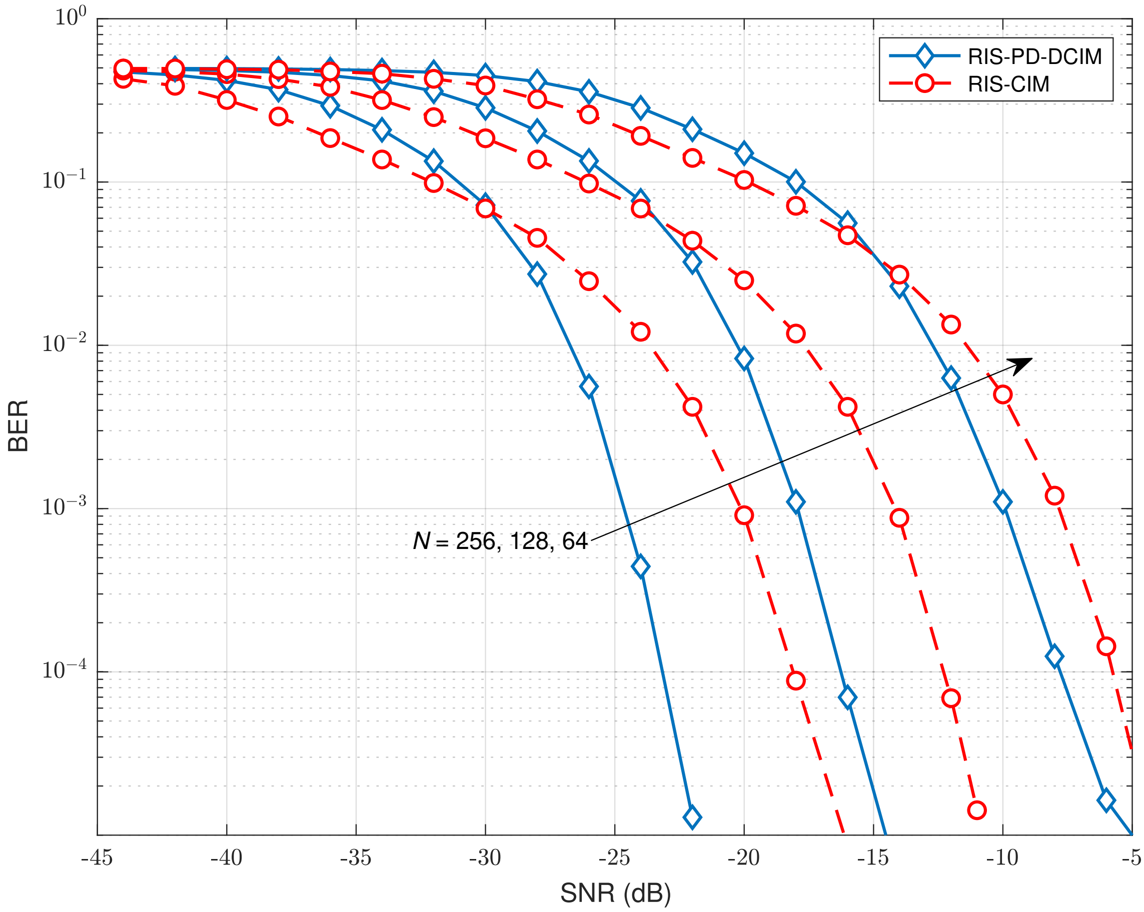

Figure 7.10: Error performance comparison of RIS-PD-DCIM with RIS-CIM for 12 bpcu and with varying N values.

Furthermore, the development of a LC detector addresses the computational challenges of decoding, making the RIS-PD-DCIM framework practical for real-time implementation and scalable to larger system configurations. Extensive simulations confirm the superiority of the proposed scheme in achieving higher spectral efficiency and reduced BER compared to existing methods under various system parameters. The RIS-PD-DCIM scheme not only highlights the potential of integrating RIS technology with advanced IM techniques but also provides a foundation for future innovations in next-generation wireless networks.

Chapter 8

CONCLUSION

This thesis investigates advanced OTA communication techniques leveraging RISs and their integration with emerging wireless technologies to enhance the efficiency of next-generation wireless communication networks. The primary objective is to develop novel system designs that improve spectral efficiency, BER performance, and overall system reliability, while also addressing the need for low complexity and practical feasibility, which are critical for 6G and beyond networks.

The proposed methodologies introduce RIS-assisted OTA virtual equalization, modulation, and multiple access schemes, optimizing the interaction between RIS and key technologies such as IM, NOMA, and hybrid RIS architectures. This research not only focuses on novel system designs and theoretical advancements and system performance enhancements but also explores practical considerations, including real-world deployment challenges, RIS hardware constraints, and scalability. Through system modeling, performance evaluation, and other analyses, this thesis provides a comprehensive framework that bridges innovative RIS-based communication techniques with their real-world applicability, contributing to the evolution of scalable, intelligent, and high-performance 6G communication networks.

8.1 Key Findings

The key findings of this thesis include:

- The proposed schemes, including RIS-aided OTA virtual equalization, hybrid RIS-aided OTA uplink-NOMA, RIS-PD-DCIM and OTA-RIS-IM, consistently demonstrated enhancements in spectral efficiency, BER performance, and system reliability, particularly in scenarios with frequency-selective fading, high interference, and power-limited conditions, without significantly increasing system complexity. These improvements highlight the effectiveness of RIS in optimizing wireless communication performance for 6G and beyond.

- The integration of RIS with IM techniques, particularly in hybrid RIS architectures and OTA modulation schemes, provided a significant boost in system performance. The proposed OTA-RIS-IM and E-OTA-RIS-IM techniques leveraged active, passive, and absorption modes at the RIS, allowing additional IM bits to be transmitted while maintaining high spectral efficiency and reliable error performance. This integration proved to be particularly effective in high-interference environments and complex fading channels.

- The introduction of low-complexity detectors across several schemes, such as RIS-PD-DCIM and hybrid RIS-based configurations, demonstrated that high-performance wireless communication can be achieved without the computational burden associated with ML detection methods. These findings underscore the feasibility of practical RIS deployments, where computational efficiency is a critical factor in real-world implementation.

- The user-controlled RIS system proposed in Chapter 5 introduced a network-independent RIS configuration, eliminating the need for centralized network control, physical backhaul connections, and extensive CSI acquisition. The implementation of an optimized codebook selection algorithm further enhanced the flexibility and adaptability of the system, making RIS deployment more feasible in practical scenarios where network dependency is a constraint.

- The RIS identification framework presented in Chapter 6 addressed critical issues and challenges in RIS-assisted wireless networks. The study proposed new research directions and explored potential RIS identification techniques, laying the foundation for RIS identification concept in RIS-enabled smart wireless environments.

- The power-differentiated dual-code index modulation (RIS-PD-DCIM) scheme in Chapter 7 successfully utilized unequal RIS partitioning, power differentiation, and spreading codes to maximize spectral efficiency while maintaining energy efficiency. By integrating low-complexity detection methods, the scheme ensured efficient modulation and data transmission, making it well-suited for low-power, high-performance 6G wireless communication systems.

These findings collectively highlight the potential of RIS in wireless communication systems, offering a scalable, efficient, and practical solution for next-generation networks. By addressing both theoretical and practical challenges, this research lays the groundwork for the seamless integration of RIS into future 6G deployments, enabling enhanced connectivity, reliability, and spectral efficiency in dynamic and interference-prone communication environments.

8.2 Future Directions

While this thesis has introduced several innovative RIS-aided communication techniques and system designs, many avenues for further research remain open. The proposed methods can be extended in various directions to enhance scalability, robustness, and real-world applicability, particularly for 6G and beyond wireless networks.

Chapter 2 explored RIS-aided over-the-air equalization, demonstrating its effectiveness in mitigating ISI and transforming frequency-selective channels into frequency-flat channels. Future research could expand this model to include scenarios where a direct link exists between the Tx and Rx, allowing for a more generalizable system design. Additionally, investigating alternative channel fading distributions, such as Rician fading, and analyzing the performance of multiple RIS deployments and mobile nodes would provide further insights into the practical feasibility and adaptability of RIS-aided ISI mitigation.

Chapter 3 introduced a hybrid RIS-aided uplink-NOMA system, where the RIS was partitioned into active and passive components to achieve power differentiation enabling NOMA OTA for the first time. Future directions could focus on dynamically varying the size of these partitions to further optimize system performance. Additionally, fine-tuning the alpha parameter, investigating optimal RIS placement strategies, and exploring alternative techniques to enhance NOMA performance under high-user-density and URLLC scenarios would further refine the proposed approach. Extending this work to incorporate multi-user and multi-RIS settings could also provide valuable insights into scalability and resource allocation in complex wireless environments.

Chapter 4 proposed OTA-RIS-IM and E-OTA-RIS-IM, which improved spectral efficiency and error performance through hybrid RIS architectures. Future research could explore the application of machine learning techniques for optimizing RIS configurations and IM bit transmission strategies dynamically. The introduction of MIMO architectures could also enhance performance by increasing the degrees of freedom available for spatial diversity and beamforming. Further, reducing the computational complexity of detection algorithms without compromising performance would be crucial for enabling real-time processing in practical 6G deployments.

Chapter 5 focused on improving the practicality of RIS deployment by introducing a network-independent user-controlled RIS system. Future work could extend this concept to outdoor and highly mobile environments, addressing user mobility challenges and ensuring seamless RIS operation across dynamic network conditions. The application of machine learning for intelligent beam control and adaptation could further enhance the effectiveness of user-controlled RIS. Additionally, exploring RIS-assisted localization techniques for enhanced indoor navigation, IoT applications, and smart city implementations would provide new opportunities for real-world deployment.

Chapter 6 addressed RIS identification and security, a crucial yet underexplored aspect of RIS-assisted networks. Future work should focus on scalable identification mechanisms that can support dense RIS deployments while minimizing overhead and complexity. Optimizing the identification period to balance latency and throughput, mitigating misidentification errors in multi-RIS zones, and developing multi-domain identification techniques that leverage time, frequency, power, and spatial characteristics could significantly enhance RIS security and network efficiency. Additionally, deep learning-based classification models could be explored for real-time RIS authentication and interference management in dynamic wireless environments.

Chapter 7 introduced RIS-PD-DCIM, a novel modulation technique that leveraged power differentiation, phase shifts, spreading codes, and M-PAM symbols to improve spectral efficiency and energy efficiency. Future research could investigate adaptive RIS partitioning strategies, where RIS elements dynamically switch between active, passive, and hybrid modes based on channel conditions. The extension of RIS-PD-DCIM to multi-user and multi-RIS scenarios would provide valuable insights into its feasibility for large-scale network deployments. Additionally, exploring low-power implementations optimized for battery-operated devices and IoT networks would make the scheme more adaptable to energy-constrained environments.

Beyond these chapter-specific future directions, there are several other research opportunities. The integration of RIS with advanced AI-driven network optimization, including deep reinforcement learning for dynamic beamforming, power control, and adaptive RIS configuration, presents a promising direction. Further, exploring RIS-aided ISAC systems, where RIS serves both as a communication enhancer and environmental sensor, could revolutionize applications in autonomous driving, smart healthcare, and industrial automation. Finally, investigating the economic and practical deployment challenges of RIS-assisted networks, including cost-benefit analyses, hardware limitations, and large-scale network planning, will be crucial for the successful real-world adoption of RIS in 6G. Addressing these challenges and research gaps will further advance RIS technology, ensuring its seamless integration into next-generation wireless networks while enhancing spectral efficiency, system reliability, and practical feasibility.

8.3 Conclusion

This thesis has introduced a series of innovative RIS-aided communication schemes that leverage the capabilities of RIS, IM, and their integration with complementary technologies to enhance the performance of next-generation wireless communication systems. Through detailed theoretical analysis, extensive simulations, and performance evaluations, it has been demonstrated that the proposed RIS-assisted equalization, modulation, and access schemes significantly improve spectral efficiency, BER performance, and system reliability while maintaining low complexity and practical feasibility.

The exploration of RIS-assisted over-the-air equalization, hybrid RIS-based uplink NOMA, and novel RIS-enabled modulation techniques presents a promising pathway for the evolution of wireless networks, particularly 6G, where scalability, adaptability, and energy efficiency are crucial design considerations. The integration of low-complexity detection methods, dynamic RIS configurations, and network-independent RIS architectures further enhances the practicality of these solutions, making them well-suited for real-world deployments in dense, interference-prone, and mobility-constrained environments.

The findings of this research contribute to both the theoretical advancement and practical implementation of RIS in next-generation communication systems. By addressing key challenges in wireless communication, including ISI suppression, efficient resource allocation, and RIS identification, this work lays a strong foundation for the seamless adoption of RIS-aided networks in 6G and beyond, ensuring high-performance, scalable, and energy-efficient wireless connectivity.

8.4 Publications Derived from This Thesis

The following research papers have been published or submitted for publication as a result of the work conducted in this thesis:

- Arslan, E., Yildirim, I., Kilinc, F., Basar, E. (2022). Over-the-air equalization with reconfigurable intelligent surfaces. IET Communications, 16(13), 1486-1497.

- Arslan, E., Kilinc, F., Arzykulov, S., Dogukan, A. T., Celik, A., Basar, E., Eltawil, A. M. (2022). Reconfigurable intelligent surface enabled over-the-air uplink NOMA. IEEE Transactions on Green Communications and Networking, 7(2), 814-826.

- Arslan, E., Kilinc, F., Basar, E., Arslan, H. (2023, November). Network-independent and user-controlled RIS: An experimental perspective. In 2023 26th International Symposium on Wireless Personal Multimedia Communications (WPMC) (pp. 1-6). IEEE.

- Arslan, E., Dogukan, A. T., Kilinc, F., Basar, E. (2024, July). Hybrid Reconfigurable Intelligent Surface Enabled Over-the-Air Index-Modulation. In 2024 6th International Conference on Communications, Signal Processing, and their Applications (ICCSPA) (pp. 1-6). IEEE.

- Arslan, E., Dogukan, A. T., Kilinc, F., Coskun, A. F., Basar, E. (2024). Reconfigurable Intelligent Surface Identification in Mobile Networks: Opportunities and Challenges. IEEE Wireless Communications Magazine.

- Arslan, E., Dogukan, A. T., Basar, E. (2025, March). "RIS-Aided Power-Differentiated Dual-Code Index Modulation" has been submitted to IEEE Transactions on Green Communications and Networking and is Under Review.

Bibliography

[3rd,] 3rd Generation Partnership Project; Technical specification group radio access network; evolved universal terrestrial radio access (E-UTRA); further advancements for E-UTRA physical layer aspects (release 9).

[GW,] Greenerwave 2022, 35 rue du sentier, 75002 paris, france.

[202, 2023] (2023). ”6G communications: Materials and hardware markets and technology 2024-2044”. *Zhar Research, UK.*

[ETS, 2023a] (2023a). ETSI GR RIS 001 V1.1.1 - Reconfigurable intelligent surfaces (RIS); use cases, deployment scenarios and requirements.

[ETS, 2023b] (2023b). ETSI GR RIS 003 V1.1.1 - Reconfigurable intelligent surfaces (RIS); communication models, channel models, channel estimation and evaluation methodology.

[3GP, 2024] (2024). 3GPP TR 38.858 V18.1.0 - Study on evolution of NR duplex operation.

[Abdallah et al., 2022] Abdallah, A., Celik, A., Mansour, M. M., and Eltawil, A. (2022). RIS-aided mmwave MIMO channel estimation using deep learning and compressive sensing.

[Ai et al., 2021] Ai, Y., Felipe, A., Kong, L., Cheffena, M., Chatzinotas, S., and Ottersten, B. (2021). Secure vehicular communications through reconfigurable intelligent surfaces. *IEEE Transactions on Vehicular Technology*, 70(7):7272–7276.

[Alamzadeh et al., 2021] Alamzadeh, I., Alexandropoulos, G. C., Shlezinger, N., and Imani, M. F. (2021). A reconfigurable intelligent surface with integrated sensing capability. *Scientific reports*, 11(1):20737.

[Alayasra and Arslan, 2022] Alayasra, M. and Arslan, H. (2022). IRS-enabled beam-space channel. *IEEE Trans. Wirel. Commun.*, 21(6):3822–3835.

[Alfattani et al., 2021] Alfattani, S., Jaafar, W., Hmamouche, Y., Yanikomeroglu, H., Yongacoglu, A., Dao, N. D., and Zhu, P. (2021). Aerial platforms with reconfigurable smart surfaces for 5G and beyond. *IEEE Commun. Mag.*, 59(1):96–102.

[Araghi et al., 2022] Araghi, A., Khalily, M., Safaei, M., Bagheri, A., Singh, V., Wang, F., and Tafazolli, R. (2022). Reconfigurable intelligent surface (RIS) in the sub-6 GHz band: Design, implementation, and real-world demonstration. *IEEE Access*, 10:2646–2655.

[Arslan et al., 2020a] Arslan, E., Dogukan, A. T., and Basar, E. (2020a). Index modulation-based flexible non-orthogonal multiple access. *IEEE Wirel. Commun. Lett.*, 9(11):1942–1946.

[Arslan et al., 2020b] Arslan, E., Dogukan, A. T., and Basar, E. (2020b). Sparse-encoded codebook index modulation. *IEEE Trans. Veh. Technol.*, 69(8):9126–9130.

[Arslan et al., 2024] Arslan, E., Dogukan, A. T., Kilinc, F., and Basar, E. (2024). Hybrid reconfigurable intelligent surface enabled over-the-air index-modulation. In *2024 6th Int. Conf. Commun., Signal Process., and their Appl. (ICCSPA)*, pages 1–6. IEEE.

[Arslan et al., 2025] Arslan, E., Dogukan, A. T., Kilinc, F., Coskun, A. F., and Basar, E. (2025). Reconfigurable intelligent surface identification in mobile networks: Opportunities and challenges. *IEEE Commun. Mag.*

[Arslan et al., 2022a] Arslan, E., Kilinc, F., Arzykulov, S., Dogukan, A. T., Celik, A., Basar, E., and Eltawil, A. M. (2022a). Reconfigurable intelligent surface enabled over-the-air uplink NOMA. *IEEE Trans. on Green Commun. and Netw.*

[Arslan et al., 2023a] Arslan, E., Kilinc, F., Basar, E., and Arslan, H. (2023a). Network-independent and user-controlled RIS: An experimental perspective. In *Proc. 26th Int. Symp. Wireless Pers. Multimedia Commun. (WPMC)*, pages 1–6. IEEE.

[Arslan et al., 2023b] Arslan, E., Kilinc, F., Basar, E., and Arslan, H. (2023b). Network-independent and user-controlled RIS: An experimental perspective. In *2023 26th Int. Symposium on Wirel. Pers. Multimedia Commun. (WPMC)*, pages 1–6.

[Arslan et al., 2021] Arslan, E., Yildirim, I., Kilinc, F., and Basar, E. (2021). Over-the-air equalization with reconfigurable intelligent surfaces. *IET Commun.*, 16:1486–1497.

[Arslan et al., 2022b] Arslan, E., Yildirim, I., Kilinc, F., and Basar, E. (2022b). Over-the-air equalization with reconfigurable intelligent surfaces. *IET Commun.*, 16(13):1486–1497.

[Asmoro and Shin, 2022] Asmoro, K. and Shin, S. Y. (2022). RIS grouping based index modulation for 6G telecommunications. *IEEE Wirel. Commun. Lett.*, 11(11):2410–2414.

[Aygül et al., 2021] Aygül, M. A., Nazzal, M., and Arslan, H. (2021). Deep learning-based optimal RIS interaction exploiting previously sampled channel correlations. In *2021 IEEE Wirel. Commun. Netw. Conf. (WCNC)*, pages 1–6. IEEE.

[Ayoubi et al., 2023] Ayoubi, R. A., Mizmizi, M., Tagliaferri, D., De Donno, D., and Spagnolini, U. (2023). Network-controlled repeaters vs. reconfigurable intelligent surfaces for 6G mmw coverage extension: A simulative comparison. In *2023 21st*

Mediterranean Commun. and Comput. Netw.g Conf. (MedComNet), pages 196–202.

[Basar, 2016] Basar, E. (2016). Index modulation techniques for 5G wireless networks. *IEEE Commun. Mag.*, 54(7):168–175.

[Basar, 2019] Basar, E. (2019). Transmission through large intelligent surfaces: A new frontier in wireless communications. In *Proc. 2019 European Conf. Netw. and Commun. (EuCNC)*, pages 112–117. IEEE.

[Basar, 2020a] Basar, E. (2020a). Reconfigurable intelligent surface-based index modulation: A new beyond MIMO paradigm for 6G. *IEEE Trans. Commun.*, 68(5):3187–3196.

[Basar, 2020b] Basar, E. (2020b). Reconfigurable intelligent surface-based index modulation: A new beyond MIMO paradigm for 6G. *IEEE Trans. Commun.*, 68(5):3187–3196.

[Basar, 2021] Basar, E. (2021). Reconfigurable intelligent surfaces for Doppler effect and multipath fading mitigation. *Frontiers in Commun. and Netw. (to appear).*

[Basar et al., 2023] Basar, E., Alexandropoulos, G. C., Liu, Y., Wu, Q., Jin, S., Yuen, C., Dobre, O. A., and Schober, R. (2023). Reconfigurable intelligent surfaces for 6G: Emerging hardware architectures, applications, and open challenges. *arXiv:2312.16874, (to appear in IEEE Veh. Tech. Mag.) DOI: 10.1109/MVT.2024.3415570).*

[Başar et al., 2013] Başar, E., Aygölü, Ü., Panayırcı, E., and Poor, H. V. (2013). Orthogonal frequency division multiplexing with index modulation. *IEEE Trans. Signal Process.*, 61(22):5536–5549.

[Basar et al., 2019] Basar, E., Di Renzo, M., De Rosny, J., Debbah, M., Alouini, M.-S., and Zhang, R. (2019). Wireless communications through reconfigurable intelligent surfaces. *IEEE Access*, 7:116753–116773.

[Basar and Poor, 2021] Basar, E. and Poor, H. V. (2021). Present and future of reconfigurable intelligent surface-empowered communications [perspectives]. *IEEE Signal Proc. Mag.*, 38(6):146–152.

[Basar et al., 2017] Basar, E., Wen, M., Mesleh, R., Di Renzo, M., Xiao, Y., and Haas, H. (2017). Index modulation techniques for next-generation wireless networks. *IEEE Access*, 5:16693–16746.

[Basar and Yildirim, 2021] Basar, E. and Yildirim, I. (2021). Reconfigurable intelligent surfaces for future wireless networks: A channel modeling perspective. *IEEE Wireless Commun. (to appear).*

[Basharat et al., 2021] Basharat, S., Hassan, S. A., Pervaiz, H., Mahmood, A., Ding, Z., and Gidlund, M. (2021). Reconfigurable intelligent surfaces: Potentials, applications, and challenges for 6G wireless networks. *IEEE Wirel. Commun.*, 28(6):184–191.

[Cheng et al., 2018] Cheng, X., Zhang, M., Wen, M., and Yang, L. (2018). Index modulation for 5G: Striving to do more with less. *IEEE Wirel. Commun.*, 25(2):126–132.

[Cheng et al., 2021] Cheng, Y., Li, K. H., Liu, Y., Teh, K. C., and Poor, H. V. (2021). Downlink and uplink intelligent reflecting surface aided networks: NOMA and OMA. *IEEE Trans. Wirel. Commun.*, 20(6):3988–4000.

[Chowdhury et al., 2020] Chowdhury, M. Z., Shahjalal, M., Ahmed, S., and Jang, Y. M. (2020). 6G wireless communication systems: Applications, requirements, technologies, challenges, and research directions. *IEEE Open J. Commun. Soc.*, 1:957–975.

[Cogen et al., 2024] Cogen, F., Ozden, B. A., Aydin, E., and Kabaoglu, N. (2024). Reconfigurable intelligent surface-empowered code index modulation for high-rate SISO systems. *IEEE Trans. Cognitive Commun. and Netw.*

[Dash et al., 2022] Dash, S. P., Mallik, R. K., and Pandey, N. (2022). Performance analysis of an index modulation-based receive diversity RIS-assisted wireless communication system. *IEEE Commun. Lett.*, 26(4):768–772.

[Di Renzo et al., 2020] Di Renzo, M., Ntontin, K., Song, J., Danufane, F. H., Qian, X., Lazarakis, F., De Rosny, J., Phan-Huy, D.-T., Simeone, O., Zhang, R., Debbah, M., Lerosey, G., Fink, M., Tretyakov, S., and Shamai, S. (2020). Reconfigurable intelligent surfaces vs. relaying: Differences, similarities, and performance comparison. *IEEE Open J. Commun. Soc.*, 1:798–807.

[Ding and Poor, 2020] Ding, Z. and Poor, H. V. (2020). A simple design of IRS-NOMA transmission. *IEEE Commun. Lett.*, 24(5):1119–1123.

[Ding et al., 2020] Ding, Z., Schober, R., and Poor, H. V. (2020). On the impact of phase shifting designs on IRS-NOMA. *IEEE Wirel. Commun. Lett.*, 9(10):1596–1600.

[Doğan-Tusha et al., 2020] Doğan-Tusha, S., Arslan, H., et al. (2020). 6G vision: An ultra-flexible perspective. *ITU J. on Future and Evol. Tech.*, 1(9):1–20.

[Dogukan et al., 2024] Dogukan, A. T., Arslan, E., Pihtili, M. E., and Basar, E. (2024). RIS-aided enhanced receive spatial modulation. *IEEE Wirel. Commun. Lett.*

[Drakshayini and Kounte, 2022a] Drakshayini, M. and Kounte, M. R. (2022a). A review of wireless channel estimation techniques: challenges and solutions. *International Journal of Wireless and Mobile Computing*, 23(2):193–203.

[Drakshayini and Kounte, 2022b] Drakshayini, M. and Kounte, M. R. (2022b). A review of wireless channel estimation techniques: challenges and solutions. *International Journal of Wireless and Mobile Computing*, 23(2):193–203.

[Dwivedi et al., 2021] Dwivedi, S., Shreevastav, R., Munier, F., Nygren, J., Siomina, I., Lyazidi, Y., Shrestha, D., Lindmark, G., Ernström, P., Stare, E., Razavi, S. M., Muruganathan, S., Masini, G., Busin, , and Gunnarsson, F. (2021). Positioning in 5g networks. *IEEE Communications Magazine*, 59(11):38–44.

[El-Mossallamy et al., 2020] El-Mossallamy, M. A., Zhang, H., Song, L., Seddik, K. G., Han, Z., and Li, G. Y. (2020). Reconfigurable intelligent surfaces for wireless communications: Principles, challenges, and opportunities. *IEEE Trans. Cogn. Commun. Netw.*, 6(3):990–1002.

[ElMossallamy et al., 2021] ElMossallamy, M. A., Seddik, K. G., Chen, W., Wang, L., Li, G. Y., and Han, Z. (2021). RIS optimization on the complex circle manifold for interference mitigation in interference channels. *IEEE Trans. Veh. Technol.*, 70(6):6184–6189.

[ETSI, 2023] ETSI (2023). Reconfigurable intelligent surfaces (RIS); use cases, deployment scenarios and requirements. Technical Report ETSI GR RIS 001 V1.1.1, European Telecommunications Standards Institute (ETSI).

[Fu et al., 2019] Fu, M., Zhou, Y., and Shi, Y. (2019). Intelligent reflecting surface for downlink non-orthogonal multiple access networks. In *2019 IEEE Globecom Workshops (GC Wkshps)*, pages 1–6. IEEE.

[Gacanin and Di Renzo, 2020] Gacanin, H. and Di Renzo, M. (2020). Wireless 2.0: Toward an intelligent radio environment empowered by reconfigurable meta-surfaces and artificial intelligence. *IEEE Veh. Technol. Mag.*, 15(4):74–82.

[Gevez et al., 2024] Gevez, Y., Arslan, E., and Basar, E. (2024). A supervised learning-assisted partitioning solution for RIS-aided NOMA systems. *IEEE Trans. Cogn. Commun. and Netw.*

[Haider and Hwang, 2019] Haider, A. and Hwang, S.-H. (2019). Maximum transmit power for UE in an LTE small cell uplink. *Electronics*, 8(7):796.

[Heath Jr, 2017] Heath Jr, R. W. (2017). *Introduction to Wireless Digital Communication: A Signal Processing Perspective*. Prentice Hall.

[Hemanth et al., 2020] Hemanth, A., Umamaheswari, K., Pogaku, A. C., Do, D.-T., and Lee, B. M. (2020). Outage performance analysis of reconfigurable intelligent surfaces-aided NOMA under presence of hardware impairment. *IEEE Access*, 8:212156–212165.

[Hong et al., 2020] Hong, S., Pan, C., Ren, H., Wang, K., and Nallanathan, A. (2020). Artificial-noise-aided secure MIMO wireless communications via intelligent reflecting surface. *IEEE Trans. Commun.*, 68(12):7851–7866.

[Hou et al., 2020] Hou, T., Liu, Y., Song, Z., Sun, X., Chen, Y., and Hanzo, L. (2020). Reconfigurable intelligent surface aided NOMA networks. *IEEE J. Sel. Areas Commun.*, 38(11):2575–2588.

[Hu et al., 2021] Hu, C., Dai, L., Han, S., and Wang, X. (2021). Two-timescale channel estimation for reconfigurable intelligent surface aided wireless communications. *IEEE Trans. Commun.*, 69(11):7736–7747.

[Hua et al., 2021a] Hua, S., Zhou, Y., Yang, K., Shi, Y., and Wang, K. (2021a). Reconfigurable intelligent surface for green edge inference. *IEEE Trans. Green Commun. Netw.*, 5(2):964–979.

[Hua et al., 2021b] Hua, S., Zhou, Y., Yang, K., Shi, Y., and Wang, K. (2021b). Reconfigurable intelligent surface for green edge inference. *IEEE Trans. on Green Commun. and Netw.*, 5(2):964–979.

[Huang et al., 2019a] Huang, C., Alexandropoulos, G. C., Yuen, C., and Debbah, M. (2019a). Indoor signal focusing with deep learning designed reconfigurable intelligent surfaces. In *Proc. 2019 IEEE 20th Int. Workshop Sig. Process. Advances in Wireless Commun. (SPAWC)*, pages 1–5.

[Huang et al., 2019b] Huang, C., Alexandropoulos, G. C., Yuen, C., and Debbah, M. (2019b). Indoor signal focusing with deep learning designed reconfigurable intelligent surfaces. In *IEEE Workshop Signal Process. Adv. Wirel. Commun. (SPAWC).*, pages 1–5. IEEE.

[Huang et al., 2020a] Huang, C., Hu, S., Alexandropoulos, G. C., Zappone, A., Yuen, C., Zhang, R., Di Renzo, M., and Debbah, M. (2020a). Holographic MIMO surfaces for 6G wireless networks: Opportunities, challenges, and trends. *IEEE Wireless Commun.*, 27(5):118–125.

[Huang et al., 2020b] Huang, C., Hu, S., Alexandropoulos, G. C., Zappone, A., Yuen, C., Zhang, R., Renzo, M. D., and Debbah, M. (2020b). Holographic MIMO surfaces for 6G wireless networks: Opportunities, challenges, and trends. *IEEE Wirel. Commun.*, 27(5):118–125.

[Huang et al., 2019c] Huang, C., Zappone, A., Alexandropoulos, G. C., Debbah, M., and Yuen, C. (2019c). Reconfigurable intelligent surfaces for energy efficiency in wireless communication. *IEEE Trans. Wirel. Commun.*, 18(8):4157–4170.

[Huang et al., 2019d] Huang, C., Zappone, A., Alexandropoulos, G. C., Debbah, M., and Yuen, C. (2019d). Reconfigurable intelligent surfaces for energy efficiency in wireless communication. *IEEE Trans. on Wireless Commun.*, 18(8):4157–4170.

[Jiang and Liu, 2016] Jiang, D. and Liu, G. (2016). An overview of 5g requirements. *5G Mobile Communications*, pages 3–26.

[Jin et al., 2024] Jin, J., Jin, X., Wen, M., Song, M., Huang, C., and Yao, Y. (2024). Active fully-connected RIS based on index modulation for high rate and energy-efficient systems. *IEEE Trans. Commun.*

[Jin et al., 2023] Jin, X., Bian, L., Li, Z., Xing, S., and Wen, M. (2023). A novel RIS-aided code index modulation scheme with low-complexity detection. *IEEE Trans. Veh. Technol.*, 72(11):14279–14288.

[Kaddoum et al., 2015] Kaddoum, G., Nijsure, Y., and Tran, H. (2015). Generalized code index modulation technique for high-data-rate communication systems. *IEEE Trans. Veh. Technol.*, 65(9):7000–7009.

[Kayraklık et al., 2022] Kayraklık, S., Yildirim, I., Gevez, Y., Basar, E., and Görçin, A. (2022). Indoor coverage enhancement for RIS-assisted communication systems: Practical measurements and efficient grouping. *arXiv preprint arXiv:2211.07188*.

[Khaleel et al., 2024] Khaleel, A., Vural, R., Ilter, M. C., Gerami, M., and Basar, E. (2024). A simple detection and identification scheme for reconfigurable intelligent surfaces. *arXiv preprint arXiv:2402.12565*.

[Khalid et al., 2023] Khalid, W., Rehman, M. A. U., Van Chien, T., Kaleem, Z., Lee, H., and Yu, H. (2023). Reconfigurable intelligent surface for physical layer security in 6G-IoT: Designs, issues, and advances. *IEEE Internet of Things Journal*, 11(2):3599–3613.

[Kilinc et al., 2021a] Kilinc, F., Yildirim, I., and Basar, E. (2021a). Physical channel modeling for RIS-empowered wireless networks in sub-6 ghz bands. *arXiv preprint arXiv:2111.01537*.

[Kilinc et al., 2021b] Kilinc, F., Yildirim, I., and Basar, E. (2021b). Physical channel modeling for RIS-empowered wireless networks in sub-6 GHz bands. In *2021 55th Asilomar Conf. on Signals, Syst., and Comput.*, pages 704–708.

[Li et al., 2021] Li, H., Cai, W., Liu, Y., Li, M., Liu, Q., and Wu, Q. (2021). Intelligent reflecting surface enhanced wideband MIMO-OFDM communications: From practical model to reflection optimization. *IEEE Trans. Commun.*, pages 1–1.

[Li et al., 2023] Li, Q., Bai, S., Wen, M., and Huang, D. (2023). RIS-based code index modulation for joint active/passive transmission. *IEEE Trans. Veh. Technol.*

[Li et al., 2020] Li, S., Duo, B., Yuan, X., Liang, Y.-C., and Di Renzo, M. (2020). Reconfigurable intelligent surface assisted UAV communication: Joint trajectory design and passive beamforming. *IEEE Wireless Commun. Lett.*, 9(5):716–720.

[Li et al., 2022] Li, X., Xie, Z., Huang, G., Zhang, J., Zeng, M., and Chu, Z. (2022). Sum rate maximization for RIS-aided NOMA with direct links. *IEEE Netw. Lett.*, 4(2):55–58.

[Lin et al., 2020] Lin, S., Zheng, B., Alexandropoulos, G. C., Wen, M., and *et al.*, C. (2020). Adaptive transmission for reconfigurable intelligent surface-assisted OFDM wireless communications. *IEEE J. Sel. Areas Commun.*, 38(11):2653–2665.

[Liu et al., 2022a] Liu, R., Wu, Q., Di Renzo, M., and Yuan, Y. (2022a). A path to smart radio environments: An industrial viewpoint on reconfigurable intelligent surfaces. *IEEE Wireless Communications*, 29(1):202–208.

[Liu et al., 2021] Liu, Y., Liu, X., Mu, X., Hou, T., Xu, J., Di Renzo, M., and Al-Dhahir, N. (2021). Reconfigurable intelligent surfaces: Principles and opportunities. *IEEE Commun. Surveys & Tuts.*, 23(3):1546–1577.

[Liu et al., 2022b] Liu, Y., Mu, X., Liu, X., Di Renzo, M., Ding, Z., and Schober, R. (2022b). Reconfigurable intelligent surface-aided multi-user networks: Interplay between noma and ris. *IEEE Wireless Communications*, 29(2):169–176.

[Luong et al., 2018] Luong, T. V., Ko, Y., and Choi, J. (2018). Repeated MCIK-OFDM with enhanced transmit diversity under CSI uncertainty. *IEEE Trans. Wirel. Commun.*, 17(6):4079–4088.

[Ma et al., 2020] Ma, T., Xiao, Y., Lei, X., Xiong, W., and Ding, Y. (2020). Indoor localization with reconfigurable intelligent surface. *IEEE Commun. Lett.*, 25(1):161–165.

[Mao et al., 2018] Mao, T., Wang, Q., Wang, Z., and Chen, S. (2018). Novel index modulation techniques: A survey. *IEEE Commun. Surv. Tutor.*, 21(1):315–348.

[Mao et al., 2016] Mao, T., Wang, Z., Wang, Q., Chen, S., and Hanzo, L. (2016). Dual-mode index modulation aided OFDM. *IEEE Access*, 5:50–60.

[Mathai and Provost, 1992a] Mathai, A. and Provost, S. (1992a). *Quadratic Forms in Random Variables: Theory and Applications*, volume 87.

[Mathai and Provost, 1992b] Mathai, A. and Provost, S. B. (1992b). *Quadratic Forms in Random Variables: Theory and Applications.* New York, NY, USA: Marcel Dekker.

[Matthiesen et al., 2020] Matthiesen, B., Björnson, E., De Carvalho, E., and Popovski, P. (2020). Intelligent reflecting surface operation under predictable receiver mobility: A continuous time propagation model. *IEEE Wireless Commun. Lett.*, 10(2):216–220.

[Melgarejo et al., 2020] Melgarejo, D. C., Kalalas, C., de Sena, A. S., Nardelli, P. H., and Fraidenraich, G. (2020). Reconfigurable intelligent surface-aided grant-free access for uplink URLLC. In *2020 2nd 6G Wirel. Summit (6G SUMMIT)*, pages 1–5. IEEE.

[Mu et al., 2019] Mu, X., Liu, Y., Guo, L., Lin, J., and Al-Dhahir, N. (2019). Exploiting intelligent reflecting surfaces in multi-antenna aided NOMA systems. *arXiv preprint arXiv:1910.13636*, pages 0090–6778.

[Niu et al., 2022] Niu, H., Lin, Z., Chu, Z., Zhu, Z., Xiao, P., Nguyen, H. X., Lee, I., and Al-Dhahir, N. (2022). Joint beamforming design for secure ris-assisted iot networks. *IEEE internet of things journal*, 10(2):1628–1641.

[Ozden et al., 2024] Ozden, B. A., Cogen, F., Aydin, E., Ilhan, H., Basar, E., and Wen, M. (2024). A novel reconfigurable intelligent surface-supported code index modulation-based receive spatial modulation system. In *2024 IEEE Wirel. Commun. and Netw. Conf. (WCNC)*, pages 1–6. IEEE.

[Pan et al., 2021] Pan, C., Ren, H., Wang, K., Kolb, J. F., Elkashlan, M., Chen, M., Di Renzo, M., Hao, Y., Wang, J., Swindlehurst, A. L., et al. (2021). Reconfigurable intelligent surfaces for 6G systems: Principles, applications, and research directions. *IEEE Commun. Mag.*, 59(6):14–20.

[Pei et al., 2021a] Pei, X., Yin, H., Tan, L., Cao, L., Li, Z., Wang, K., Zhang, K., and Björnson, E. (2021a). RIS-aided wireless communications: Prototyping, adaptive beamforming, and indoor/outdoor field trials. *IEEE Trans. on Commun.*, 69(12):8627–8640.

[Pei et al., 2021b] Pei, X., Yin, H., Tan, L., Cao, L., Li, Z., Wang, K., Zhang, K., and Björnson, E. (2021b). RIS-aided wireless communications: Prototyping, adaptive beamforming, and indoor/outdoor field trials. *IEEE Trans. on Commun.*, 69(12):8627–8640.

[Perović et al., 2020] Perović, N. S., Di Renzo, M., and Flanagan, M. F. (2020). Channel capacity optimization using reconfigurable intelligent surfaces in indoor mmwave environments. In *Proc. IEEE Int. Conf. on Commun. (ICC)*, pages 1–7. IEEE.

[Perović et al., 2020] Perović, N. S., Renzo, M. D., and Flanagan, M. F. (2020). Channel capacity optimization using reconfigurable intelligent surfaces in indoor mmwave environments. In *ICC 2020 - 2020 IEEE Int. Conf. Commun. (ICC)*, pages 1–7.

[Popov, 2021] Popov, V. e. a. (2021). Experimental demonstration of a mmwave passive access point extender based on a binary reconfigurable intelligent surface. *Frontiers in Communications*, 2.

[Pradhan et al., 2020] Pradhan, C., Li, A., Song, L., Li, J., Vucetic, B., and Li, Y. (2020). Reconfigurable intelligent surface (RIS)-enhanced two-way OFDM communications. *IEEE Trans. Veh. Technol.*, 69(12):16270–16275.

[Rains et al., 2022] Rains, J., Tukmanov, A., Cui, T. J., Zhang, L., Abbasi, Q. H., Imran, M. A., et al. (2022). High-resolution programmable scattering for wireless coverage enhancement: an indoor field trial campaign. *IEEE Trans. on Antennas and Propag.*, 71(1):518–530.

[Rappaport et al., 2019] Rappaport, T. S., Xing, Y., Kanhere, O., Ju, S., Madanayake, A., Mandal, S., Alkhateeb, A., and Trichopoulos, G. C. (2019). Wireless communications and applications above 100 GHz: Opportunities and challenges for 6G and beyond. *IEEE Access*, 7:78729–78757.

[Ren et al., 2023] Ren, Y., Zhou, R., Teng, X., Meng, S., Zhou, M., Tang, W., Li, X., Li, C., and Jin, S. (2023). On deployment position of RIS in wireless communication systems: Analysis and experimental results. *IEEE Wirel. Commun. Lett.*, 12(10):1756–1760.

[Saad et al., 2020] Saad, W., Bennis, M., and Chen, M. (2020). A vision of 6G wireless systems: Applications, trends, technologies, and open research problems. *IEEE Netw.*, 34(3):134–142.

[Sahin et al., 2021] Sahin, M. M., Erol, I. G., Arslan, E., Basar, E., and Arslan, H. (2021). OFDM-IM for joint communication and radar-sensing: A promising waveform for dual functionality. *Front. Commus. Net.*, 2:34.

[Şahin et al., 2021] Şahin, M. M., Gurol, I. E., Arslan, E., Basar, E., and Arslan, H. (2021). OFDM-IM for joint communication and radar-sensing: a promising waveform for dual functionality. *Front. Commun. Netw.*, 2:715944.

[Shin et al., 2007] Shin, C., Heath, R. W., and Powers, E. J. (2007). Blind channel estimation for mimo-ofdm systems. *IEEE Transactions on Vehicular Technology*, 56(2):670–685.

[Simeone et al., 2004] Simeone, O., Bar-Ness, Y., and Spagnolini, U. (2004). Pilot-based channel estimation for ofdm systems by tracking the delay-subspace. *IEEE transactions on wireless communications*, 3(1):315–325.

[Simon, 2002] Simon, M. K. (2002). *Probability distributions involving Gaussian random variables: A handbook for engineers and scientists*. Springer.

[Simon, 2007] Simon, M. K. (2007). *Probability Distributions Involving Gaussian Random Variables: A Handbook for Engineers and Scientists*. Springer Science & Business Media.

[Su et al., 2020a] Su, R., Dai, L., Tan, J., Hao, M., and MacKenzie, R. (2020a). Capacity enhancement for irregular reconfigurable intelligent surface-aided wireless communications. In *GLOBECOM 2020 - 2020 IEEE Glob. Commun. Conf.*, pages 1–6.

[Su et al., 2020b] Su, R., Dai, L., Tan, J., Hao, M., and MacKenzie, R. (2020b). Capacity enhancement for irregular reconfigurable intelligent surface-aided wireless communications. In *Proc. IEEE Global Commun. Conf.*, pages 1–6. IEEE.

[Subrt and Pechac, 2012] Subrt, L. and Pechac, P. (2012). Controlling propagation environments using intelligent walls. In *2012 6th Eur. Conf. on Antennas and Propag. (EUCAP)*, pages 1–5. IEEE.

[Sugiura et al., 2017] Sugiura, S., Ishihara, T., and Nakao, M. (2017). State-of-the-art design of index modulation in the space, time, and frequency domains: Benefits and fundamental limitations. *IEEE Access*, 5:21774–21790.

[Tan et al., 2016] Tan, X., Sun, Z., Jornet, J. M., and Pados, D. (2016). Increasing indoor spectrum sharing capacity using smart reflect-array. In *2016 IEEE Int. Conf. Commun. (ICC)*, pages 1–6. IEEE.

[Tang et al., 2020] Tang, W., Dai, J. Y., Chen, M. Z., Wong, K.-K., Li, X., Zhao, X., Jin, S., Cheng, Q., and Cui, T. J. (2020). MIMO transmission through reconfigurable intelligent surface: System design, analysis, and implementation. *IEEE J. Sel. Areas Commun.*, 38(11):2683–2699.

[Tapio et al., 2021a] Tapio, V., Shojaeifard, A., Hemadeh, I., Mourad, A., and Juntti, M. (2021a). Reconfigurable intelligent surface for 5G NR uplink coverage enhancement. In *2021 IEEE 94th Veh. Technol. Conf. (VTC2021-Fall)*, pages 1–5.

[Tapio et al., 2021b] Tapio, V., Shojaeifard, A., Hemadeh, I., Mourad, A., and Juntti, M. (2021b). Reconfigurable intelligent surface for 5G NR uplink coverage enhancement. In *2021 IEEE 94th Veh. Technol. Conf. (VTC2021-Fall)*, pages 1–5.

[Tasci et al., 2022a] Tasci, R. A., Kilinc, F., Basar, E., and Alexandropoulos, G. C. (2022a). A new ris architecture with a single power amplifier: Energy efficiency and error performance analysis. *IEEE Access*, 10:44804–44815.

[Tasci et al., 2022b] Tasci, R. A., Kilinc, F., Basar, E., and Alexandropoulos, G. C. (2022b). A new RIS architecture with a single power amplifier: Energy efficiency and error performance analysis. *IEEE Access*, pages 1–1.

[Tasci et al., 2022c] Tasci, R. A., Kilinc, F., Basar, E., and Alexandropoulos, G. C. (2022c). A new RIS architecture with a single power amplifier: Energy efficiency and error performance analysis. *IEEE Access*, 10:44804–44815.

[Thirumavalavan and Jayaraman, 2020] Thirumavalavan, V. C. and Jayaraman, T. S. (2020). BER analysis of reconfigurable intelligent surface assisted downlink power domain NOMA system. In *2020 Int. Conf. Commun. Syst. Netw. (COMSNETS)*, pages 519–522. IEEE.

[Tugtekin et al., 2023] Tugtekin, O. F., Dogukan, A. T., Arslan, E., and Basar, E. (2023). Coordinate interleaved OFDM with repeated in-phase/quadrature index modulation. *IEEE Trans. Wirel. Commun.*

[Wang et al., 2020] Wang, C.-X., Huang, J., Wang, H., Gao, X., You, X., and Hao, Y. (2020). 6g wireless channel measurements and models: Trends and challenges. *IEEE Vehicular Technology Magazine*, 15(4):22–32.

[Wang et al., 2023a] Wang, C.-X., You, X., Gao, X., Zhu, X., Li, Z., Zhang, C., Wang, H., Huang, Y., Chen, Y., Haas, H., et al. (2023a). On the road to 6g: Visions, requirements, key technologies, and testbeds. *IEEE Communications Surveys & Tutorials*, 25(2):905–974.

[Wang and Swindlehurst, 2023] Wang, F. and Swindlehurst, A. L. (2023). Applications of absorptive reconfigurable intelligent surfaces in interference mitigation and physical layer security. *IEEE Transactions on Wireless Communications*, 23(5):3918–3931.

[Wang et al., 2022] Wang, H., Liu, C., Shi, Z., Fu, Y., and Song, R. (2022). GSIC for RIS-aided uplink multi-antenna NOMA systems. *IEEE Commun. Lett.*, 26(1):187–191.

[Wang et al., 2023b] Wang, J., Gong, S., Wu, Q., and Ma, S. (2023b). Ris-aided mimo systems with hardware impairments: Robust beamforming design and analysis. *IEEE Transactions on Wireless Communications*, 22(10):6914–6929.

[Wen et al., 2015] Wen, M., Cheng, X., Ma, M., Jiao, B., and Poor, H. V. (2015). On the achievable rate of OFDM with index modulation. *IEEE Trans. Signal Process.*, 64(8):1919–1932.

[Wen et al., 2017] Wen, M., Cheng, X., and Yang, L. (2017). *Index modulation for 5G wireless communications*, volume 52. Springer.

[Wu et al., 2021a] Wu, C., Liu, Y., Mu, X., Gu, X., and Dobre, O. A. (2021a). Coverage characterization of STAR-RIS networks: NOMA and OMA. *IEEE Commun. Lett.*, 25(9):3036–3040.

[Wu and Zhang, 2019] Wu, Q. and Zhang, R. (2019). Towards smart and reconfigurable environment: Intelligent reflecting surface aided wireless network. *IEEE Commun. Mag.*, 58(1):106–112.

[Wu and Zhang, 2020] Wu, Q. and Zhang, R. (2020). Towards smart and reconfigurable environment: Intelligent reflecting surface aided wireless network. *IEEE Commun. Mag.*, 58(1):106–112.

[Wu et al., 2021b] Wu, Q., Zhang, S., Zheng, B., You, C., and Zhang, R. (2021b). Intelligent reflecting surface-aided wireless communications: A tutorial. *IEEE Trans. on Commun.*, 69(5):3313–3351.

[Wu et al., 2021c] Wu, Q., Zhang, S., Zheng, B., You, C., and Zhang, R. (2021c). Intelligent reflecting surface-aided wireless communications: A tutorial. *IEEE Trans. Commun.*, 69(5):3313–3351.

[Wymeersch et al., 2020] Wymeersch, H., He, J., Denis, B., Clemente, A., and Juntti, M. (2020). Radio localization and mapping with reconfigurable intelligent surfaces: Challenges, opportunities, and research directions. *IEEE Veh. Technol. Mag.*, 15(4):52–61.

[Yang et al., 2020a] Yang, L., Yang, J., Xie, W., Hasna, M. O., Tsiftsis, T., and Renzo, M. D. (2020a). Secrecy performance analysis of RIS-aided wireless communication systems. *IEEE Trans. Veh. Technol.*, 69(10):12296–12300.

[Yang et al., 2020b] Yang, L., Yang, J., Xie, W., Hasna, M. O., Tsiftsis, T., and Renzo, M. D. (2020b). Secrecy performance analysis of RIS-aided wireless communication systems. *IEEE Trans. Veh. Technol.*, 69(10):12296–12300.

[Yang et al., 2020c] Yang, L., Yang, Y., Hasna, M. O., and Alouini, M.-S. (2020c). Coverage, probability of SNR gain, and DOR analysis of RIS-aided communication systems. *IEEE Wireless Commun. Lett.*, 9(8):1268–1272.

[Yang et al., 2019] Yang, Y., Zhang, S., and Zhang, R. (2019). IRS-enhanced OFDM: Power allocation and passive array optimization. In *Proc. 2019 IEEE Global Commun. Conf. (GLOBECOM)*, pages 1–6. IEEE.

[Yang et al., 2020d] Yang, Y., Zhang, S., and Zhang, R. (2020d). IRS-enhanced OFDMA: Joint resource allocation and passive beamforming optimization. *IEEE Wireless Commun. Lett.*, 9(6):760–764.

[Yang et al., 2020e] Yang, Y., Zheng, B., Zhang, S., and Zhang, R. (2020e). Intelligent reflecting surface meets OFDM: Protocol design and rate maximization. *IEEE Trans. Commun.*, 68(7):4522–4535.

[Ye et al., 2021] Ye, J., Kammoun, A., and Alouini, M. S. (2021). Spatially-distributed RISs vs relay-assisted systems: A fair comparison. *IEEE Open J. Commun. Soc.*, 2:799–817.

[Yigit et al., 2022] Yigit, Z., Basar, E., Wen, M., and Altunbas, I. (2022). Hybrid reflection modulation. *IEEE Trans. Wirel. Commun.*

[Yildirim et al., 2021] Yildirim, I., Kilinc, F., Basar, E., and Alexandropoulos, G. C. (2021). Hybrid RIS-empowered reflection and decode-and-forward relaying for coverage extension. *IEEE Commun. Lett.*, 25(5):1692–1696.

[Yildirim et al., 2020] Yildirim, I., Uyrus, A., and Basar, E. (2020). Modeling and analysis of reconfigurable intelligent surfaces for indoor and outdoor applications in future wireless networks. *IEEE Trans. Commun.*, 69(2):1290–1301.

[Yizhan et al., 2020] Yizhan, C., Zhong, W., Da, H., and Ruosen, L. (2020). 6G is coming: Discussion on key candidate technologies and application scenarios. In *Proc. 2020 Int. Conf. on Comput. Commun. and Netw. Security (CCNS)*, pages 59–62.

[Yu et al., 2024] Yu, Z., Ren, H., Pan, C., Zhou, G., Wang, B., Dong, M., and Wang, J. (2024). Active RIS-aided ISAC systems: Beamforming design and performance analysis. *IEEE Trans. Commun.*, 72(3):1578–1595.

[Yuan et al., 2021] Yuan, J., Wen, M., Li, Q., Basar, E., Alexandropoulos, G. C., and Chen, G. (2021). Receive quadrature reflecting modulation for RIS-empowered wireless communications. *IEEE Trans. Veh. Technol.*, 70(5):5121–5125.

[Zeng et al., 2020] Zeng, S., Zhang, H., Di, B., Han, Z., and Song, L. (2020). Reconfigurable intelligent surface (RIS) assisted wireless coverage extension: RIS orientation and location optimization. *IEEE Commun. Letters*, 25(1):269–273.

[Zeng et al., 2021a] Zeng, S., Zhang, H., Di, B., Han, Z., and Song, L. (2021a). Reconfigurable intelligent surface (ris) assisted wireless coverage extension: Ris orientation and location optimization. *IEEE Commun. Lett.*, 25(1):269–273.

[Zeng et al., 2021b] Zeng, S., Zhang, H., Di, B., Han, Z., and Song, L. (2021b). Reconfigurable intelligent surface (RIS) assisted wireless coverage extension: RIS orientation and location optimization. *IEEE Commun. Lett.*, 25(1):269–273.

[Zhang et al., 2022a] Zhang, C., Peng, Y., Li, J., and Tong, F. (2022a). An IRS-aided GSSK scheme for wireless communication system. *IEEE Commun. Lett.*, 26(6):1398–1402.

[Zhang et al., 2020a] Zhang, H., Di, B., Song, L., and Han, Z. (2020a). Reconfigurable intelligent surfaces assisted communications with limited phase shifts: How many phase shifts are enough? *IEEE Trans. on Veh. Tech.*, 69(4):4498–4502.

[Zhang et al., 2020b] Zhang, H., Di, B., Song, L., and Han, Z. (2020b). Reconfigurable intelligent surfaces assisted communications with limited phase shifts: How many phase shifts are enough? *IEEE Trans. Veh. Technol.*, 69(4):4498–4502.

[Zhang et al., 2021a] Zhang, H., Song, L., Han, Z., and Poor, H. V. (2021a). Spatial equalization before reception: Reconfigurable intelligent surfaces for multi-path mitigation. In *ICASSP 2021-2021 IEEE Int. Conf. Acoust., Speech and Signal Process. (ICASSP)*, pages 8062–8066. IEEE.

[Zhang et al., 2021b] Zhang, Z., Dai, L., Chen, X., Liu, C., Yang, F., Schober, R., and Poor, H. V. (2021b). Active RIS vs. passive RIS: Which will prevail in 6G? *arXiv preprint arXiv:2103.15154*.

[Zhang et al., 2022b] Zhang, Z., Dai, L., Chen, X., Liu, C., Yang, F., Schober, R., and Poor, H. V. (2022b). Active RIS vs. passive RIS: Which will prevail in 6G? *IEEE Trans. Commun.*, 71(3):1707–1725.

[Zhang et al., 2021c] Zhang, Z., Zhang, C., Jiang, C., Jia, F., Ge, J., and Gong, F. (2021c). Improving physical layer security for reconfigurable intelligent surface aided NOMA 6G mmworks. *IEEE Trans. Veh. Technol.*, 70(5):4451–4463.

[Zheng et al., 2020] Zheng, B., You, C., and Zhang, R. (2020). Fast channel estimation for IRS-assisted OFDM. *IEEE Wireless Commun. Lett.*, 10(3):580–584.

[Zheng and Zhang, 2020] Zheng, B. and Zhang, R. (2020). Intelligent reflecting surface-enhanced OFDM: Channel estimation and reflection optimization. *IEEE Wireless Commun. Lett.*, 9(4):518–522.

[Zhi et al., 2022] Zhi, K., Pan, C., Ren, H., Chai, K. K., and Elkashlan, M. (2022). Active RIS versus passive RIS: Which is superior with the same power budget? *IEEE Commun. Lett.*, pages 1–1.

[Zhu et al., 2020] Zhu, J., Zhao, M., Zhang, S., and Zhou, W. (2020). Exploring the road to 6G: ABC — foundation for intelligent mobile networks. *China Commun.*, 17(6):51–67.

Appendix A

A.1 Proof of Lemma 1

Let us define

$$A = \sqrt{\alpha} \sum_{m=1}^{M} |h_1^m||h_{BS}^m|. \tag{A.1.1}$$

The active part of the RIS aligns coherently to cancel out the phases of the complex Gaussian random variables h_1^m and h_{BS}^m hence, resulting in only the magnitude of the channels $|h_1^m|$ and $|h_{BS}^m|$ which are i.i.d. Rayleigh distributed. Since they are i.i.d. random variables, the mean can be expressed as the product of their individual means as

$$\mathrm{E}[|h_1^m||h_{BS}^m|] = \mathrm{E}[|h_1^m|]\mathrm{E}[|h_{BS}^m|]. \tag{A.1.2}$$

Thus (A.2) equates to

$$\left(\sigma_{h_1}\sqrt{\frac{\pi}{4}}\right)\left(\sigma_{h_{BS}}\sqrt{\frac{\pi}{4}}\right) = \frac{\sigma_{h_1}\sigma_{h_{BS}}\pi}{4}. \tag{A.1.3}$$

On the other hand, the variance is calculated using

$$\mathrm{VAR}[|h_1^m||h_{BS}^m|] = \mathrm{E}[(|h_1^m||h_{BS}^m|)^2] - \mathrm{E}[|h_1^m||h_{BS}^m|]^2. \tag{A.1.4}$$

The calculation of $\mathrm{E}[|h_1^m||h_{BS}^m|]^2$ is simple as we just square (A.3) resulting in

$$\mathrm{E}[|h_1^m||h_{BS}^m|]^2 = \frac{\sigma_{h_1}^2\sigma_{h_{BS}}^2\pi^2}{16}. \tag{A.1.5}$$

To obtain $\mathrm{E}[(|h_1^m||h_{BS}^m|)^2]$, which can be re expressed as $\mathrm{E}[|h_1^m|^2]\mathrm{E}[|h_{BS}^m|^2]$, we need to find the individual second moments.

We will find the second moment for $|h_1^m|$ as $\mathrm{E}[|h_1^m|^2]$ since the same can be applied for the latter. The variance will help us to do so:

$$\text{VAR}[|h_1^m|] = \text{E}[|h_1^m|^2] - \text{E}[|h_1^m|]^2. \tag{A.1.6}$$

Reordering allows us to solve for the desired $\text{E}[|h_1^m|^2]$ as

$$\begin{aligned}
\text{E}[|h_1^m|^2] &= VAR[|h_1^m|] + \text{E}[|h_1^m|^2] && \text{(A.1.7)}\\
&= \frac{4\sigma_{h_1}^2}{4} - \frac{\pi}{2} \cdot \frac{\sigma_{h_1}^2}{2} + \frac{\sigma_{h_1}^2 \pi}{4} && \text{(A.1.8)}\\
&= \sigma_{h_1}^2 && \text{(A.1.9)}
\end{aligned}$$

The same is applied to $\text{E}[|h_{BS}^m|^2]$ resulting in $\sigma_{h_{BS}}^2$. Thus, $\text{E}[(|h_1^m||h_{BS}^m|)^2]$ is expressed as

$$\text{E}[(|h_1^m||h_{BS}^m|)^2] = \sigma_{h_1}^2 \sigma_{h_{BS}}^2. \tag{A.1.10}$$

Finally, to obtain the variance of $|h_1^m||h_{BS}^m|$ we substitute (A.5) and (A.10) into (A.4) to obtain

$$\text{VAR}[|h_1^m||h_{BS}^m|] = \sigma_{h_1}^2 \sigma_{h_{BS}}^2 (1 - \frac{\pi^2}{16}). \tag{A.1.11}$$

When the number of RIS elements M is significantly large, from the CLT, the random variable A from (A.1) converges to a real Gaussian distributed random variable with $A \sim \mathcal{N}(\frac{\sqrt{\alpha} M \pi \sigma_{h_1} \sigma_{BS}}{4}, \, \alpha M \sigma_{h_1}^2 \sigma_{BS}^2 (1 - \frac{\pi^2}{16}))$.

Appendix B

B.1 Proof of Lemma 2

For B, we have the complex Gaussian random variable as

$$B = \sum_{n=1}^{N} g_1^n \beta^n g_{BS}^n. \tag{B.1.1}$$

The passive part of the RIS (β^n) does not align coherently for the channels, hence, the phases do not cancel out and remains a complex Gaussian distributed random variable. Thus the mean remains zero and the variance is the multiplication of the variances of the two i.i.d random variables g_1^n and g_{BS}^n as

$$\mathrm{VAR}[g_1^n g_{BS}^n] = \mathrm{VAR}[g_1^n]\mathrm{VAR}[g_{BS}^n] = (\sigma_{g_1}^2)(\sigma_{g_{BS}}^2). \tag{B.1.2}$$

Due to sufficiently large N elements from the RIS, and the CLT, the variance can be finalized as

$$\mathrm{VAR}[B] = N\sigma_{g_1}^2\sigma_{g_{BS}}^2. \tag{B.1.3}$$

Appendix C

C.1 Proof of Lemma 3

Furthermore, the means and variances or the random variables C and D are found similarly as in A and B. C is not coherently aligned with the active part of the RIS, therefore the approach in B is exploited. D is coherently aligned with the passive part of the RIS, hence, the identical approach of A is considered.

E is simply the multiplication of the phase shift of the RIS element $e^{j\phi_m}$ and h_{BS}^m. Since the mean and variance do not change when multiplied with an exponential term, E follows the same distribution as h_{BS}^m which is $\mathcal{CN}(0, \sigma_{BS}^2)$. F is simply the noise term and its distribution has been provided.

Appendix D

D.1 Proof of Lemma 4

As it can be seen from (3), A and the C have h_{BS}^m as a common term; however, they are independent since they are uncorrelated and Gaussian distributed. To find their correlation coefficient, the covariance of A and C is required and since C has zero mean, it may be expressed as

$$\mathrm{E}[AC] = \mathrm{E}\left[\left(\sum_{m=1}^{M} h_1^m e^{j\theta_m} h_{BS}^m\right)\left(\sum_{m=1}^{M} h_2^m e^{j\theta_m} h_{BS}^m\right)\right]. \tag{D.1.1}$$

After adjusting the RIS phases according to the first path, (D.1) may be re-expressed as

$$\mathrm{E}[AC] = \mathrm{E}\left[\left(\sum_{m=1}^{M} |h_1^m||h_{BS}^m|\right)\left(\sum_{m=1}^{M} h_2^m e^{-j\angle h_2^m} |h_{BS}^m|\right)\right]. \tag{D.1.2}$$

Here, h_1 is a complex Gaussian term with zero mean hence, $\mathrm{E}[AC] = 0$. Therefore, the correlation coefficient of A and C is also zero resulting in A and C being uncorrelated. Furthermore, they are Gaussian distributed and independent. On the other hand, the same procedure applies for B and D where they share the g_{BS}^n term.